KU Leuven
Group Biomedical Sciences
Faculty of Medicine
Department of Imaging & Pathology

IN VIVO IMAGING OF IMMUNE CELLS USING ^{19}F MRI IN DIFFERENT DISEASE MODELS

Shweta Saini

Jury:

Promoter:	Prof. Uwe Himmelreich
Co-promoter:	Dr. Hannelie Korf
Chair:	Prof. Ghislain Opdenakker
Secretary:	Prof. Olivier Gheysens
Jury members:	Prof. Pieter Gillard
	Prof. Olivier Gheysens
	Dr. Philipp Boehm-Sturm
	Prof. Ivo Lambrichts

Dissertation presented in partial fulfilment of the requirements for the degree of Doctor in Biomedical Sciences.

June 2019

Table of Contents

Acknowledgements

My very interesting PhD journey finally brought me here, to thank all the people who taught me so much, both personally and professionally during these amazing 5 years. Indeed, I must take a stop here, go back down the memory lane and thank them before, I move forward.

My promoter Prof. Uwe Himmelreich deserves a big thank for granting me this challenging opportunity and supporting me through out. Thank you for showing faith in my abilities. Every time I was frustrated, I knocked on your door and you always motivated me to protect my PhD boat from shattering in the ordeal of ocean and believed that I will one day reach the shore. Off course, I got scared from the sound of waves and dark clouds on my way but you always showed me light at the end of the tunnel. I really appreciate your generosity and a lot of patience (I am still trying to learn it ☺). I would also like to thank my co-promoter Dr. Hannelie Korf for her tremendous help throughout my PhD and showing me different aspects of life and research.

My sincere thanks to all my jury members Prof. Pieter Gillard, Prof. Olivier Gheysens Dr. Philipp Boehm-Sturm and Prof. Ivo Lambrichts for your highly valuable suggestions and critical feedbacks, which for sure helped in the betterment of this thesis. Dr. Philipp, I owe you special thanks for encouraging me to submit my paper in the special issue of fluorine MRI, despite of my enormous confusions regarding it.

'Thank you' may be a small word for many people I came across in Mosaic. Tom Dresselaers, thank you so much for being my first teacher in Mosaic and giving me introduction of two big MR scanners with patience. Bella and Stefaan, thank you very much for your help in my experiments and a lot of chit chats about various off topic things. Willy, thank you for helping me grow both personally and professionally. Peter, a big thank to you for resolving all the money matters ;), I am so happy you visited India. I enjoyed the cultural discussion with you and your wife a lot. Ann, thank you for keeping an eye on our stock availability and keeping everything organized. Jens, thank you for helping me with liquid nitrogen dewar and all the cool 'tattoo talks' (btw congratulations for being a daddy now ☺). Tinne, thanks a lot for your help in my experiments.

I highly appreciate my scientific collaborators from KU Leuven, Prof. Chantal Mathieu, for giving me the opportunity to work in her lab. I would like to thank Dr. Conny Gysemans for her valuable support, critical feedback on data analysis and experimental planning. An-Sofie, thank you for all the help you provided for my last experiments specially, coming to the lab during the weekends and helping me with the collection of 'DCs in deep slumber' from crazy 50+ well plates!! I found you as a very hard working and dedicated person. Congratulations on your job Dr. ☺. Jos Loreys and Dries Swinnen, thank you very much for all the technical help in my last experiments. My collaborators from Ghent University, Prof. Stefaan De Smedt, thank you for a very nice and fruitful collaboration. A special thanks to Rein Verbeke for taking care of the nanoparticle synthesis and always being kind to my last minute requests (which I had a lot!!). I wish you all the luck with your upcoming defense and future. Thank you Dr. James Dooley and Prof. Adrian Liston with the immunohistochemistry. I learnt a lot from you both.

My fellow sailors!! aka s#ame colleagues ☺, many thanks to all of you for being there always and helping me in various phases of my PhD life. Bryan, thank you for 'kindly giving me' dry ice at various time points. Kristof, thanks for testing my patience not one time but 'several' times. Thank you for helping me with image processing, you are brilliant and next in the row for defense so good luck ☺. Bart, when you will get The Nobel Prize please don't forget to invite me in the ceremony!! Bram, you can do it !!, the ^{19}F MRI legacy is now on your name so please take good care of that tiny piece of…..coil ☺. Liesbeth, my office neighbor, thank you for all the 'ideas' you gave me and my 'desktop' is working fine now ☺. I wish you all the best for the final phase of your PhD. Sarah, you are now carrying the remaining load of particles on your shoulders and I am sure you will do justice to it. You know what, we sing better karaoke!! Thank you so much for your helping hand in my PhD thesis 'transportations'☺ and good luck for your PhD. Rita, thanks for being my Marie Curie partner. Sayuan, you were my fluorine mentor and I learnt so much from you. I know, I annoyed you many times with my 'special questions' but because of those questions, you know finally, I made it. Kaat and Sergi, thank you for all the interesting discussions during lunchtime, I wish you good luck with your careers. Noelia, your kind help during my final doctoral plan is highly appreciated, congratulations for being a mother now. Akila, yes, I believe that coconut oil, cucumber and soda can help overcome ALS and tanning, how exciting!! ☺.

Jennifer, thank you so much for your help in saving the sinking ship. I think I can never thank you enough. I took fungi a bit too seriously, but I am happy that after a long struggle now life is fungus-

free ☺. Always be the kind of person you are, pure and honest (not too honest ☺). Melissa, my partner in crime, thank you for sprinkling all the support and craziness around. I could not have managed it without being insane ☺. I guess, we were destined to meet and look we are also defending together ☺. Always remember 'Nalu' is strictly prohibited by the sugar police ☺. All the best for your future.

My Indian friends, Eshwar-Priya, Saurabh-Kanchan, Abhishek-Suravi, Vikas-Kajal, Rudra, Parveen and Ritesh, thank you for all amazing indian festivals and times we celebrated together. I never felt that I am alone here because of you all. Thank you Bala, for helping with your 'magical chemistry'. You know the screws of that tube holder actually screwed things up ☺. Jennifer and I really enjoyed laughed so hard during that experiment ☺ ☺.

Now it is the time to thank family. My parents and parents-in-law, you were my strength when I was weak. Thank you for cherishing every big/small success I achieved and thanks a lot for always motivating me with your love and care. Mom and Dad, you are my two strong pillars and it is because of you both, I am here finishing a big chapter of my life. I was so happy to have you both in Belgium last year. I hope you enjoyed the other side of the world. With you, I created most amazing and precious memories of my life. I wish you all good health and a lot of happiness. In this birth, I can never repay what you gave to me. Richa, Ritu and Shekher, DD loves you a lot and wish a lot of success and good health to all of you. You all actually did PhD with me as you were always there in my mind and in my heart.

Sumit, you are a lot more than my husband, a friend, a guide and an 'absorber'. You absorbed all my frustrations and helped me reaching to this point in my life. It was you, who persuaded me to do a PhD. I know we live far from each other during my PhD and I know it was very difficult for us to manage, but you supported me with all that mental peace, I needed at times. I learnt a lot from you. You are a very kind person and a fresh breeze of solace. You are the only one of you, may be that's the fun of you. I am fortunate to have you as my soulmate and happy that now we are together forever ♥ ♥….

Summary

Cell tracking, in particular immune cell tracking strategies are gaining momentum in order to better understand the pathology and treatment strategies in different diseases. Inflammation is a hallmark in many diseases like autoimmune disorders, infectious diseases, cancer, neurodegeneration, cardiovascular diseases and others. In this context, immune cells are of high interest for studying the mechanism of diseases. Specific populations of immune cells are commonly identified by measuring the expressions of their cellular surface molecules by flow cytometry or immunohistochemistry. These invasive techniques provide *in vitro* quantitative and qualitative data about the number and type of immune cells present an organ/tissue region. However, with these techniques it is difficult to noninvasively follow and measure the location and migration of immune cells longitudinally in the same individual.

Molecular imaging modalities like conventional magnetic resonance imaging (MRI) are emerging as powerful cell tracking techniques, which can be exploited for the longitudinal follow-up of immune cell migration, cell physiology and thus inflammation. MRI-based cell tracking facilitates the evaluation of novel therapeutics in particular for approaches that stimulate endogenous and exogenous immune cell recruitment like in immunotherapies. In this regard, flourine-19 magnetic resonance imaging (^{19}F MRI) is becoming popular for cellular imaging applications, thanks to the possibility of direct quantification of labeled cells in a region of interest and due to the lack of endogenous background signal. For the *in vivo* visualization of immune cells, it is important to first label them with a suitably and biologically safe contrast agent by *in vitro* or *in vivo* cell labeling methods. For the same, PFC-based contrast agents are already used for both preclinical and clinical applications. However, a tailored labeling approach is required for different immune cells in order to achieve sufficient labeling for their *in vivo* detection using ^{19}F MRI, hereby overcoming the intrinsically low sensitivity of ^{19}F MRI.

In this thesis, we have optimized the labeling approaches of different immune cells. Firstly, macrophages were labeled *in vivo* by exploiting their phagocytic property. We showed high uptake of newly synthesized and biocompatible zonyl PFCE nanoparticles (ZPFCE-NPs) by macrophages.

We investigated the intricate immune cell infiltration in the pulmonary region of *A. fumigatus* infected mice in three different models using either no or two different clinically applied immunosuppressive drugs by using ^{19}F MRI. We detected variations in the immune responses and immune cell migration of the labeled macrophages *in vivo* in infected and healthy animals at different time-points. We combined ^{19}F MRI with bioluminescence imaging (BLI) and fluorescence imaging (FLI) to better understand the progression of infection and inflammation in immunocompetent and immunocompromised mice upon *A. fumigatus* challenge. With this imaging platform, we showed the potential of ^{19}F MRI for specific quantification and tracking of macrophages in different aspergillosis models.

Cell labeling strategies for non-phagocytic cells are more challenging and mostly difficult to achieve without using transfection agents. We explored the labeling of T cells with the help of lipid modified PFCE-based nanoparticles for their *in vivo* homing in the pancreatic region of a type 1 diabetes (T1D) mouse model. We proved that *in vitro* labeling of T cells can be achieved and that cells can be visualized in *in vivo* phantoms using ^{19}F MRI. However, for the *in vivo* detection of labeled T cells after their transplantation in the T1D model, we failed to reach local cell concentrations that would overcome the detectability limit of ^{19}F MRI (~10^{16} fluorine atoms/voxel). Based on our observations, the proliferation of these cells diluted the label rapidly so that nanoparticle concentrations per cell were too low for the generation of detectable MR signal in the pancreatic region of the T1D mouse model using ^{19}F MRI.

Dendritic cells (DCs) are another type of immune cells widely studied for their role in triggering autoimmunity in T1D and other diseases. Recently, these cells gained popularity for their use as DC vaccines in cancer therapy. We employed a ^{19}F MR imaging approach by *in vitro* labeling DCs with ZPFCE-NPs and following them longitudinally after engraftment in the pancreatic region of T1D mice, with or without mild pancreatitis. We showed the feasibility of our imaging platform for the evaluation of modulated DCs for facilitating treatment not limited to autoimmune diseases but possibly also suitable for DC-based cancer therapies.

Together, this research has explored not only the potential but also, the limitations of preclinical ^{19}F MRI. We showed the cell labeling and *in vivo* tracking applications by investigating purpose

developed fluorinated contrast agents. With clinically safe and already in-use contrast agents, ^{19}F MRI has moved closer to translation towards the clinic but also for a better understanding of various complex diseases using preclinical models. This potent imaging technique allows the quantitative assessment of engrafted cells *in vivo* for the diagnosis and testing of novel cellular therapeutics. We believe that this research will lay a firm foundation for the improvement of cell-based therapies by providing a validation tool based on ^{19}F MRI, with a scope of future translation to humans.

Samenvatting

Het traceren van cellulaire entiteiten, en in het bijzonder immuuncellen, wordt steeds belangrijker om de pathologie en behandelingsstrategieën van verschillende ziektes beter te begrijpen. Inflammatie is een typisch kenmerk van diverse stoornissen zoals onder andere autoimmuunziektes, infectieziektes, kanker, neurodegeneratie en cardiovasculaire aandoeningen. In deze context is de studie van immuuncellen essentieel om deze ziektemechanismen te ontrafelen. Flowcytometrie en immunohistochemie zijn technieken waarmee diverse celpopulaties geïdentificeerd kunnen worden op basis van de expressie van specifieke molecules op het cel oppervlak. Deze *in vitro* technieken verschaffen zowel quantitatieve als qualitatieve data over het aantal en type van immuuncellen aanwezig in een bepaald orgaan of weefsel. Deze invasieve technieken laten echter niet toe om de locatie/migratie van immuuncellen longitudinaal op te volgen binnen hetzelfde individu.

Moleculaire beeldvormingstechnieken, zoals conventionele magnetische resonantie beeldvorming (MRI), zijn beloftevolle technieken die aangewend kunnen worden voor de longitudinale follow-up van immuuncel migratie, fysiologie, en dus ook inflammatie. Deze MRI-gebaseerde technieken verbeteren de evaluatie van nieuwe therapieën zoals immunotherapie, waarbij de rekrutering van zowel de endogene als exogene immuuncellen gestimuleerd wordt. Om deze reden wint fluor-19 (^{19}F) beeldvorming (^{19}F MRI) aan populariteit. Deze techniek biedt de mogelijkheid om gemerkte cellen te quantificeren in een afgelijnde regio, met als voordeel de afwezigheid van een endogeen achtergrondsignaal. Om immuun cellen *in vivo* te kunnen visualiseren, is het belangrijk om ze eerst primair te labelen met geschikte contraststoffen door middel van *in vitro* en *in vivo* labeling technieken. PFC-gebaseerde contraststoffen werden reeds succesvol gebruikt voor dit doel in zowel preklinische als klinische applicaties. Vanwege de intrinsieke lage sensitiviteit van ^{19}F MRI, zijn aangepaste en specifieke procedures vereist om de immuun cellen voldoende te labelen voor *in vivo* detectie door middel van ^{19}F MRI.

In deze thesis werden vooreerst de labeling procedures geoptimaliseerd voor verschillende types van immuuncellen. Macrofagen werden *in vivo* gelabeled door gebruik te maken van de

fagocytische eigenschappen. Deze cellen toonden een hoge opname van nieuwe, biocompatibele zonyl PFCE nanopartikels (ZPFCE-NPs). Vervolgens werd ^{19}F MRI gebruikt om de infiltratie van deze immuuncellen te onderzoeken in de longen van *A. fumigatus* geïnfecteerde muizen. Hiervoor werden drie verschillende muismodellen gebruikt, waarbij ofwel geen ofwel twee verschillende klinisch-gebruikte immunosuppressiva toegediend werden. In deze in vivo studie werden variaties gevonden in de immuunrespons en immuuncel migratie van de gelabelde macrofagen tussen gezonde en geïnfecteerde dieren op specifieke tijdspunten. ^{19}F MRI werd gecombineerd met bioluminescentie (BLI) en fluorescentie beeldvorming (FLI) om de progressie van de infectie en inflammatie in deze immunocompetente en immunodeficiënte muizenbeter te begrijpen. Met dit beeldvormingsplatform toonden werd het potentieel van ^{19}F MRI aangetoond voor de kwantificatie en opvolging van macrofagen in verschillende modellen van invasive pulmonaire aspergillosis.

In tegenstelling tot fagocyterende immuuncellen, is het labelen van immuuncellen zonder fagocyterende eigenschappen veel moeilijker te realiseren zonder gebruik te maken van transfectie agentia. In deze studie werden T cellen gelabeled met behulp van lipide-gemodificeerde PFCE-gebaseerde nanopartikels. Daarna werd het spreidingspatroon van deze cellen in de regio van de pancreas onderzocht in een diabetes type 1 (DT1) muis model. We toonden aan dat het *in vitro* labelen van T cellen mogelijk is en dat de cellen kunnen worden gevisualiseerd met ^{19}F MRI in *in vivo* fantomen. Het bleek echter niet mogelijk te zijn in om de T cellen *in vivo* te detecteren na transplantatie in het DT1 muismodel, mede omdat de cellulaire concentraties onder de detectielimiet bleven (~10^6 fluor atomen/voxel). Deze observaties toonden aan dat het label zeer snel verdunt onder invloed van de proliferatie van deze cellen, waardoor de nanopartikel concentraties per cel te laag zijn om een detecteerbaar ^{19}F MR signaal te genereren in de pancreas van het DT1 muis model.

Dendritische cellen (DCs) zijn een andere klasse van immuuncellen die extensief bestudeerd worden vanwege hun rol in het initiëren van autoimmuniteit in TD1 en andere aandoeningen. In recente studies werden deze immuuncellen vooral aangewend als DC vaccins voor de mogelijke behandeling van kanker. In deze studie werden DCs *in vitro* gelabeled met ZPFCE-NPs en vervolgens longitudinaal opgevolgd na implantatie in de regio van de pancreas in TD1 muizen met

of zonder milde pancreatitis. Met deze studie toonden we aan dat ons beeldvormingplatform gebruikt kan worden voor de evaluatie van gemoduleerde DCs, met potentieel voor de behandeling van autoimmuunziektes en kanker.

In conclusie, ons onderzoek heeft zowel het potentieel als de limitaties van preklinische ^{19}F MRI geëxploreerd, door gebruik te maken van specifieke ^{19}F-gelabelde contraststoffen voor het labelen en opvolgen van cellen *in vivo*. Aangezien deze agentia als klinisch veilig worden beschouwd en dus klaar zijn voor gebruik in patiënten, kan ^{19}F MRI niet enkel gebruikt worden om complexe pathologieën beter te begrijpen via preklinische modellen, maar heeft deze techniek ook een groot potentieel voor translatie naar een klinische omgeving. Deze veelbelovende beeldvormingsmodaliteit laat ons toe om geïmplanteerde cellen kwantitatief op te volgen, om zowel de diagnose als ook het testen van nieuwe cel-gebaseerde therapieën te faciliteren. We geloven dat ons onderzoek een robuuste basis biedt voor de verbetering van cel-gebaseerde therapeutische strategieën met ^{19}F MRI als validatie instrument voor toekomstige toepassingen in mensen.

List of abbreviations

^{1}H MRI	Proton Magnetic Resonance Imaging
2D	Two dimensions
5-FU	5-fluorouracil
^{19}F MRI	Fluorine Magnetic Resonance Imaging
^{19}F MRS	Fluorine Magnetic Resonance Spectroscopy
FDG	^{18}F- fluorodeoxyglucose
APC	Antigen presenting cell
ATP	Adenosine triphosphate
BAL	Broncho-alveolar lavage
BLI	Bioluminescence Imaging
CCD	Charge-coupled device
CFU	Colony-forming unit
CT	Computed tomography
CY	Cyclophosphamide
DC	Dendritic Cell
FLI	Fluorescence imaging
FOV	Field of view
Gd	Gadolinium
HCA	Hydrocortisone acetate
IPA	Invasive pulmonary aspergillosis
LPS	Lipopolysaccharide

NMR	Nuclear magnetic resonance
NP	Nanoparticle
PAS	Periodic acid-Schiff
PBS	Phosphate-buffered saline
PET	Positron emission tomography
PFC	Perfluorocarbons
PFCE	Perfluoro-15-crown-5-ether
PFOB	Perfluorooctylbromide
PFPE	Perfluoropolyethers
RF	Radiofrequency
ROI	Region of Interests
SNR	Signal-to-Noise Ratio
SPIO	Super-paramagnetic iron oxide
STZ	Streptozotocin
T1	Spin-Lattice Relaxation
T2	Spin- Spin Relaxation
TE	Echo Time
T1D	Type 1 Diabetes
TCR	T cell receptor
US	Ultrasound

CHAPTER 1

Introduction

1.1 General introduction

Our knowledge of molecular and cellular processes was traditionally based on detailed studies of excised tissue using histological methods. However, this approach does not provide information on dynamic processes in an intact organism. With improved *in vivo* imaging methods and sensitive contrast agents, cell imaging under *in vivo* conditions is now possible. Hereby, immune cell imaging is a very important tool for the in depth understanding of disease mechanisms and cell therapy. Immune cells are successfully used in the treatment of autoimmune disease and cancer (1, 2). It is crucial to study the dynamics of the inherent behavior of immune cells and their safe application as therapeutic vehicle.

Development of advanced imaging techniques is also essential to broaden our knowledge of interactions of immune cells diseased tissue and disease-causing agents under physiological and pathophysiological conditions. Dynamic *in vivo* molecular imaging is a rapidly growing field also applied for the visualization of immune cells (3, 4). Combining different imaging techniques in preclinical and clinical studies can enhance the development of effective and safe treatments (5, 6). One of the most important advantages of using imaging techniques is the reduction of the number of experimental animals in preclinical studies due to the acquisition of data from the same animal at repeated time points. This not only reduces the costs of the experiments but also enhances statistical power as each animal can act as it's own control.

For successful imaging of immune cells, several factors need to be addressed for planning experimental studies. For example, selection of the most suitable method(s) will depend on the biological question that needs to be answered. Every imaging method has its own advantages and disadvantages. In addition to the imaging methods, contrast agents or tracers are required in particular for immune cell tracking, where different cell labeling methods can be optimized for the desired immune cell type and time- frame over which cells have to be monitored.

1.2 Molecular Imaging

The precept of molecular imaging started with 'seeing is believing' and since then, it has evolved into a quantitative approach with dramatic impact on many preclinical and clinical studies (7). Imaging techniques like magnetic resonance imaging (MRI), positron emission tomography (PET), ultrasound and optical imaging are widely used to study miniscule biological processes at

molecular level. The major contribution of molecular imaging especially for disease diagnosis is the ability to visualize specific target(s) known as biomarkers to gather in-depth details on the pathology for diseases monitoring (5). Both researchers and clinicians incline towards visualization of the disease onset and progression non-invasively over blood tests/biopsies to aid in disease assessment. For multimodal imaging, two or more molecular imaging techniques are combined for a single investigation in order to cross-validate data. Multimodal imaging platforms like PET/MR, PET/CT etc. aid in elucidating sensitive and specific detection of diseases for tailored and refine treatments of individual patients by combining molecular information (for example PET but also MRI) with anatomical information (for example, CT and MRI). Innovations in the imaging technology also increased the demand of contrast agents to study the *in vivo* biological interactions (Fig. 1).

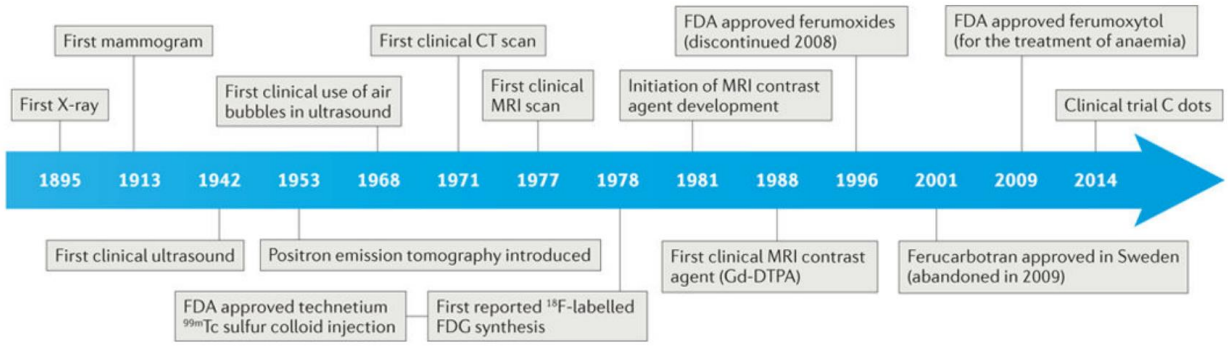

Fig. 1. Timeline of the development of imaging techniques and contrast agents/ tracers for the in-depth understanding of the disease mechanisms (8).

Modern cutting-edge research in oncology, endocrinology, neurology or infectious diseases requires imaging platform that combine advanced imaging technology with sensitive and specific contrast agents and tracers for *in vivo* monitoring of anatomical, functional and molecular processes. In most diseases, inflammation is involved in the onset of underlying chronic or acute pathological state where noninvasive imaging of inflammatory immune components could potentially improve disease diagnosis and allow early therapeutic intervention (9–12). Noninvasive molecular imaging techniques together with specific potential contrast agent can longitudinally track the structural and molecular changes occurring in the biological environment.

One efficient way of imaging inflammation is targeting the trafficking of immune cells and changes in their migratory patterns in degenerative, infectious or autoimmune diseases. Major

breakthroughs in recent years on labeling of macrophages, monocytes and lymphocytes with contrast agents and tracers allow sensitive follow-up of disease onset and progression using modalities like MRI, PET, CT, optical imaging etc. (13–19).

1.3 Imaging of Immune cells: brief overview

Imagine living a life where even the smallest organism living on earth is strong enough to give you a lethal attack. The reason we have lived our life thus far, relies in the workflow of our defense mechanism together with it's defenders, which protected us from all of these harmful organisms like parasites, viruses, bacteria etc. This defense mechanism is known as immune system and here immune cells are our defenders. Immune cells are born from immortal hematopoietic stem cells present in the bone marrow. These stem cells generate daughter cells known as progenitor cells, which further differentiate into various types of immune cells (Fig. 2).

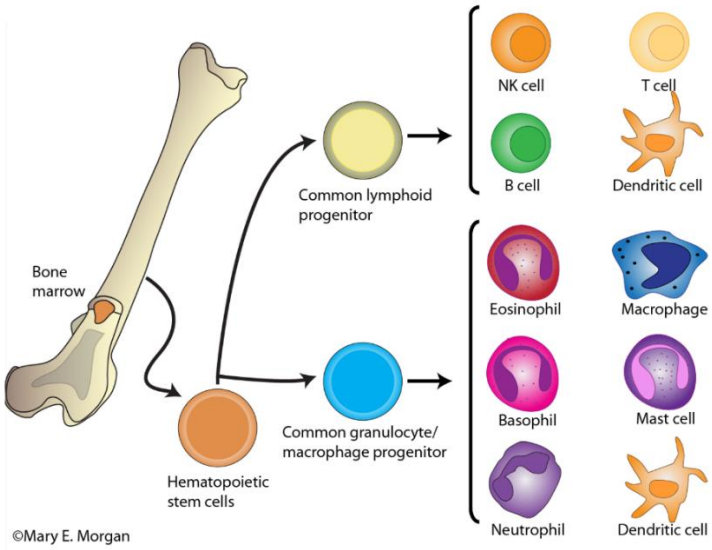

Fig. 2 Generation of different immune cells from the hematopoietic stem cells located in the bone marrow. (Source: http://theibdimmunologist.com).

Broadly, these defenders based on their roles belongs to either innate immune system or adaptive immune system (20). Innate immune system gives innate immunity encoded in our germline and passed on through different generations with small genetic fine-tuning (21). The innate immune cells are monocytes, dendritic cells (DCs), macrophages, granulocytes, natural killer cells, and other cells. Innate immunity thus provides immediate protection against intruders however; this protection is incomplete and possess short-term memory. Therefore, as an extra defensive plan,

our body contacts more specialized soldiers from adaptive immune system providing adaptive (acquired) immunity. These soldiers are known as T cells and B cells. Be it innate immune cells or adaptive immune cells, each cell-type has a distinct role in the cascade of events happening after the encounter of an intruder. Realizing the strength and type of danger both these innate and adaptive immune systems either work together by joining hands or defend alone against the intruder. Here, we introduce the different types of immune cells studied in this thesis.

- Macrophages

  Macrophages are known for their antigen-presenting capacity and as innate immune cells, play distinctive role in the host defense mechanisms. Macrophages are distributed in different body tissues. The modus operandi of macrophages is ingesting, processing and clearing foreign materials. For the recruitment of additional macrophages, they present these foreign materials on their cell surface as an inflammatory response (22–24). This behavior not only triggers phagocytes but also initiate adaptive immune response. Macrophages are broadly divided in two categories classically activated macrophages (M1) and alternatively activated (M2) or tumor-associated macrophages (25). The M1 subtype is responsible for the secretion of proinflammatory cytokines like IL-1β, TNF-α, IL-6 etc. These macrophages not only perform eradication of dead cells and debris but also elevate inflammation against foreign materials. The M2 subtype is further divided in M2a, M2b, M2c and M2d macrophages playing crucial role in wound healing and immune regulatory functions like immunosuppression and immune regulation (26, 27). The investigation of macrophages using molecular imaging techniques like PET, MRI, optical imaging etc. enables us to better understand inflammatory diseases and interaction of tumor with surrounding tissue (18, 28). In particular, the migratory pattern upon inflammatory signals in various diseases will help in tailoring and testing anti-inflammatory medications.

- T cells

  T cells are part of adaptive immune system. Thanks to their distinctive surface proteins/receptors called T cell receptors (TCRs) they are highly specialized in recognizing

antigens upon their presentation on APCs like macrophages, dendritic cells etc. For the activation of T cells, it is important to have binding between TCR and the antigen. These cells are divided in two categories: helper (CD4+) T cells and cytotoxic (CD8+) T cells (29). After the formation of the TCR-MHC II complex, a cascade of immune reactions takes place in the body. As a result, the CD4+ T cells triggers the activation of B cells for antibodies release and macrophages for clearance of dead cell debris. The CD4+ T cells also activates CD8+ T cells for apoptosis of the damaged cells (30, 31). In contrast to CD4+ T cells, CD8+ T cells only recognize the antigen peptide presented by the MCH I molecule. CD8+ T cells secrete chemicals like perforin and granzymes to stimulate death of the infected and tumor cells (32, 33). T cell were studied using different molecular imaging techniques like PET for their tracking in melanomas (34). For graft rejection studies, MRI was used to investigate graft rejection by tracking T cells (35).

- Dendritic cells

DCs are professional APCs and help in the regulation of the adaptive immune response (36). Originated from bone marrow precursor cells, DCs are located in the peripheral tissues in immature form. These immune cells are responsible for the capturing, processing and presentation of antigens to both types of T cells (37). These processes change the status of immature DCs to matured DCs. Upon maturation, DCs show high expression of co-stimulatory molecules together with MHC class I and II molecules (38, 39). DCs were studied as potential antitumor therapy in cancer patients (40). The potential of DC vaccines against cancer made these immune cells a very promising tool in tumor therapy. Hereby, determination of the location and migration by *in vivo* imaging techniques would help in guiding and managing therapy (41, 42).

- Natural killer cells

These lymphocytes of innate immune system are responsible for controlling different types of tumors and microbial infections (43, 44). The natural killer cells (NK) cells are activated by alpha, beta and gamma interferons or cytokines secreted by macrophages. NK cells

induce cytotoxicity without MHC coupling, unlike T cells. These cells are can be used for immunotherapy by targeting malignant cells and their tracking can provide valuable information about the success of therapy against cancer. *In vivo* PET imaging of NK cells was reported after labeling them with ^{18}F or ^{11}C radiotracer (45, 46). Optical imaging techniques are also used for tracking NK cells by labeling them with green fluorescent protein or luciferase reporter genes (47, 48). MRI-based NK cell tracking was performed using genetically engineered cells and injecting them into a NIH 3T3 HER2/neu receptor positive tumor bearing mice. The study reported increased targeting of tumor observed by the injected genetically engineered NK cells. Based on these studies, it might be useful to investigate NK cell-based immunotherapies by tailoring protocols for clinical applications against human malignancy.

- B cells

These cells play pivotal role in the generation of adaptive immune response against infectious diseases by producing antibodies specific to the antigen presented by the pathogen (49, 50). The imaging and tracking of B cells is in it's infancy compared to other immune cell types. Imaging of B cells was performed using PET/CT after injecting ^{89}Zr-labeled anti-B-cell antibody for their tracking in organs like spleen, lymph nodes and joints (51). MRI and FLI imaging modalities were also used for tracking the migration of fluorescent and magnetic nanoparticle-labeled B cells into spleen (52). Further, imaging studies are required in order to fully understand and explore B cell-related disorders and respective therapies.

Immune cells like macrophages, T cells, natural killer cells and dendritic cells are currently also used for the immune cell-based therapies in order to target diseases like cancer, HIV etc. (40, 53–60). Immune cell labeling is often required for applications like flow cytometry and confocal microscopy (61). These techniques applied in research, provide end-point quantification of different cells after cell-specific immunostainings. However, these methods are not suitable for noninvasive *in vivo* follow up of immune cells in deep tissues or organs in live animals.

1.4 Noninvasive imaging modalities: with a focus on cell imaging

Different preclinical and clinical molecular imaging techniques have proven to be an asset in providing longitudinal *in vivo* information to follow-up biological processes under healthy and diseased condition. Every modality has it's own advantages and disadvantages posing limitations for their use (Table. 1). Therefore, multimodal imaging platform helps in overcoming these shortcomings in order to improve diagnosis and therapy follow-up.

Modality	Advantages	Disadvantages	Contrast agents	Radiation
CT	Unlimited tissue depth penetration High spatial resolution Can be used for whole body imaging Low acquisition time Anatomical imaging	Radiation exposure Poor soft tissue contrast	Krypton Xenon Iodine Barium	X-rays
Positron emission tomography (PET)	Unlimited tissue depth penetration Can be used for whole body imaging Detailed anatomical information can be obtained when combined with CT or MRI	Radiation exposure Low spatial resolution and long acquisition time Expensive	^{11}C ^{18}F ^{64}Cu	High energy γ-rays
MRI	Unlimited tissue depth penetration Non-ionizing radiation High spatial resolution and excellent soft tissue contrast Whole body imaging possible	Expensive Long acquisition time and limited sensitivity	Gd^{3+} SPIO, USPIO	Radio waves
Ultrasound	High spatial resolution Real time imaging with low acquisition time Highly sensitive and inexpensive	Cannot be used for whole body imaging	Microbubbles	High frequency sound
OI	High spatial resolution Real time imaging with low acquisition time Highly sensitive and inexpensive	Cannot be used for whole body imaging limited tissue depth penetration	Fluorescent dyes and molecules Light sensitive NPs	Visible or near-infrared light

Table. 1 Advantages and disadvantages of different imaging modalities for *in vivo* imaging (62).

Hereby, pre-labeling or *in vivo* targeting of particular cell types (for example, tumor cells, stem cells, immune cells etc.) is essential to understand the role of these cell types in a particular disease. Computed tomography (CT) and ultrasound (US) imaging are powerful imaging tools used both clinical and preclinical setting. CT provides x-ray based anatomical and volumetric information with high spatial resolution. CT provides contrast based on tissue density changes, for example between soft tissue, air (lungs) and dense tissue (bones), however it's soft tissue contrast is poor. CT is not only used for preclinical *in vivo* studies of lung diseases like emphysema, fibrosis etc. (63–67), but also for diseases affecting bones and joints (68–70). Studies have been conducted on the usage of gold nanoparticles for *in vitro* labeling of monocytes and their visualization by contrast enhancement *in vivo* CT imaging (71). However, high tissue

concentrations of these contrast agents are required to generate detectable signal enhancement *in vivo* using CT, raising questions on the potential cytotoxicity and clinical applicability of gold nanoparticles (72–74).

US imaging is a safe, inexpensive and fast imaging method. This modality exploits absorption, reflection and refraction of ultrasound waves to perform real time imaging with very short acquisition times. US is widely used both preclinically and clinically. However, depending on the type of tissue, it has penetration depth limitations, which restricts *in vivo* tracking of contrast labeled cells to certain organs. As contrast agents, gas-filled microbubbles can be used for labeling cells and targeting disease specific biomarkers (75). For enabling specific targeting of cells, some of these microbubbles contain avidin or streptavidin moieties which makes them immunogenic and thus restricts their clinical use (76, 77). However, other surface chemicals have been used that have overcome such biocompatibility issues (78–80). Other methods that are more frequently used for cell labeling and imaging are explained in more detail in the following sections.

1.4.1 Optical imaging

Optical imaging, utilizes a wide range of visible and near infrared light, generating and modulating properties of photons in order to create images from cells to organs and whole organisms. Various methods are used for targeting/labeling cells for optical imaging. This includes processes like fluorescence, phosphorescence, bioluminescence, photoacoustic imaging and others (81–85). Contrast in optical imaging can be generated by externally administered contrast agents but also by genes that produce optically active compounds (bioluminescent or fluorescent) inside the cell, either as a natural process (for example in fireflies) or in genetically modified organisms (86–88). External contrast can be added in the form of fluorophores like organic compounds but also peptides, proteins or fluorescent nanoparticles like quantum dots (89). The flexibility and range (wavelength of the fluorophores) of detection is an additional advantage of optical imaging. Optical imaging also aids in the visualization of immune cells like macrophage (28). The two main methods of optical imaging are fluorescence imaging (FLI) and bioluminescence imaging (BLI).

- Fluorescence imaging

Fluorescence imaging is based on the light absorbing ability of fluorescent molecules at specific wavelengths and subsequent excitation. These molecules then release photons of longer wavelength when they return to their ground state (Fig. 3). To detect these photons, sensitive CCD cameras are used in combination with dedicated filters for chosen wavelengths (90). However, the limited depth penetration by the absorption and scattering of light within tissues limits the use of FLI. As scattering depends on the wavelength, near infrared (NIR) probes are frequently used to reduce these disadvantages. Fluorescence signal can be generated using either fluorophores or reported genes (91).

Applications based on the usage of fluorophores make use of fluorescent molecule to discern the location of a conjugated probe. On the other hand, reporter gene-based strategies use Red Fluorescent Proteins, or mCherry reporter genes incorporated by direct linking with a key molecule or exploiting specific promoter. This method helps in gathering detailed information about molecular events or biological processes. In recent years, FLI gained momentum due to advancement in tailored multifunctional agents using NIR dyes to overcome the depth penetration limitations of FLI (92, 93).

Studies have been conducted for the *in vivo* immune cell tracking using FLI on non-phagocytic cells by incorporating lipophilic fluorescent dyes with minimal cytotoxic levels (4). In this regard, natural killer cells are tracked *in vivo* in human prostate cancer xenograft model using FLI but owing to photo-bleaching the quantitative tracking of cells shown was poor (94). *In vivo* labeling and tracking of NIR fluorophore-coupled T cells was performed in breast cancer mouse model (95). However, unspecific fluorescent signal was observed in organs like liver, spleen and lungs due to the migration of T cell in these organs. Briefly, depending on the location of tumor in the body, data analysis should be done carefully as, cell migration into nearby organs can lead to misinterpretation of experimental data.

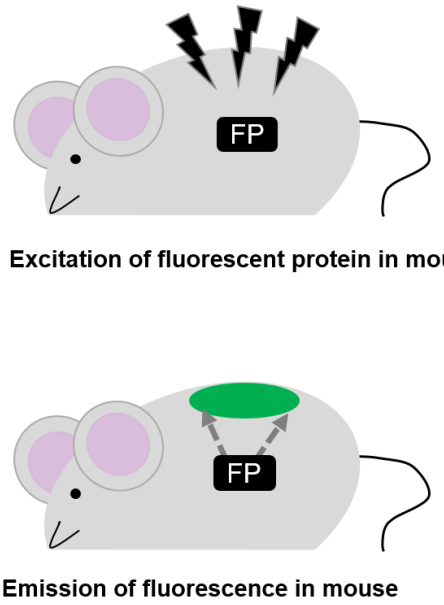

Fig. 3 Principle of fluorescence imaging. In animal models, cells carrying a fluorescent label were injected. Following the excitation of the label at a specific wavelength, photons with longer wavelength were emitted.

Another important aspect to consider before using FLI for cell tracking is the route of administration of fluorophore labeled cells, target organ and disease model. Cell labeling using NIR dye-loaded contrast agents is largely used for *in vivo* visualization and quantification of disease progression (93, 96, 97). Nanoparticle-based fluorescence contrast agents are exploited for their hydrophobicity, quantum yield and choice of different wavelengths. Mostly used nanoparticle-based contrast agents for *in vivo* FLI are dye conjugated nanoparticles, quantum dots and gold nanoparticles (98). However, for preclinical and clinical studies, cell labeling applications using quantum dots are often not opted because of their potential cytotoxicity issues (99, 100).

- *Bioluminescence imaging*

BLI is widely used noninvasive whole body imaging technique, which attributes to the emission of visible light with remarkably high signal-to-noise ratios in living organisms (101). Standard procedures of BLI includes the sensitive detection of visible light (400-620 nm) generated upon luciferase (enzyme)-mediated oxidation of luciferin (substrate) with the help of charge-coupled device (CCD) (Fig. 4). Various factors decide on the sensitivity

of the photon detection including the expression of luciferase, the location of the genetically engineered cells in the body, the accessibility of the substrate etc. (82).

The most frequently used bioluminescent reporter gene for preclinical imaging is the luciferase enzyme obtained from North American firefly (*Photinus pyralis* or FLuc) (102). Luciferases can also be cloned from jellyfish (*Aequorea*), sea pansy (*Renilla or* RLuc) and corals (103). The photons produced by firefly-luciferase requires ATP and oxygen in order to emit light. BLI signal produced by firefly luciferase at the peak emission wavelength of 560 nm can penetrate several centimeters deep into tissue.

For cell and animal imaging, the luciferase-luciferin system is ideal because the insertion of luciferase-encoding genes into the promoter region of target cell genes allows detection of an undiluted BLI signal upon cell division (104, 105). In this context, luciferase-expressing tumor cells are readily used for quantification of tumor growth and metastases detection in murine xenograft cancer models using BLI (106). This methodology has been developed over the past 10 years for *in vivo* preclinical imaging of biological process in healthy organisms and under pathological conditions (107–109). This technique offers a low cost imaging method for real-time disease analysis.

With this methodology, it is possible to perform longitudinal follow-up studies of biological processes with serial quantification by taking multiple image acquisitions. Despite of having the above-mentioned advantages, BLI faces several other issues regarding detection of signal, like dependence of the firefly luciferase-controlled oxygenation of luciferin on the adequate availability of oxygen and ATP. In case of poor administration of luciferin or improper ATP production, the measurements of BLI signal intensity may represent false data. In addition, for the acquisition of signal originating from deep tissue, attenuation of photons limits the detectability and quantification of signal.

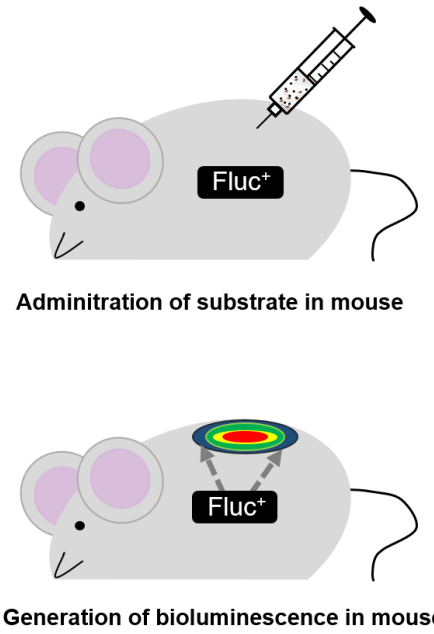

Fig. 4 Principle of bioluminescence imaging. Mouse carrying luciferase-expressing cells was injected with the substrate. In the presence of oxygen and ATP, luciferin is oxidized by luciferase enzyme, resulting in the emission of photons.

In this case, signal from the surface of the animal appears more intense compared to the signal from deeper tissues. Another limitation is the changes in the dynamics of the tissue geometry like growing tumors or formation of metastasis, which may affect the BLI signal intensity due to scattering and/or absorption of light.

For immune cell imaging, BLI is used for macrophage tracking mainly for *ex vivo* labeling of genetically engineered macrophages with the help of a lentivirus vector to encode the desired reporter gene (110). The genetically engineered macrophages were administrated intravenously and orthotopically in order to perform *in vivo* BLI. However, luciferase-labeled macrophages show a technical limitation due to poor transfection efficiency. Further, genetically engineering of primary immune cells can affect their normal biological function.

1.4.2 Positron Emission Tomography

Positron emission tomography (PET) based on the generation of positrons by a PET tracer and subsequent annihilation by meeting its anti-matter, electrons. This results in the generation of two photons with an energy of 511keV, emitted in opposite directions (180°). The emitted radiation is

captured by external detectors (scintillation crystals) positioned in a 360˚ array surrounding the object. The distribution of an isotope inside the biological tissue can be determined by drawing lines of reference of annihilation events that occur within a short coincidence time (< 10ns). In addition, of the localization of tracers, the radioactive decay of tracers is monitored (kinetic modelling).

PET offers highly sensitive detection of molecular events at sub-physiological concentrations of tracers, which makes it a popular imaging modality in clinical studies. However, the poor spatial resolution of PET (limited to mm) is a disadvantage for preclinical studies.

For the imaging of pathological process in the body, PET utilizes radiotracers, formulated with radioisotopes like ^{18}F- or ^{11}C. One of the most popular tracers is ^{18}F fluorodeoxyglucose (FDG), which is readily used in preclinical and clinical research. FDG mimics glucose and therefore, shows high uptake by the cells undergoing rapid glycolysis. FDG-PET hence allows the sensitive detection of cancer and related malignancies, inflammatory processes including neuroinflammation and infections (111–113). Detection of inflammation and infectious processes is assessed by elevated FDG accumulation, as a consequence of high rates of glycolysis and FDG uptake by inflammatory macrophages infiltrating into a site of infection (114, 115). However, PET is challenging in terms of imaging the initial phase of inflammation due to insufficient contrast between the inflamed and healthy tissues. In the field of gene and cell therapy, PET imaging also play important role where, use of radionuclide-based reporter genes has been reported in humans (116–118). These reporter genes are integrated either in cultured cells or into the genome of bacteria, fungi and animals for analysis of gene regulation using PET imaging (119). For gene therapy, kinetics are monitored *in vivo* by determining the sites, magnitude and time variability of therapeutic transgene expression. In cellular gene therapy, kinetic studies are performed by tracking the locations of genetically engineered therapeutic cells, measuring their quantity at each location and time dependent follow-up of changes in their characteristics post administration (120). However, immunogenicity is an issue using reporter genes which can be a detrimental factor related to the success rate of therapeutic cell expression after their adoptive transfer. Another limitation for clinical translation is efficient delivery of PET reporter genes into the primary cells that cannot be ex vivo cultured for longer time (121). Therefore, safe and stable PET reporter gene studies are required with high sensitivity and non-immunogenicity.

1.4.3 Magnetic resonance imaging

Magnetic resonance imaging (MRI) also known as nuclear magnetic resonance (NMR) is based on the intrinsic magnetic properties of the tissue. MRI can provide excellent soft tissue contrast together with very high spatial resolution. Using multi-parametric approach, MRI provides information related to function (fMRI), metabolism (MR spectroscopy), blood flow (MR angiography), perfusion (DCE MRI), tissue connectivity (DTI) etc., (122–127).

1.4.3.1 Proton Magnetic Resonance Imaging

MRI is based on the NMR effect discovered by Bloch *et al*. and Purcell *et al*. in 1946 (128). They described that isotopes with a nuclear spin align parallel or anti-parallel to an external magnetic field. Transition between the different energetic states (parallel and anti-parallel alignment) is possible by a radio-frequency (RF) pulse. The measurement of NMR effect exploits the nuclei with a nonzero magnetic moment like hydrogen (^{1}H), phosphorus (^{31}P), carbon (^{13}C), fluorine (^{19}F) etc., an external static magnetic field (B0) and a time-varying RF field (B1). In case of no external magnetic field, the protons/spins in the respective isotopes align in random orientation with no net magnetic moment. When B0 is applied to the tissue, all the protons align parallel or anti-parallel to B0. After a short RF pulse is applied, the net magnetization will be disturbed. For example, a RF pulse corresponding to a flip angle of 90° will induce precession of spins around the B0 field with a resonance frequency so called, Larmor frequency. The Larmor frequency is also directly proportional to B0. During the precession, nuclei enter in the relaxation phase to achieve thermal equilibrium, which is composed of two main components called spin-lattice (T1) and spin-spin (T2) relaxation times.

These relaxation times are responsible for generating MR contrast based on the chemical and physical composition of the object, which also changes in healthy and pathological state. The T1 relaxation time is the time required for restoring the longitudinal magnetization back to it's thermal equilibrium state. In contrast to T1, T2 relaxation time is the process of dephasing of the net transverse magnetization including, dephasing between different spins. In order to generate high MR contrast in images, the abundance of protons in the tissue, their interaction with the nearby chemical environment and the strength of external magnetic field need to be considered.

1.4.3.2 Proton MR exogenous contrast agents

Externally added agents, so called contrast agents, can affect the T1 and T2 relaxation in a sample and hereby help in enhancing the visibility of desired tissue (129). Contrast agents mainly affecting T1 relaxation are frequently referred to positive contrast agents while agents mainly affecting T2 relaxation are referred to as negative contrast agents. Most of these agents mainly affect relaxation times of protons. They can be used for targeting specific cell types after labeling. For MRI, T1-weighted (hyper-intense signal) and T2 weighted (hypo-intense signal) images are produced adjusting echo times, inversion times and/ or repetition times of MR protocols, so called MR pulse sequences (130, 131). Here, we will discuss two main categories of proton-affecting contrast agents for MR imaging.

- *Superparamagnetic nanoparticles*

  These contrast agents are typically formulated in the form of iron oxide nanoparticles with coatings to make them biocompatible, for example using polyethylene glycol, dextran, heparin, albumin and lipid shells like liposomes (132). Superparamagnetic particles of iron oxide (SPIOs) shorten T2/T2* relaxation times of surrounding protons. SPIOs also have a strong T1 effect but even stronger T2/T2*. They cause reduced (hypo-intense) MR signal intensity in T2-weighted images. Based on the diameter of the iron oxide nanoparticles, they can be categorized as small superparamagnetic iron oxide (SPIO) nanoparticles with core size of <1µm and ultra-small superparamagnetic iron oxide (USPIO) nanoparticles with core size <50nm (133, 134). SPIO nanoparticles are sensitive and capable of detecting labelled single cells in MR images and were successfully used in clinic for cancer imaging, bowel imaging and myocardial imaging (135, 136).

  Despite of the popularity, many of the clinically approved SPIO nanoparticles are removed from the market and thus are no longer available for diagnostic MR imaging. For *in vivo* preclinical MR imaging, SPIO nanoparticles are widely used for cell labeling and tracking in animal models (137–139). For immune cells labeling, various coatings of SPIO nanoparticles are formulated and tested (140). Homing of SPIO nanoparticles-labeled macrophages after intravenous injection in animal model of renal ischemia was tracked using MRI (141). For cancer immunotherapy, dextran-coated SPIO nanoparticles were used

for improved T cell labeling in order to monitor their time-dependent recruitment towards the tumor after adoptive transfer in animals (142, 143).

- *Paramagnetic contrast agents*

  These contrast agents are composed of metal ions that have unpaired electrons exhibiting permanent magnetic moment. Interaction of the magnetic moment of paramagnetic atoms with much smaller magnetic moment of the protons in adjacent water molecules reduces their T1 and T2 relaxation times. . Two well-known paramagnetic ions are Gadolinium (Gd) and manganese (Mn). Gadolinium metal ion is a lanthanide and can cause potential toxicity in its ionic form. Therefore, it is chelated with an organic ligand before administration to animals and humans. Gd-chelates have been introduced to the clinic in 1998 for diagnostic MR imaging in the form of intravenous injections. Apart from applications in oncology (for example, detection of brain tumors), Gd-chelate nanoparticles are also used as blood pool agents for contrast enhanced MRI of tissue vasculature (144). Mn is also a T1 contrast agent, which gives hyper-intense signal in T1-weighted MR imaging. This metal ion interacts with the surrounding water in the tissues and increases the MR signal intensity of the region with highest uptake of Mn-based nanoparticles (145). Mn based contrast agents have been used for the detection of hepatocellular carcinoma where, the degree of Mn-based nanoparticles in the desired tissue corresponds to the tumor growth (146). Mn ions have also been used in preclinical studies for validating functional connectivity by using its analogy to calcium and hereby visualizing transport across functioning synapses (147). Similarly to Gd, toxicity of free manganese is a concern (148).

Recently, magnetic nanoparticle-based monitoring of cancer therapies are gaining momentum by tracking the location of engrafted immune cells by *in vivo* MRI (3, 149, 150). This aid in the longitudinal visualization and quantification of immunological processes occurring in the pathological environments. Migration of immune cells like DCs towards the draining lymph nodes can be traced over time by MRI, after labeling them with an efficient magnetic contrast agent (151).

Proton-based MRI utilizes contrast agents like SPIO for indirect quantification of signal by altering the chemical environment of the surrounding tissue to generate local contrast. Despite of having several advantages of these paramagnetic and superparamagnetic compounds, they lack high specificity. In many cases, it becomes difficult to distinguish between the injected labeled cells and the background signal because intrinsic contrast. This is in particular the case for SPIOs and USPIOs where, the hypointense contrast can be mistaken for disrupted vasculature (hemorrhage) or formation of scar tissue. This gives rise to unambiguous MR signal in images and thus affects the correct interpretation of MRI data.

In order to overcome this problem, it is desired to have a MRI nucleus with low biological availability to reduce unspecific signal. Other MR detectable nuclei such as ^{19}F and ^{13}C are also of high interest for cell labeling and tracking applications thanks to their direct signal quantification and signal specificity due to the lack of intrinsic background signal in living body.

1.4.3.3 Fluorine-19 Magnetic Resonance Imaging and Spectroscopy

Soon after the first proton-based MR image was presented by Lauterbur, proton-based MRI entered the clinic for the diagnosis of diseases by exploiting distinctive relaxation times of healthy and diseased tissue (152). Apart from the high natural abundance of hydrogen atoms in the form of water present in body, other nuclei also drew attention for MRI. In this context, first report released in 1977 by Holland *et al*. reported on fluorine-19 magnetic resonance imaging (^{19}F MRI) using glass tubes filled with sodium fluoride (NaF) and PFTA (perflurotributylamine) as potential fluorine contrast agents (153). This represents an early report on the availability of MRI contrast agents in the form of fluorinated compounds. Holland *et al*. discussed the similarity between the gyromagnetic ratios of ^{1}H and ^{19}F nuclei, which helps in acquiring MR images at two different but not too distant frequencies using the same imaging set-up.

The fluorine nuclei is of high interest for MRI applications because the sensitivity of the fluorine nucleus is 83% relative to proton, resulting in the signal-to-noise ratio of approximately 88% of that of proton per nucleus (154). It has a ½ spin quantum number, high stability and 100% abundance in nature. However, the signal-to-noise ratio (SNR) depends on several factors, which should be taken into account in order to achieve high ^{19}F MR signal intensity from the desired region (Fig. 5).

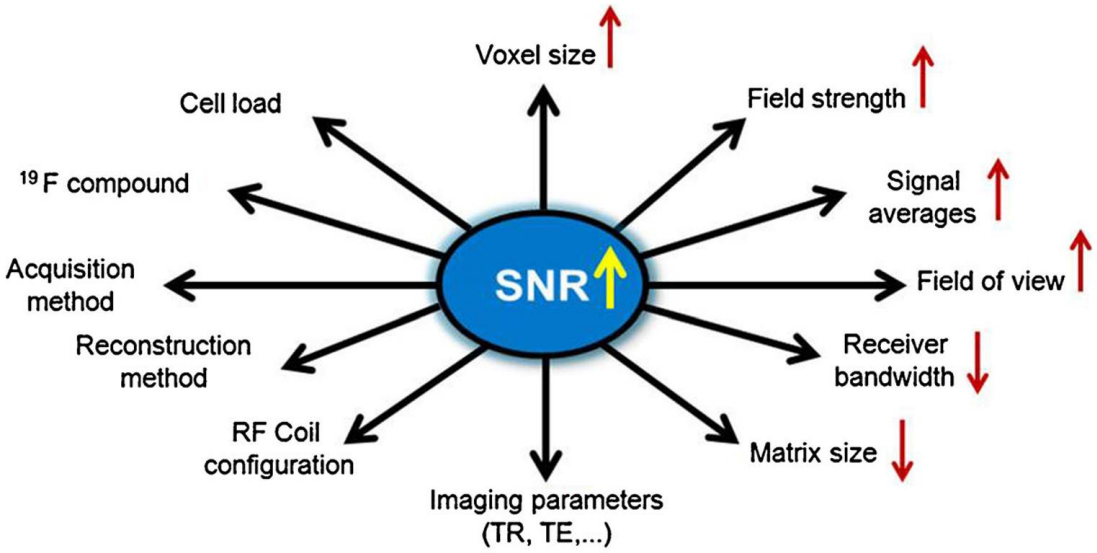

Fig. 5 Dependence of SNR on different factors for ^{19}F MRI, showing upward arrow for increase and downward arrow for decrease in the SNR (155).

Fluorine atoms are normally present in teeth and bone but despite of their high fluorine concentration they are not detectable by conventional MRI due to their immobile nature (solid compounds). This results in extremely short T2 relaxation time making their detection difficult by using standard spin-echo or gradient-echo ^{19}F MRI. Therefore, external administration of fluorinated contrast agents is needed in order to generate ^{19}F MR signal from living objects. This has the advantage that there is no MR-detectable background signal in ^{19}F MRI, which helps in the direct and specific measurement of contrast agent' uptake in the region of interest. For ^{19}F MRI, fluorine MR signal is usually acquired by using a dual-tuned surface or volume radiofrequency coils, which can be tuned to both ^{1}H and ^{19}F frequencies.

With the help of such coils, proton and fluorine images can be obtained sequentially, with similar image/slice geometry. To locate the origin of fluorine MR signal, ^{19}F MR images are directly overlaid on the ^{1}H MR images during data post processing (Fig. 6).

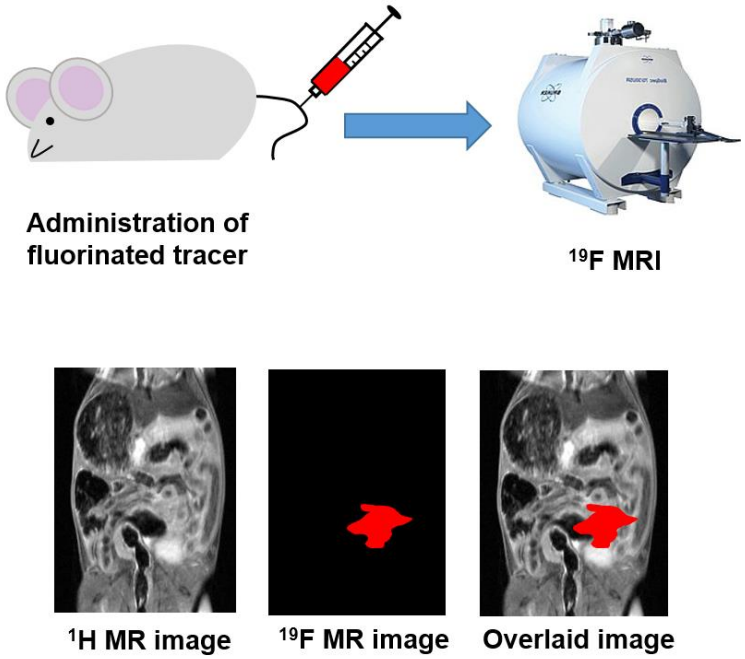

Fig. 6 ^{19}F MR imaging after administration of fluorinated contrast agent in an animal model (above) and data post processing of acquired fluorine MR signal after the overlay on anatomical MR images, for the localization of the fluorine MR signal (below).

In order to perform metabolic assessment of fluorinated compounds, another powerful technique, fluorine magnetic resonance spectroscopy (^{19}F MRS) is used. This method allows highly specific examination of fluorine containing drugs and their chemical byproducts. The assessment of different fluorine containing drugs *in vivo* and *ex vivo* can be performed using ^{19}F MRI/MRS (154). Hereby, the chemical structure, catabolism and pharmacokinetics of a drug can be assessed in the biological environment. Despite of being a sensitive and specific tool, binding of certain drugs with plasma proteins like fluoxetine, limits the pharmacokinetic quantification of drugs using ^{19}F MRS. As a result, of such bindings, the very short T2 relaxation time does not allow the detection of these compounds by ^{19}F MRS. Although being of similar sensitivity as ^{1}H MRI/S, ^{19}F MRI is limited by the concentration of the fluorinated compounds. Local concentrations in the mM range are required to achieve detection by ^{19}F MRI.

- *Chemical compounds as contrast agents for ^{19}F MRI/^{19}F MRS*

As mentioned above, both ^{19}F MRI and ^{19}F MRS can be used for studying biological processes using fluorinated contrast agents. One of the early biological applications of ^{19}F MRS tool was

the investigation of 5-fluorouracil (5-FU) for its pharmacokinetic properties in cancer treatment in the late 1970s and early 1980s (156, 157). 5-FU is an antineoplastic cancer drug in patients receiving chemotherapy. ^{19}F MRS of 5-FU was first reported first by William E. Hull *et al*. back in year 1988 (158). The ^{19}F MRS measurements were conducted using *ex vivo* samples in an 11.7T MR spectrometer. As a potential anticancer drug, 5-FU has been tested for the neoplasm disorders of the colorectal system, the head/neck, breast cancer and others (159–161). Capecitabine, a protodrug is formulated to apply intrinsic toxicity of 5-FU to achieve its high deposition in cancerous region with minimal availability in healthy tissue (154). In this regard, ^{19}F MRS can provide in-depth understanding of the drug metabolism and its cytotoxic activity.

For ^{19}F MRI, various fluorinated compounds are used for the generation of the ^{19}F MR signal (162). In addition, fluorinated gases can be also used to generate ^{19}F-based contrast in preclinical and clinical studies (Fig. 9). The most commonly used fluorinated gases are sulfur hexafluoride (SF_6), hexafluoroethane (C_2F_6) and fluoropropane (C_3F_8) (163).

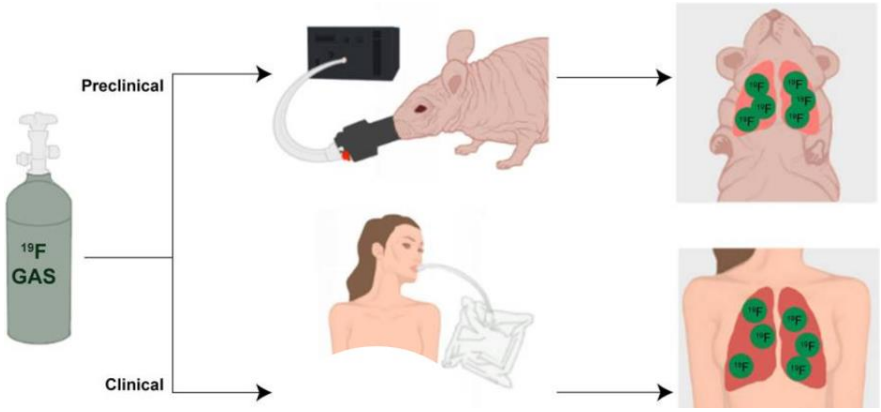

Fig. 7 Preclinical and clinical applications for functional ^{19}F MRI using fluorinated gases after inhalation (164).

For the preclinical and clinical practice, SF_6 fluorinated gas could be used together with the halothane [CF(3) CHBrCl] for anesthesia (165). Hereby, ^{19}F gases could also be used for functional assessment of lungs by ^{19}F MR imaging because they offer direct measurement of airspace sizes, lung capacity, ventilation and perfusion ratios (Fig. 7) (166–171). Imaging of lung cancer was demonstrated by using PFC nanoparticles with the help of multimodal imaging (172).

- *^{19}F MRI for cell labeling and tracking*

Another category of fluorinated compounds are perfluorocarbons (PFCs), which have gained high interest for ^{19}F MRI applications. PFCs are highly inert and stable compounds, which show immiscibility not only in lipophilic solvents but also in hydrophilic solvents. Due to their high density, they are also used in eye surgery to keep the retina 'fixed' to one location. They are also used as vehicles for targeted drug delivery and as contrast agents for ultrasound in the form of microbubbles (173).

Their original application was the use as blood substitutes due to their oxygen transfer property from the red blood cells to tissues (174). PFCs show potential for cell labeling applications in combination with other modalities. Thanks to their oxygen carrying capacity, they can be used for the measurement of percentage oxygenation in cells after labeling (154). For example, PFC nanoparticles can be targeted to a specific cell type to study the oxygen content in the region(s) of interest. PFCs were also applied for liquid ventilation as a therapy for different respiratory disorders (175). They can also be used as aerosols in order to aid effective gas exchange in acute respiratory distress syndrome. Since PFCs have been in use both clinically and preclinically, they offer also a safer means for cell labeling and targeting with potential of translation into the clinic.

For PFCs to be an efficient labeling agent, it is important to have high ^{19}F density per molecule for high detection sensitivity *in vivo* after sufficient cell loading with the fluorinated contrast agents. Therefore, to be able to qualify as a promising fluorinated contrast agent for cell labeling, certain requirements needs to considered before planning experiments. Some of these essential check-points are as follows:

a. Assembly of high number of chemically equivalent fluorine atoms
b. No cytotoxicity including effects on cell functions
c. Formulation with choice of surfactants to facilitate labeling of non-phagocytic cells
d. High stability in biological media
e. If possible, possess a single resonance in the ^{19}F MRS to avoid chemical shift displacement effects
f. Should have relatively short T1 and long T2

g. Oxygenation-sensitive fluorinated contrast agents should be checked before measurement of engrafted cells *in vivo*

h. Clearance of the particle from the body should be considered

Mostly PFCs are used in the form of emulsions because this increases the high content of PFC per droplet and makes its formulation easier for the manufacturer. Emulsions are a mixture of an immiscible compound encapsulated by a surfactant to make droplets relatively stable in water. It is therefore, crucial for the formulation of stable PFCs to remain dispersed. They should not disintegrate from the solvent. The synthesis of PFC emulsions for preclinical applications requires careful analyses, if incorporation of additional chemical moieties like fluorescent antibodies or dyes is needed.

For *in vivo* applications, the chance of detachment of these additional tags in PFC emulsions is high due to interaction with the blood pool proteins. Since fluorine is highly electronegative, assembling ^{19}F nanoparticles can alter their chemistry. Therefore, metabolism of these contrast agents must be taken into account for *in vivo* cell labeling experiments. For quantification of fluorine nanoparticle-labeled cells, it is assumed that the MR signal is generated only from the injected cells and that detachment of the fluorine label in the extracellular space is negligible. To make a precise estimation of labeled cells *in vivo*, a reference with known fluorine concentration should be kept close to the animals in a preclinical setting.

There are various types of PFCs for the cell labeling reported like perfluorooctyl bromide (PFOB), perfluoropolyethers (PFPE) and perfluoro-15-crown-5-ether (PFCE) (154). As a promising fluorinated agent, PFCE is preferred as it offers high fluorine load of 20 chemically and magnetically identical fluorine atoms, producing a single peak in ^{19}F MRS. For the synthesis of these emulsions, mostly phospholipids (safe for cells) and poloxamers (aid in drug delivery) are used (176).

Various factors affect the efficiency of cell loading with the fluorine emulsions, including but not limited the choice of the contrast agent, cell type, labeling method and overall cellular uptake. In order to get correct quantification from ^{19}F MR images, it is of high importance that the mean cellular uptake of contrast agent is reproducible. For the *in vivo* labeling, most

importantly the ^{19}F agent must be well tolerated by the plasma proteins and should avoid the formation of a protein corona (177). However, for *ex vivo* labeling methods, the incubation time, surface coating of cell plates, washing steps and culture medium are very important to enhance cell-nanoparticle interaction for increased uptake. The use of fluorinated tracers/nanoparticles for labeling different cell types was also shown for mesenchymal stem cells, beta cells and hepatocytes (178–181).

Some cell types are easier to label with fluorinated contrast agents/nanoparticles like phagocytic cells for e.g. macrophages, monocytes, dendritic cells etc. These phagocytic cells take up the nanoparticles during their normal endocytic pathway, a hallmark of their antigen presenting property. On the other hand, labeling of non-phagocytic cells is far more challenging and requires further modification of fluorinated contrast agents like using positive lipids, antibodies or transfections agents in order to facilitate labeling (182, 183).

In this thesis, we will focus on the tracking of both phagocytic and non-phagocytic immune cells and their labeling strategies using modified PFCE nanoparticles with the help of ^{19}F MRI in different disease models.

- *Applications of in vivo ^{19}F MRI for tracking of immune cells*

Use of PFCs for cell labeling and tracking was first reported in the year 2005 by Ahrens *et al*., where they showed the capability of these nanoparticles in tracing the cells used in immunotherapy (184). As mentioned above, phagocytic immune cells are of high interest for cell labeling and tracking because of their biological relevance, ease of labeling and migratory properties.

PFCE nanoparticles have been studied for *in vivo* labeling of macrophages after injecting them intravenously and tracking the migration of circulating immune cells using ^{19}F MRI (Fig. 8). In this procedure, the patrolling immune cells mainly, macrophages/monocytes engulf the fluorinated nanoparticles and infiltrate into the inflamed organ (185). Different inflammatory conditions are elucidated with this methodology in order to follow the immune response in various diseases after systemic injection of fluorine nanoparticles (186).

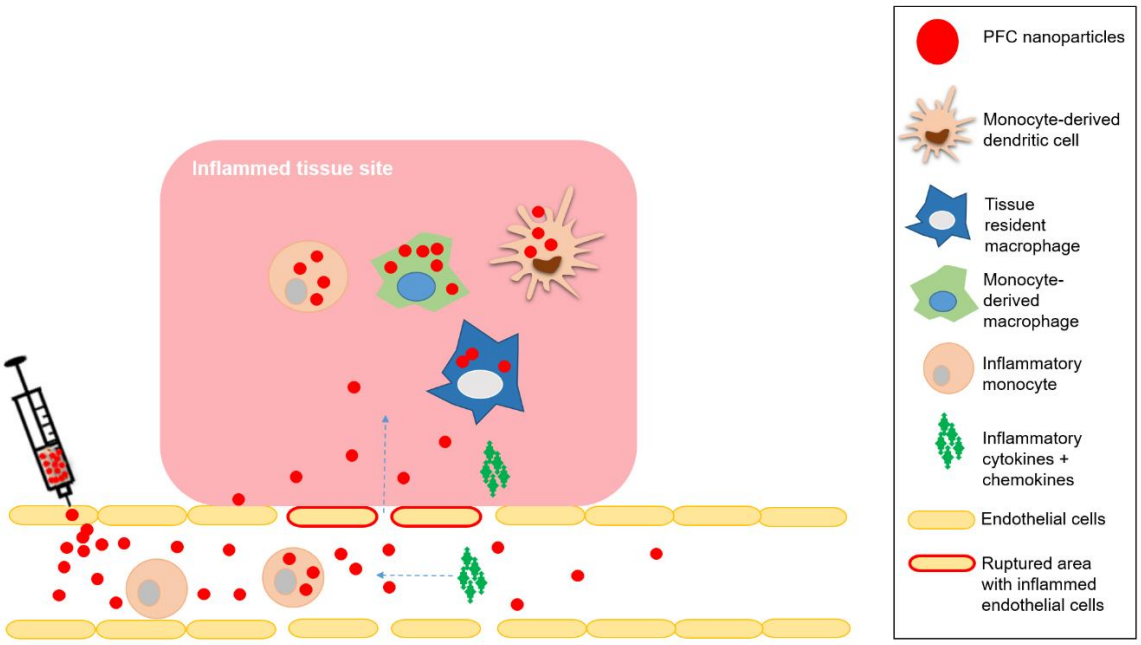

Fig. 8 *In vivo* labeling of phagocytic immune cells after the intravenous administration of PFC nanoparticles after the inflammatory trigger post injury.

Thanks to the long blood half-life of PFCE nanoparticles, their retention in blood circulation allows sufficient time for phagocytic uptake. To name a few, cardiac and cerebral ischemia, myocardial infarction, pneumonia, bacterial abscess formation, peripheral nerve injury, and rejection of donor organs after transplantation have been studied (187–193). For quantification of the ^{19}F MR signal in a particular region of interest, it is assumed that the fluorine signal, marked as fluorine 'hotspots' in ^{19}F MRI image is directly proportional to the number of PFCE labeled macrophages (194, 195).

For *ex vivo* labeling of primary immune cells before their *in vivo* engraftment, methods have been established for tracking T cells and dendritic cells (DCs) using ^{19}F MRI (182, 184). For the tracking and quantification of adoptively transferred T cells, *ex vivo* labeling strategies using perfluoropolyether (PFPE) nanoparticles were applied in a mouse model of type 1 diabetes (196). Dendritic cells are also widely studied for clinical applications in humans where human DCs were labeled with PFCE nanoparticles and their draining to lymph nodes was monitored in patients (197). ^{19}F MRI offers tremendous potential for the visualization and quantification of immune cells to estimate the degree of inflammation. This will help not only for the early detection of diseases but also for time-dependent intervention in cell therapies. With the help

of this imaging technique, clinical studies can also be performed thanks to the rapid development in the field of contrast agent development and ^{19}F MRI. For example, dedicated coils have been tested successfully in patients (198).

However, the translation of ^{19}F MRI cell imaging techniques from preclinical to clinical applications poses certain challenges, which also need to be addressed (155). This includes critical analysis of the hardware requirements, imaging sequences and parameters. While PFCs are already used in clinical practices and proven to be a safe, fluorine contrast agents should also be developed for example, with drug loading capacities and high fluorine concentrations. Therefore, we can conclude that cell labeling and tracking studies using ^{19}F MRI shows high potential for dynamic *in vivo* immune cell monitoring.

1.5 Diseases models

In this thesis, we focused on two different disease models, for noninvasive assessment of the interplay between immune cells and pathological processes by using ^{19}F MRI together with other molecular imaging techniques.

1.5.1 Invasive Pulmonary Aspergillosis: a fungal infection

With the increase in resistance to antimicrobial therapy, infections are an increasing problem worldwide. Therefore, early diagnosis and follow-up of therapy are important. Infectious diseases relate to the host immune system. Interaction between immune cells and pathogens decide on the progression of infections. A pathogen e.g. bacteria, viruses or fungi is a microorganism recognized by the body's immune system as an intruder, being recognized as a threat to the biological system and potentially causing infections.

Among others, infections caused by fungi have a broad spectrum of manifestations ranging from topical infections to lethal reoccurring infections in humans (199). *Aspergillus fumigatus* is the most studied filamentous fungal species due to it is ubiquitous nature and high natural abundance in air, water, soil, dead animals and decaying vegetation (200, 201). *A. fumigatus* can produce thousands of conidia in the air, which upon inhalation by immunologically challenged patients can spread in the lungs and penetrate the airways (Fig. 9). Depending on the immune status of humans, *A. fumigatus* can be cleared from the body or spread to other organs, causing

aspergillosis (202–204). A potentially lethal medical condition is the manifestation of *Aspergillus* species in the pulmonary region of immunocompromised humans and it's further invasion, also known as invasive pulmonary aspergillosis (IPA). Approximately 90% of IPA cases in humans occurs due to *A. fumigatus*.

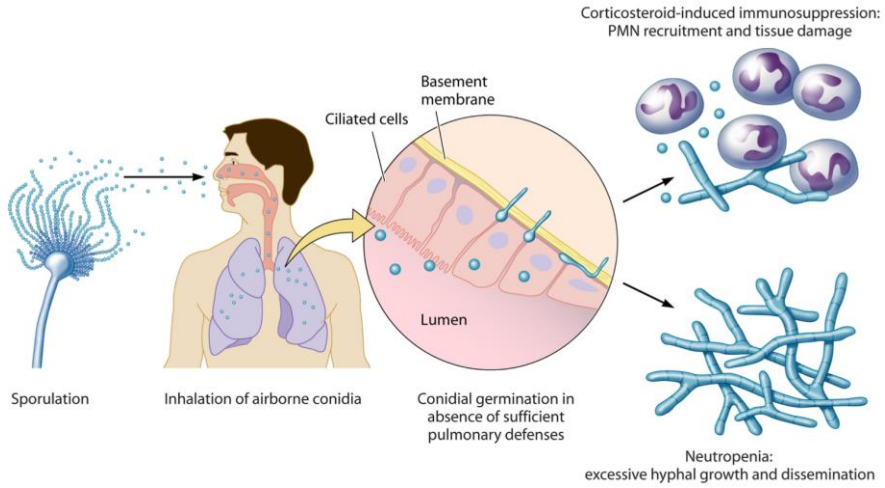

Fig. 9 *A. fumigatus* induced airborne infection through inhalation of conidia with pulmonary manifestations in immunosuppressed patients. Response to the *A. fumigatus* conidia in the lungs depends on the immune status of patients, which can lead either to the massive inflammation upon PMN recruitment or severe dissemination due to lack of neutrophils (205).

- Host-pathogen interactions

Like for any other infection, innate immune cells play a pivotal role in combating this fungus, by inducing a first line antimicrobial defense. The polymorphonuclear cells like macrophages, dendritic cells, neutrophils play significant role in the prevention of *A. fumigatus* infection. Hereby, the fungal cell wall is recognized by immune cells using different surface-bound and soluble pattern recognition receptors (PRRs). The initiation of a proinflammatory response starts with the resident macrophages of the lung to begin the phagocytic processes of clearing up to $>10^8$ viable conidia per day (206). In individuals with a functioning immune system, macrophages sufficiently clear the fungal conidia inhaled by the subject but sometimes few conidia succeed in invading the lung tissue by hyphal germination. To combat this situation, neutrophils come into play with their effector mechanism, contributing to the chemotactic elimination of fungal hyphae to prevent further invasion into the tissue. The formation of

neutrophil extracellular traps (NETs) are essential in order to prevent the spreading of the fungus in tissues by trapping the germinating conidia (207). However, if the fungal burden is frequent or profound then the adaptive immune system consisting of CD4+ and CD8+ T lymphocytes also participates in the fungal elimination. This shows that a fully functioning and active immune system is crucial for the prevention of aspergillosis (Fig. 10).

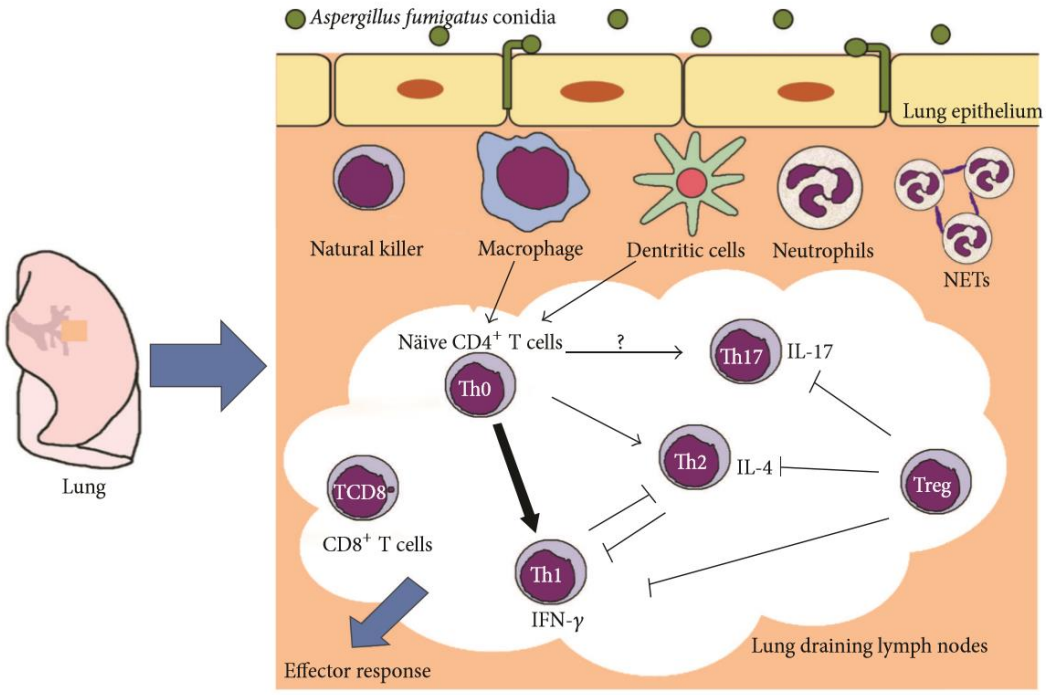

Fig. 10 Interaction of fungal spores with immune components after pulmonary *A. fumigatus* challenge with a subsequent activation of the host's immune system (208).

With an increase in the number of immunocompromised patients worldwide due to HIV, congenital immune impairments, hematological malignancies and organ transplantations, IPA cases are also increasing. Clinically relevant immunosuppressive drugs used for patients are either glucocorticosteroid-based or are DNA alkylating agents like cyclophosphamide.

- *Glucocorticoid-based immunosuppression*

Glucocorticoids are complex immunosuppressive inhibitors of inflammatory processes, which work by inducing immunodeficiency (206). These inhibitors block the transcription factors responsible for the immune response by impairing the immune function of nearly every cell type. Hydrocortisone acetate belongs to the family of glucocorticoid and is widely used for

immunosuppression in patients. Together with inducing reversible lymphopenia and monocytopenia, hydrocortisone also reduces the number of circulating CD4+ T lymphocytes (209). Hydrocortisone acetate tremendously decreases the phagocyte function impair cytokine and reactive oxygen species (ROS) production of the immune cells. Impairment of phagocytic cells like macrophages strongly reduces their capability for killing fungal conidia. However, neutrophils remain unaffected. The subsequent heavy recruitment of neutrophils at the site of fungal infection can result in lethal exacerbated inflammation and massive tissue injury.

- *Cyclophosphamide-based immunosuppression*

Cyclophosphamide belongs to the group of oxazaphosporines and is the oldest anticancer drug used in the clinic for more than 40 years. It is a cytotoxic drug mostly used in patients with hematological malignancies and patients receiving hematopoietic stem cell transplantation (210–213). Cyclophosphamide possess antimitotic and antireplicative effects. It is very important to optimize and schedule the dose of cyclophosphamide depending on the specific application. High-dose therapy of this drug is capable to eradicate the hematopoietic cells completely while the low-dose selectively acts on the T cells (214). The modus operandi of cyclophosphamide-induced immunosuppression differs largely from the glucocorticoids. It works by conjugating with DNA, hinders cellular replication and reduces the number of circulating white blood cells, mainly neutrophils.

Neutrophils play a pivotal role in the prevention of fungal invasion and therefore, their depletion due to administration of cyclophosphamide increases the risk of IPA. Therefore, neutropenia can be a life-threatening situation in most patients after exposure to *A. fumigatus* conidia (215).

Different types of host responses occur under different immunosuppressive regimen upon *A. fumigatus* infection. Therefore, it is of high importance to noninvasively study the immune cell-host interaction in a time dependent manner to understand the distinctive immune reactions against IPA.

1.5.2 Type 1 diabetes: an autoimmune disorder

Type 1 diabetes mellitus (T1D), also known as juvenile diabetes is a complex and chronic autoinflammatory disease (216, 217). With the increasing number of T1D patients worldwide, one in 300 people in the US is suffering from this autoimmune disorder. Type 1 diabetes increases the risks of developing other organ-specific autoimmune diseases like thyroid disease (218). The exact triggering mechanism of T1D is still not fully revealed however, it has been reported that genetically predisposed people are more prone to develop diabetes upon exposure to certain environmental factors. Other than this, viruses like enterovirus, rotavirus and rubella are considered as prime suspects for triggering T1D (219–221).

As a normal physiological function of immune system, immune cells can differentiate between foreign and self-antigens (222). Sufficient checkpoints in thymus are responsible for the central tolerance and take care of the elimination of self-reactive T cells. This mechanism can go wrong with escaping auto reactive T cells in the blood. Like many other autoimmune diseases, both genetic and environmental factors can trigger the autoimmune components of T1D by sending signals to the autoreactive T cells where, the immune system fails to suppress the immune response against auto antigens (223, 224). The self-destruction of the islet antigen specific beta cells in pancreas also influences impairment of the peripheral tolerance operated via peripheral tissue antigens in the lymph nodes.

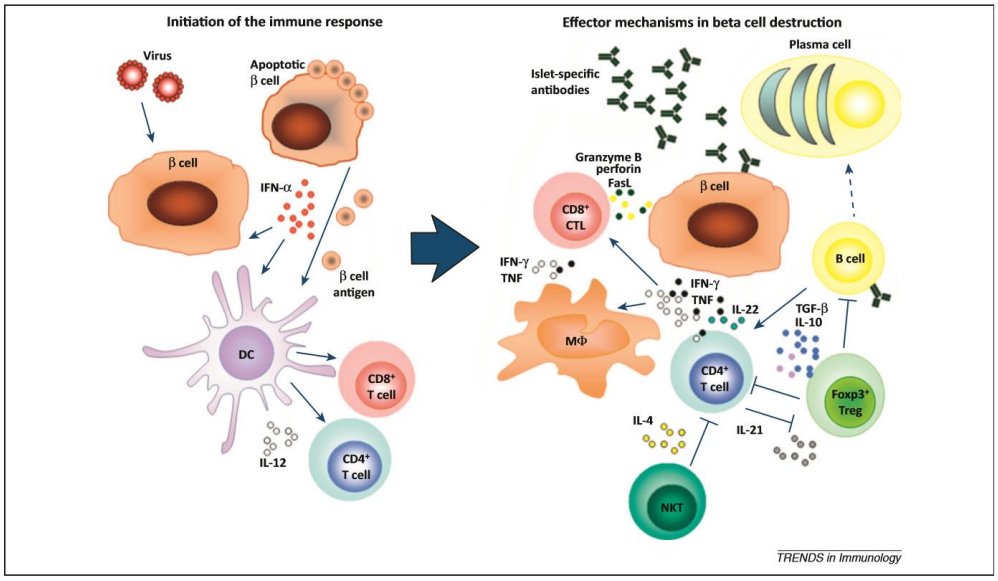

Fig. 11 Immune mechanisms involving different immune cells in the destruction of insulin producing pancreatic beta (β) cells (223).

As a proinflammatory response, hampered immunological tolerance against insulin producing beta cells causes insulitis by recruiting the inflammatory infiltrate in pancreas (Fig. 11). High infiltration of lymphoid cells like CD4+ and CD8+ T cells together with macrophages and dendritic cells, destroy 90% of islets by the time T1D is diagnosed (225). The lack of insulin producing beta (β) cells in the islets results in the elevated blood glucose level. External administration of insulin via subcutaneous injections or insulin pump is then required. T1D in itself leads to other complications like blindness, metabolic syndrome and risk of cardiovascular diseases, diabetic kidney disease etc. (226, 227).

Current diagnosis of T1D in individuals is performed routinely by laboratory testing of islet-specific autoantibodies in the blood. As a successful therapeutic approach, pancreatic transplantation has proved to be a boon to patients suffering with T1D. However, like many other organ transplants, patients are required to have lifelong immunosuppression. Alternatively, patients are injected with donor islets into the liver with mixed results where, success rates of 80% at 1 year and 20% at 5 years have been reported (228). It is important to note that both quality and quantity of islets are responsible for the success rate of these treatments in TD patients.

As established treatment cannot fully prevent the disease associated complications, novel strategies targeting the underlying immune response to cure or at least delay the onset of the disease, would be very valuable. Such treatments require fine-tuning of the immune system's own mechanisms to tolerate the autoreactive immune cells thereby restoring β-cell function. However, the non-invasive assessment of the immunological processes in the pancreas are currently not assessable. While some progress has been made for the non-invasive visualization of β-cells in pre-clinical settings, the interplay between immune cells (229) and β-cells can only be visualized by invasive imaging techniques (230, 231). The potential value of non-invasive imaging to study interactions between β-cells and immune cells includes monitoring the dynamics of cellular processes and disease progression particularly, in preclinical models of diabetes. Most of our knowledge related to T1D pathogenesis comes from experimental mouse models such as non-obese diabetic (NOD), which is a well-established model for studying autoimmune diabetes. Using these models together with noninvasive imaging techniques will potentially improve our understanding of T1D and the dynamics of inflammatory processes. In addition, *in vivo* imaging provides an efficient way to assess new therapeutic strategies.

CHAPTER 2

Objectives of thesis

Main objectives of the thesis

Immune cell tracking is one of the crucial tools, which can be extensively exploited in order to gain better understanding of diseases pathogenesis and therapy. In this context, imaging migration of immune cells towards sites of injury after labeling cells with suitable contrast agents can provide valuable biological information. Visualization of migratory pattern of immune cells using dynamic noninvasive imaging techniques have been studied using various molecular and anatomic imaging techniques.

While molecular imaging techniques including magnetic resonance imaging (MRI), have been used for labeling and tracking of different immune cells using paramagnetic and superparamagnetic contrast agents, it lacks specificity due to the lack of background-free biological information. It was the objective of this thesis, to explore the potential of fluorine magnetic resonance imaging (^{19}F MRI) as an emerging modality for *in vivo* monitoring of cell migration without any background interference from the surrounding tissue. Hereby, three different immune cell populations (macrophages, dendritic cells and T cells) were used to test specific advantages and limitations of different imaging approaches.

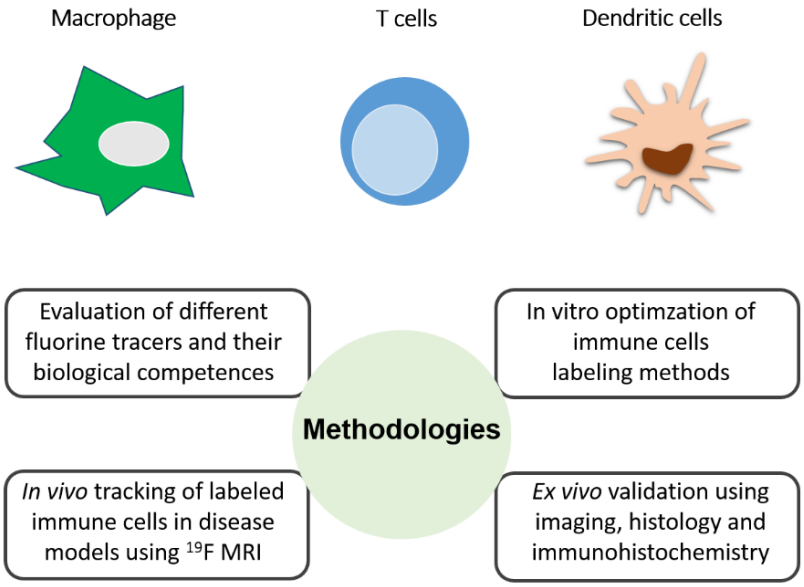

Summary of experimental workflow conducted on three different immune cell types.

To facilitate the labeling procedures, we used different fluorinated contrast agents that were specifically developed and synthesized by our collaborators at the University of Gent (Belgium). Various modifications have been made to the PFCE-NPs to optimize these contrast agents for the respective cell types, discussed in the method section of research chapters.

The overall goal of this thesis was to:

- optimize, validate, follow and quantify fluorine nanoparticle-labeled immune cells in murine models of different diseases where, inflammatory processes play crucial role by using ^{19}F MRI
- better understand the pathogenesis of different diseases for the improvement of disease diagnosis and (immune)cell-based therapies

Chapter 3

In this chapter, the main aim was to optimize labeling of macrophages using newly synthesized zonyl perfluorocarbon-based nanoparticles (ZPFCE-NPs) for their *in vivo* tracking in mouse models. For the same, we developed *in vitro* macrophage labeling protocols with ZPFCE-NPs at various time points using different concentrations. We investigated the biocompatibility of these nanoparticles for the *in vivo* labeling of macrophages after systemic administration in fungal mouse model of invasive pulmonary aspergillosis using ^{19}F MRI. Two clinically relevant models of IPA were evaluated for the *in vivo* longitudinal noninvasive quantification of inflammatory infiltrate in murine lungs. Using multimodal imaging platform by combining BLI and FLI with ^{19}F MRI, we studied dynamic profile of macrophages and other immune cells labeled with ZPFCE-NPs at different disease time-points.

Chapter 4

In order to track and investigate the migration of autoimmune T cells in type 1 diabetes mouse model, we optimized T cell labeling using different concentrations of lipid modified PFCE-NPs. Development and optimization of *in vitro* labeling protocols of T cells was performed using lipid modified PFCE-NPs in order to achieve sufficient labeling for *in vivo* detection in ^{19}F MRI. Pre-labeled T cells were adoptively transferred in type 1 diabetes mouse model for their time-dependent follow-up with the help of ^{19}F MRI where, we observed *in vivo* limitations of our imaging approach in combination with ^{19}F MRI.

Chapter 5

Together with T cells, dendritic cells (DCs) also play significant role in the pathogenesis of type 1 diabetes. Therefore, we aimed to optimize the *in vitro* labeling of autoimmune DCs using novel perfluorocarbon-based fluorinated nanoparticles and studying their *in vivo* migratory profiles. After pre-labeling, dendritic cells were transferred in type 1 diabetes model using intraperitoneal injections. ^{19}F MRI was performed for the longitudinal tracking and quantification of labeled dendritic cells in the pancreatic region at various time-points. We investigated the dynamic profiles of ZPFCE-labeled DCs with and without pancreatic stress in a well-studied type 1 diabetes mouse model.

Chapter 6

In this chapter, we provided broad overview of labeling and *in vivo* monitoring of immune cells using noninvasive ^{19}F MRI. We discussed the advantages and limitations of ^{19}F MRI together with future perspective for the advancement of imaging methods.

CHAPTER 3

^{19}F MRI allows non-invasive longitudinal monitoring of host-microbe interactions in murine pulmonary aspergillosis*

Shweta Saini, Jennifer Poelmans, Hannelie Korf, James L Dooley, Sayuan Liang, Bella Manshian, Rein Verbeke, Stefaan J Soenen, Greetje Vande Velde, Ine Lentacker, Katrien Lagrou, Adrian Liston, Conny Gysemans, Stefaan C. De Smedt, Uwe Himmelreich.

*Under review in iScience Journal, Cell press, Elsevier

3.1 Abstract

The fungus *Aspergillus fumigatus* is ubiquitous in nature and the most common cause of invasive pulmonary aspergillosis (IPA) in patients with a compromised immune system. The development of IPA in patients under immunosuppressive treatment or in primary immunodeficiency patients demonstrates the importance of the host immune response in controlling aspergillosis. However, study of the host-microbe interaction has been hampered by a lack of tools for their non-invasive assessment. We developed a methodology to study the response of the host's immune system against IPA, using longitudinal *in vivo* monitoring by fluorine-19 magnetic resonance imaging (^{19}F MRI). We showed the advantage of a perfluorocarbon-based contrast agent for the *in vivo* labeling of macrophages and dendritic cells, permitting quantification of pulmonary inflammation in murine IPA models. Our findings reveal the potential of ^{19}F MRI for the dissection of rapid kinetics of innate immune response against IPA development, and the permissive niche generated through immunosuppression.

3.2 Introduction

Aspergillus fumigatus is an opportunistic, potentially life threatening fungus, which thrives mainly on organic substrates like decaying vegetation in the soil or food. While environmental exposure of humans to the airborne *A. fumigatus* conidia is common, host-pathogen interactions effectively eradicate conidia from the pulmonary region of healthy individuals (201, 232). The key determinant of infection is thought to be the innate immune response. *A. fumigatus* conidia in the alveolar space of lungs trigger pathogen recognizing receptors (PRRs), driving the first responders of the immune system (202). Key cellular mediators of immunity include resident alveolar macrophages, monocytes and dendritic cells for the engulfment of conidia, and neutrophils for the destruction of hyphae using neutrophil extracellular traps (208, 233, 234).

While healthy individuals effectively clear *A. fumigatus*, infection becomes life threatening in immunocompromised patients. With an increasing number of immunocompromised patients from organ transplantation or cancer treatment, IPA is rapidly growing as a medical problem (235). The acute inflammation in the lungs of IPA patients suggests an underlying malfunction, rather than absence, of essential host immune components as the causative factor (236). The

modus operandi for the clinical use of immunosuppressive drugs mainly includes cyclophosphamide (213) and hydrocortisone acetate (237, 238) administered intravenously to the patients. In previous studies, it was shown that the pathophysiology of IPA and the immune response against the fungal infection differs for each compounds (202, 239). Corticosteroids treatment impairs phagocyte function, including an abnormality in cellular migration and production of the inflammatory cytokines, while leaving neutrophils intact and functional (240–242). The phagocytic defect permits infection growth, which in turn drives a massive recruitment of neutrophils to the site of infection, resulting in intensive tissue damage. By contrast, cyclophosphamide induces neutropenia and depletes other circulating white blood cells, while leaving the local innate immune response relatively intact. Here the neutropenia is thought to be critical in permitting hyphal growth and further invasion in the tissue (204). A key limitation of these conclusions, however, is the reliance on invasive methods that are restricted to single time point measurements, such as immunohistochemistry (243). Knowledge of immune kinetics and longitudinal disease progression is currently lacking, but is essential for understanding the dynamics of these processes (204). *In vivo* imaging techniques are potentially able to assess the host response against the infection longitudinally in individual animals.

Different imaging techniques have been used in preclinical models to characterize IPA like computed tomography, positron emission tomography, bioluminescence imaging, single photon emission tomography, proton magnetic resonance imaging (^{1}H MRI) and fibred confocal fluorescence microscopy (215, 244–248). While these approaches fulfil the non-invasive and longitudinal criteria required, they lack specific information on inflammatory processes occurring in the host. In other disease models, *ex vivo* and *in vivo* cell labeling approaches use ^{1}H MRI contrast agents, to visualize immune cells for studying various inflammatory processes (249–252). However, ^{1}H MRI contrast agents such as (super)paramagnetic nanoparticles, generate unspecific signal voids, making it difficult to locate and quantify labeled cells *in vivo*. Fluorine contrast agents in combination with ^{19}F MRI may provide an alternative, with specific and quantifiable contrast (188, 189, 253).

^{19}F MRI is an emerging non-invasive tool, which can be applied both for imaging of *ex vivo* contrast agent-labeled cells after their transplantation and for *in vivo* labeling of cells after

systemic administration of fluorinated contrast agents (176, 254, 255). In this context, perfluoro-15-crown-5-ether fluorinated nanoparticles (PFCE-NPs) in combination with ^{19}F MRI, can generate highly specific MR contrast, due to the lack of background signal. Overlaying the ^{19}F MR image with a conventional ^{1}H MR image provides the necessary anatomical background (256).

Here, we developed an imaging platform allowing non-invasive and longitudinal quantification of the degree of pulmonary inflammation in IPA murine models. We showed the *in vivo* labeling of immune cells with newly developed zonyl perfluoro-15-crown-5-ether nanoparticles (ZPFCE-NPs) reveal underlying pathophysiological events during acute IPA using ^{19}F MRI.

3.3 Materials and Methods

3.3.1 Animals

For the *in vitro* labeling experiments, macrophages were isolated from the peritoneum of C57/BL6 female mice (8-9 week-old). Female OT-II mice (6-8-week-old) bearing the MHCII-restricted T cell receptor (TCR) for $OVA_{323–339}$ were bred in house. For *in vivo* experiments, 10-week-old male Balb/c mice (Janvier, Le Genest, France) were housed in KU Leuven animal housing facility with free access to food and water. All experiments were performed according to European, Belgian and KU Leuven ethical guidelines.

3.3.2 Synthesis of fluorinated Zonyl-PFCE nanoparticles

The synthesis of biochemically inert perfluoro-15-crown-5-ether (PFCE) nanoparticles consisting of a PFCE liquid core emulsified by a monolayer of phospholipids was performed as described previously (257). The fluorosurfactant Zonyl® FSP (Du Pont, Delaware, USA) was incorporated in the lipid shell of PFCE nanoparticles, obtaining nanoparticles with an average size of 280nm. For the *in vitro* and *in vivo* experiments, ZPFCE-NPs were coupled with either Cholestryl BODIPY® FLC12 or DiR fluorescent dye (both from Molecular Probes, Invitrogen, Merelbeke, Belgium).

3.3.3 In vitro labeling of macrophages using ZPFCE nanoparticles

For *in vitro* labeling, cells were incubated with ZPFCE-NPs at fluorine concentration of 0.5, 1 and 10mM for 1h at 37°C in 5% CO2 in ultra-low attachment plates (Corning Costar, Kennebunk, ME, USA). For positive selection of labeled macrophages, cells were analyzed for surface marker

expression after pre-incubation with the Fc receptor blocking antibody anti-CD16/CD32 (eBioscience, San Diego, CA, USA) and staining using anti-F4/80 and anti-CD11/b (eBioscience, San Diego, CA, USA) to perform quantitative flow cytometric analyses.

3.3.4 Toxicological assay on ZPFCE-NP labeled macrophages

Primary macrophages were labeled with different concentrations of ZPFCE-NPs. Surface staining with anti-F4/80 (eBiosciences) was performed to identify macrophages by microscopic analysis. Following exposure to nanoparticles, immune cells were stained to assess cell viability, cytoskeletal changes and oxidative stress. Data analysis was performed using a high-content InCell 2000 analyzer (GE Healthcare Life Sciences, Diegem, Belgium) as previously described (258).

3.3.5 Determination of cytokine secretion by ZPFCE-NP labeled macrophages

For cytokine measurement, ZPFCE-NP labeled macrophages were co-cultured in the presence or absence of 1µg/mL lipopolysaccharides (Sigma Aldrich, Overijse, Belgium) for 24h. Supernatants were collected and measurements of IL-10, IL-1beta and TNF-alpha were performed using a customized MSD V-PLEX mouse proinflammatory kit (Mesoscale, Maryland, USA). Readings were performed using a MESO QuickPlex SQ120 plate reader (Mesoscale, Maryland, USA).

3.3.6 In vitro adaptive immune test on ZPFCE labeled macrophages

Splenocytes from OTII transgenic mice were homogenized and negative selection of purified total CD4+ T cells was performed using a cocktail of antibodies for CD16/CD32, CD11b, CD11c, B220, MHC-II and CD8 markers. Contaminating, bead-bound cells were removed using sheep-anti-rat IgG paramagnetic beads, according to the manufacture's specifications (Dynabeads, Invitrogen Merelbeke, Belgium). Purity of samples (>95%) was routinely assessed by flow cytometry. Purified OTII-transgenic CD4+ T cells were co-incubated with ZPFCE-NP labeled macrophages in a 96 well plate together with variable doses of anti-TCR b5.1/b5.2 (OTII) peptide at concentrations of 0, 0.1, 1, 10µg/ml for 1-3 days at 37°C under 5% CO_2 for 1h. To prevent non-specific binding all surface stains were performed in the presence of anti-CD16/CD32. For macrophages, the antibodies F4/80-PerCPCy5.5, CD45-APC-eFluor780 and CD11b-eFluor450 were used. To stain T cells, CD44-FITC, TCRb5.1/5.2-PE, CD62L-Per CPCy5.5, CD69-PECy7 and

CD4-eFluor450 were used to assess effector, memory and naïve CD4+ T cell subsets using flow cytometry. All antibodies were purchased from eBioscience (San Diego, CA, USA).

3.3.7 Murine models of invasive pulmonary aspergillosis

To develop a non-neutropenic IPA model, mice were injected subcutaneously (s.c.) with 9mg hydrocortisone acetate per 25g body weight (Sigma-Aldrich, USP, Overijse, Belgium) one and three days before inoculation with *A. fumigatus* (HCA group, *n*=9). To induce neutropenia, 200mg kg^{-1} body weight cyclophosphamide (Sigma-Aldrich, USP, Overijse, Belgium) was injected intraperitoneally (i.p.) one and three days before inoculation with *A. fumigatus* (CY group, *n*=9). Infected immunocompetent mice (I-IC group, *n*=4) and non-infected immunocompetent mice (N-IC, *n*=3) were included as controls groups.

The $Fluc^+$ *A. fumigatus* strain 2/7/1 was generously provided by M. Brock (School of Life Sciences, University of Nottingham, UK). The strain was cultured and conidia were harvested using a previously described protocol (215). On day of infection (day 0), HCA and infected immunocompetent groups (I-IC group, *n*=4) were intranasally instilled with 1×10^6 spores. The CY group was inoculated with 5×10^5 spores based on the protocol described previously (215). ZPFCE-NPs were administered via tail vein 1h prior to MRI acquisition on day 0 and day 1 (Fig. 1A). On the day of inoculation (day 0), MRI experiments were performed on all mice groups 4h after the administration of spores. All murine groups were monitored for weight loss and posture changes starting from day 0 to detect onset of disease symptoms and to define the humane end-points.

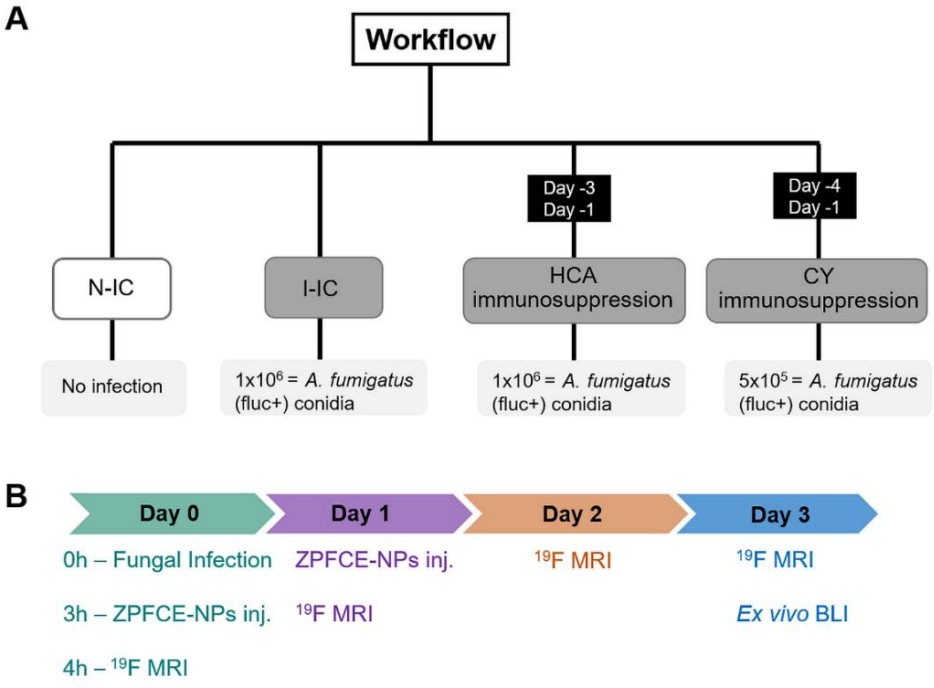

Fig. 1 Schematic representation of experimental workflow. (A) Immunosuppression regimes and fungal loading in different experimental groups. (B) Timeline for different *in vivo* imaging experiments in the murine models. (N-IC: Non-infected immunocompetent, I-IC: Infected-immunocompetent HCA: Hydrocortisone acetate, CY: Cyclophosphamide).

3.3.8 Longitudinal in vivo fluorine (^{19}F) magnetic resonance imaging

Animals were anesthetized for approximately 40 minutes by intraperitoneal (i.p.) injections of ketamine (45-60 mg kg^{-1}, Nimatek, Eurovet animal health, Bladel, The Netherlands) and Medetomidine (0.6-0.8 mg kg^{-1}, Domitor, The Orion Pharma, Espoo, Finland) solution. *In vivo* longitudinal follow-up of all murine groups was performed using ^{1}H and ^{19}F MRI on a 9.4T preclinical MRI scanner (Bruker Biospec 94/20, Ettlingen, Germany), (Fig. 1B). After the MR acquisition, injections of atipamezole (Antisedan, The Orion Pharma, Espoo, Finland) were administered i.p. to reverse the effects of anesthesia. Throughout the MR imaging experiments, body temperature and respiration rate of the animals were monitored and maintained to 37°C and 60-80 min^{-1}, respectively.

A purpose-built dual-tuned radio frequency surface coil was used to acquire fluorine and ^{1}H MR images. For all *in vivo* MRI experiments, 2D RARE (Rapid Acquisition with Relaxation Enhancement) MRI was performed using the following acquisition parameters: ^{1}H MRI, repetition time (TR) = 3500ms, rare factor = 8, flip angle = 180°, averages = 4, matrix size = 256×256, FOV = 40 mm × 40 mm, echo time (TE) = 6.12ms, spatial resolution = 0.156mm×0.156mm, slice thickness = 1mm, total scan time = 7 minutes. Frequency shift from 400 MHz to 376 MHz was performed on the same coil for ^{19}F MRI. For ^{19}F MRI, TR = 5388ms, rare factor = 32, flip angle = 180°, averages = 220, matrix size = 32×32, FOV = 40 mm × 40 mm, TE = 6.11ms, spatial resolution = 1.25mm×1.25mm, slice thickness = 2mm were used with total scan time = 23 minutes. A reference tube containing 30mM of ZPFCE-NPs embedded in agar was placed next to the abdomen of the animal during the MR acquisition to allow quantification of fluorine atoms. For both ^{1}H and ^{19}F MR images, data were acquired with the same localization (placement, orientation of slice packages).

3.3.9 Quantification of ^{19}F MR signal and data processing

Prior to the MR signal quantification, images were reconstructed using the Paravison 5.1 software (Bruker Biospin, Ettlingen, Germany). For post processing, MR images were exported to the MeVislab software version 2.6.1 (MeVis Medical Solutions AG, Bremen, Germany). Gaussian smoothing was applied to the ^{19}F MR images. Before masking the fluorine images, interval thresholding was performed by applying a value higher than the background noise (standard deviation of noise). Masked ^{19}F MR images were rescaled to the same matrix size as the ^{1}H MR images before superimposing them over each other. Motion corrections were applied to all scan for precise overlay of ^{1}H over ^{19}F images with the help of MeVislab software. To calculate the amount of fluorine atoms/voxel, the processed ^{19}F MR images were analyzed slice-wise using the Fiji software, version 1.49a (South Carolina, USA) by drawing the region of interests on the fluorine hot spots in the lungs and the lymph node regions, which were identified based on the anatomical ^{1}H MR images. For quantification, regions were compared with the reference tube that contained 30mM ZPFCE-NPs. Cumulative ^{1}H image scoring was performed on ^{1}H images of all murine groups from day 0 to day 3. Based on the visual observations, lung

lesions were identified and a scoring system was used to assign a value for the quantification of signal intensities corresponding to the disease development as described previously (259, 260).

3.3.10 Ex vivo bioluminescence imaging

On day 3, the animals were euthanized and the lungs were inflated with 0.5ml D-luciferin (7.5mg) (Promega, Leiden, The Netherlands) by inserting a 22-gauge catheter (Terumo, Heverlee, Belgium) into the trachea. The lungs were immediately placed into the flow chamber to perform *ex vivo* BLI acquisitions on the IVIS Spectrum imaging system (Perkin Elmer, Massachusetts, USA). Data were analyzed using Living Image® software version 4.5.5 (Perkin Elmer, Massachusetts, USA).

3.3.11 Differential white blood cell measurements

For the differential blood cell counting, mice were euthanized under deep terminal anesthesia and blood was withdrawn using a 25-gauge needle (Terumo, Heverlee, Belgium) from the left ventricles of the beating heart through cardiac puncturing. Total collected blood volume was 0.3 ml from each mouse. To prevent coagulation of blood, 30µl of tri-sodium citrate, 3.8% w/v (VWR, Belgium) was added to the blood collection tubes. Blood cell counts were performed on an ADVIA®2120i hemocytometer, version 5.4 (Siemens Healthcare, GmbH, Erlangen, Germany).

3.3.12 Colony-forming unit (CFU) measurements

After the *ex vivo* BLI acquisition, the right lung lobes were collected in 600µl PBS and homogenized to obtain suspensions of lung tissue. Lung homogenates were plated on Sabouraud agar, followed by an incubation period of 2-3 days at 30°C for manual counting of CFUs.

3.3.13 Flow cytometry and microscopy

Flow cytometry acquisitions were performed on a Gallios™ flow cytometer (Beckman Coulter, Brea, California, USA). For the data analyses, a FlowJo software, version 10.4.2 (FlowJo LLC, Ashland, Oregon, USA) was used. Microscopic images were acquired using a confocal microscope (Nikon, Tokyo, Japan) and analyzed using Fiji software, version 1.49a (South Carolina, USA).

3.3.14 Ex vivo optical imaging of lungs and cervical lymph nodes

Ex vivo fluorescence imaging was performed on the lungs and cervical lymph nodes (LN) of all animals using the IVIS Spectrum imaging system (Perkin Elmer Massachusetts, USA). For the acquisition of data, parameters used are as following: exposure time = 10sec, 740nm excitation and 800nm emission filters with medium binning. Data analysis was performed using the Living Image® software, version 4.5.5 (Perkin Elmer, Massachusetts, USA).

3.3.15 Histology and immunohistochemistry

Right lung lobes were fixed in 4% PFA and embedded in paraffin. For visualization of fungi, lungs were sectioned (5µm) and stained with Periodic acid-Schiff (PAS) agent as described (215). Brightfield images were acquired using ZEISS Axio Scan.Z1 Digital Slide Scanner (Carl Zeiss, Oberkochen, Germany). For immunoflurosence, left lung lobes were fresh frozen in OCT (optimum cutting temperature) formulation and cryosections (11µm) were fixed in 4% paraformaldehyde and stained according to manufacturer's protocol. For staining of the sections following monoclonal antibodies were used: GR1 (RB6-8C5, eBioscience), CD11b (M1/70, Biolegend), CD11c biotin (N418, eBioscience). For the staining of immune cells, the following detection antibodies were used: Donkey anti-Rat 488, Streptavidin 546, (all from Molecular Probes). Images were acquired using a EVOS FL Auto 2 microscope (Fisher Scientific, Merelbeke, Belgium).

3.3.16 Statistical analysis

For statistical analyses, One-way and Two-way ANOVA tests were performed together with Bonferroni multiple comparison test to compare the different animal groups using the GraphPad Prism software®, version 5.04 (La Jolla, CA, USA).

3.4 Results

3.4.1 Small-sized biocompatible ZPFCE-NPs showed efficient in vitro labeling of murine phagocytes

In order to monitor the immune responses *in vivo*, we sought to exploit the functional property of phagocytosis for immune cells labeling. ZPFCE-NPs label professional phagocytic cells due to

their small size (261). To validate the feasibility of this strategy, we used ZPFCE-NPs incorporated with Cholestryl BODIPY® FLC 12 green fluorescent dye. These nanoparticles did not show nanotoxicity in primary macrophages upon labeling with relatively high concentrations, affirming their suitability for *in vivo* applications (Fig. S1).

Macrophages, identified by their characteristic high surface expression of CD11b and F4/80, successfully phagocytosed ZPFCE-NPs in a dose-dependent manner (Fig. 2). ZPFCE-NP labeling of macrophages showed similar labeling efficiencies for particle concentrations of 1mM and 10mM (Fig. 2A).

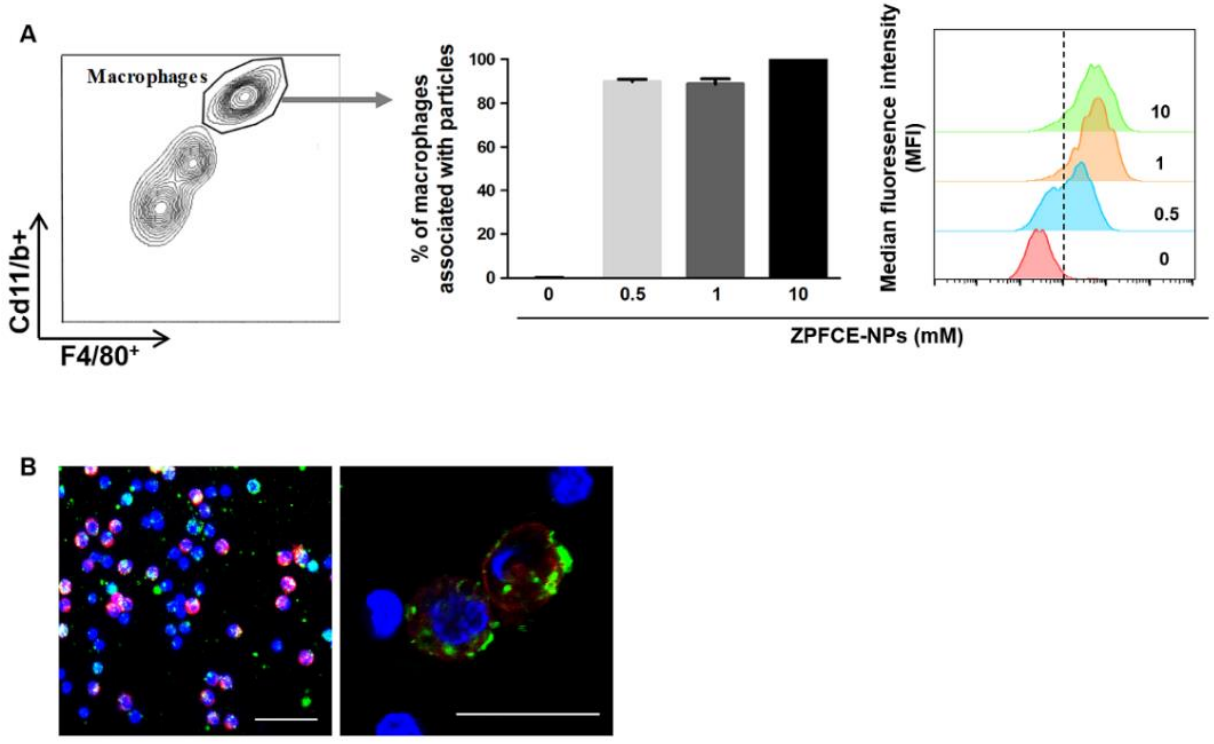

Fig. 2 ZPFCE-NPs allows labeling of macrophages. (A) Labeling of macrophages (positive cells for F4/80 and CD11b surface marker) with ZPFCE-NPs was measured in terms of percentage uptake at variable doses of particles. Median fluorescence intensities were measured from the gated ZPFCE-NP labeled macrophages for each dose (mean±SD). (B) Confocal image showing macrophages stained by F4/80 surface (red) with the ZPFCE-NPs (green), magnified representative images show intracellular uptake of ZPFCE-NPs. Scale bar is 20µm.

A key requirement for an *in vivo* labeling protocol is that the label does not interfere with the biological processes being measured. In order to investigate whether ZPFCE-NP labeling modulates macrophage function, we tested key innate and adaptive functions *in vitro*. Using cytokine secretion as a readout for innate functional activation of macrophages, we found no impact of ZPFCE-NPs on spontaneous or LPS-induced immune activation at a dose of 1mM, and only a weak enhancement of LPS-induced TNF-alpha production at 10mM (Fig. 3A).

For the adaptive immune system, we tested the biological effect of ZPFCE-NPs labeling on antigen-presenation by macrophages. C57BL/6 peritoneal macrophages were pre-labeled with ZPFCE-NPs and pulsed with OVA peptide (OVA323-339,) before the co-culture with OVA-reactive OT-II TCR transgenic CD4+ T cells. OT-II T cells showed efficient activation when primed with OVA-loaded macrophages, which was unaltered by the pre-loading with ZPFCE-NPs (Fig. 3B). Together, these results demonstrate that 1mM ZPFCE-NPs allow macrophage labeling without inducing biological alterations to either the innate or adaptive functions of macrophages.

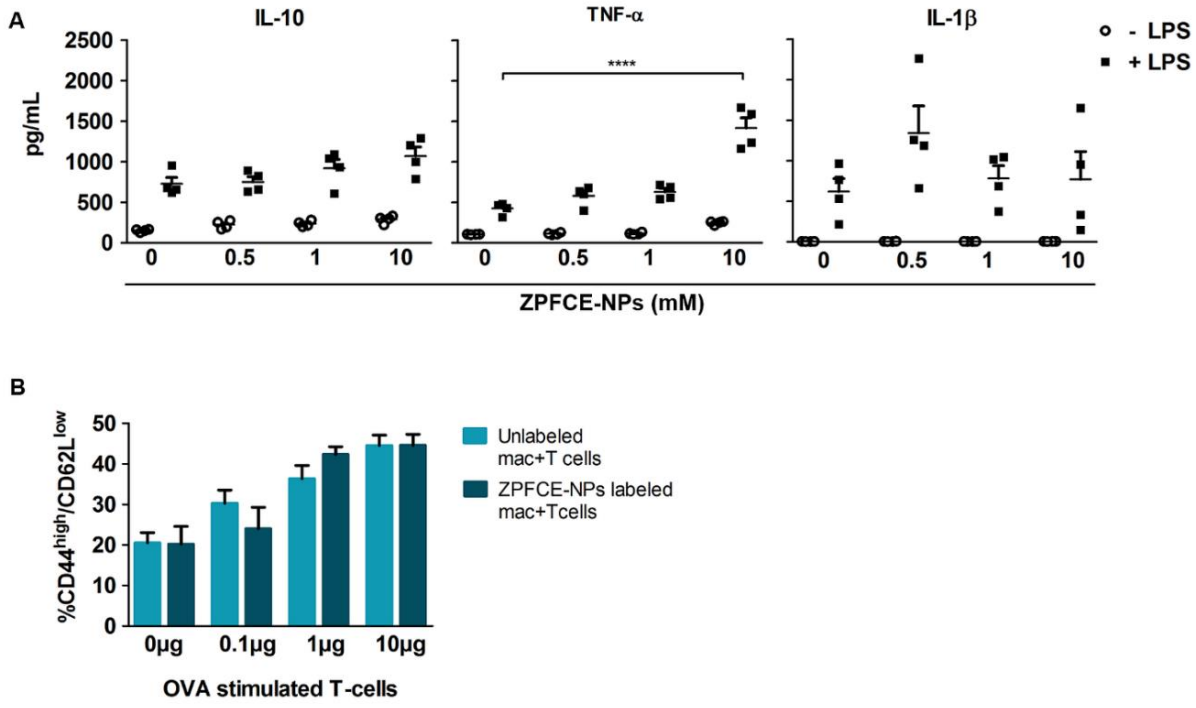

Fig. 3 ZPFCE-NPs allows labeling of murine macrophages without modulating their innate and adaptive immune function. (A) Cytokine measurements performed on supernatants from ZPFCE-labeled macrophages in the presence

and absence of LPS. Data represent; mean±SEM (n=5, ****p<0.0001). (B) C57BL/6 peritoneal macrophages were pre-loaded with ZPFCE-NPs and pulsed with OVA peptide ($OVA_{323-339}$) at different concentrations, before co-culture with OT-II TCR transgenic CD4+ T cells. After 3 days of co-culture, the cells were stained for lineage T cell markers in combination with T cell activation markers and analyzed by flow cytometry. The percentage of $CD44^{high}CD62L^{low}$ activated T cells across variable doses of the OT II peptide, for ZPFCE-NP-labeled and unlabeled macrophages (n=5, mean±SEM).

3.4.2 ^{19}F MR imaging allows in vivo visualization and quantification of immune cell recruitment in A. fumigatus infected lungs

Having validated ZPFCE-NPs as an efficient and biologically-neutral fluorinated nanoparticles for macrophages, we sought to assess the *in vivo* utility using IPA mouse models to apply our methodology as a proof-of-principle. To test the robustness of our immunomonitoring method, we used three models of pulmonary aspergillosis with immunocompetent and immunosuppressed mice, together with non-infected mice as control. Cyclophosphamide (CY) or hydrocortisone acetate (HCA) immunosuppressive drugs were used to induce neutropenia and phagocytic dysfunction in mice, respectively. Immunocompetent mice infected with *A. fumigatus* demonstrated a large and rapid influx of macrophages into the lung within 4 hours of infection (Fig. 4A, second row and 4B). Inflammation was quickly resolved, with a return to near-baseline macrophage levels by 24 hours (Fig. 4B).

By contrast, both forms of immunosuppression sharply reduced the immediate innate response to infection, with poor influx at 4 hours (Fig. 4A, third-fourth row and 4B). In both cases, this defect in the immediate response corrected with a more chronic inflammatory signal, with large macrophage influx out to at least three days post infection (Fig. 4B), consistent with a model where the defective immediate response allowed infection to become invasive and chronic. We observed and quantified a higher fluorine MRI signal intensity in the HCA mice as compared to the CY mice groups at the site of inflammation post pulmonary infection. No detectable fluorine signal was observed from the non-infected immunocompetent mice (N-IC).

Key differences were also observed between the immunosuppressed groups, with HCA treated mice, but not CY treated mice, resulting in a transient flux of macrophages into the cervical lymph nodes on day 1 post infection (Fig. 4C). This indicates that HCA allow macrophage mobilization but diverts recruitment into the draining lymph node rather than into the tissue.

In order to monitor progression of infection, we applied a cumulative scoring of ^{1}H MR images based on the lung signal intensity in all murine groups. This shows the pathophysiological changes occurring over time following infection from day of infection (day 0) until day 3 (Fig. S2A). We have observed high signal intensities in the CY group where infection was more profound compared to the HCA group (Fig. S2B). Together, these results both validate ^{19}F MRI as an *in vivo* monitoring tool for anti-microbe responses, and also indicate a critical window of response for the innate immune system against *A. fumigatus* invasive infection.

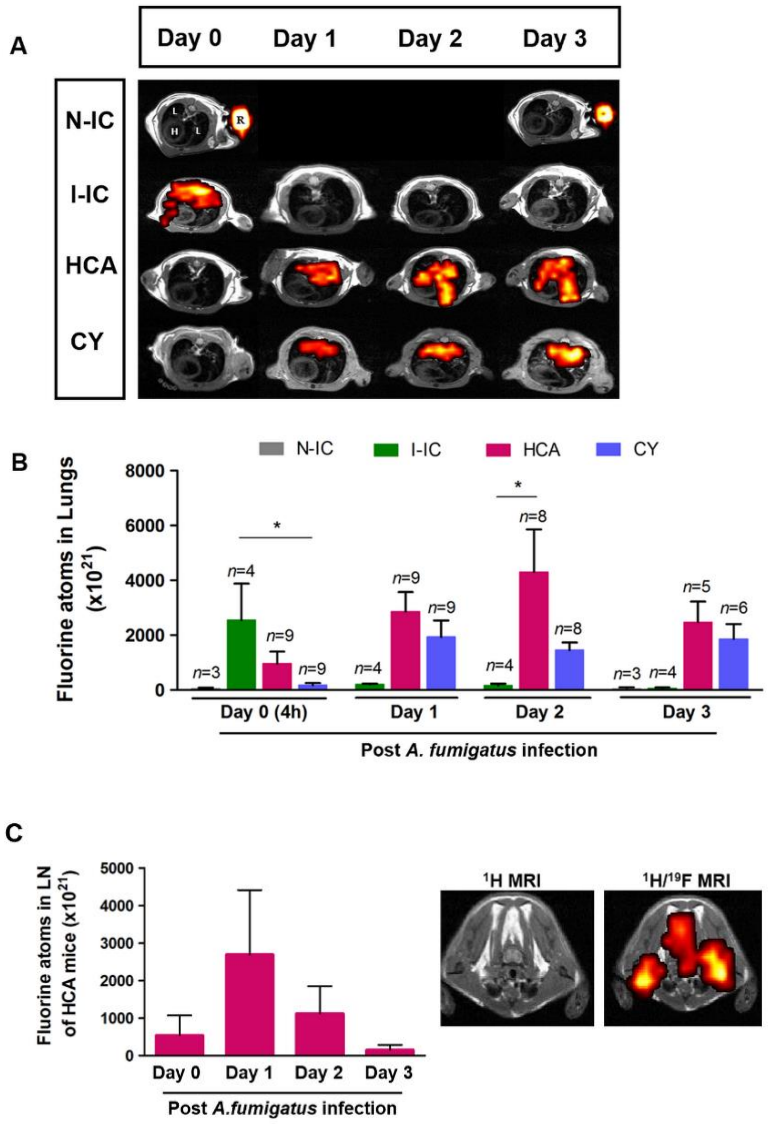

Fig. 4 ^{19}F MRI identifies the differential local immune response to infection by *A. fumigatus* in immunocompromised murine hosts. (A) ^{19}F MR images (fluorine signal was superimposed on anatomical ^{1}H MR images) were obtained

from hydrocortisone acetate (HCA), cyclophosphamide (CY) and infected-immunocompetent (I-IC) mice as well as non-infected control mice (N-IC) on day 0 (4h post infection). All mice received systemic injection of ZPFCE-NPs on day 0 (4h post infection) and day 1. All infected mice were imaged daily (^{1}H and ^{19}F MRI). The non-infected immunocompetent (N-IC) group was followed-up on day 0 and day 3. (B) Quantification of the ^{19}F MR signal from the lung region was performed for all groups by comparing, the signal intensity of the lung region with a reference (R in panel (A) top left image) containing 30mM ZPFCE-NPs. (C) ^{19}F MRI signal was observed from the lymph node region only for the mice from HCA group on day 1. Mean ^{19}F MR signal intensity was quantified with respect to the 30mM reference placed next to each animal. ^{19}F MRI signal in lymph nodes is indicated as hot spots overlaid over the anatomical ^{1}H MR image (right panel). Data showed as mean±SEM (n= 5, $*$ $p<0.05$).

3.4.3 Distinctive fungal burden depicted by BLI and CFU confirms infection

In order to affirm infection and viable pulmonary fungal load with inflammatory processes that we have monitored by ^{19}F MRI, we have examined the Fluc^{+} *A. fumigatus* infection three days after infection by using *ex vivo* BLI. After D-luciferin administration in the lungs, cyclophosphamide treated mice showed higher BLI signal intensity compared with the hydrocortisone treated mice (Fig. 5A).

No detectable bioluminescence signal was observed from the lungs the two control groups, infected immunocompetent and non-infected mice. Quantification of BLI signal also showed significantly high fungal infection in the cyclophosphamide treated group compared to the hydrocortisone treated group and infected-immunocompetent group (Fig. 5B). This indicates strong invasion of fungi in the lungs of CY group due to lack of an efficient immune response compared to the HCA group where, the immune response prevents the growth of *A. fumigatus*.

For the quantification of pulmonary fungal load, we performed CFU counting on the cultured lung homogenates from all mice groups. We observed a significant increase in the *A. fumigatus* burden in the lungs of the CY group when compared to the HCA on day 3 (Fig. 5C). In contrast, N-IC and I-IC groups did not show any fungal growth. These results together with ^{19}F MRI suggest the early immune activation in infected mice as a critical aspect for the control of potentially invasive *A. fumigatus* progression.

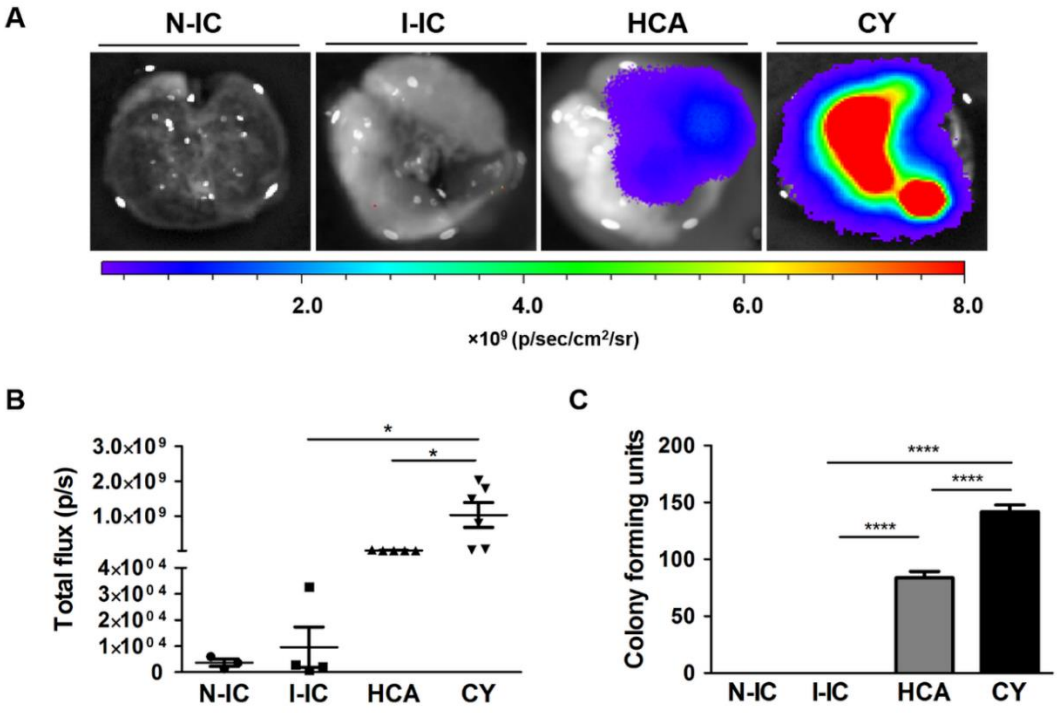

Fig. 5 Visualization and quantification of fungal load reveals the impaired immune response against *A. fumigatus* invasion in immunocompromised mice. (A) *Ex vivo* bioluminescent imaging (BLI) was performed to visualize firefly luciferase (Fluc) expressing *A. fumigatus* in the lungs three days after the infection. After the end-point ^{19}F MRI experiment, animals were sacrificed and D-luciferin was administered into the excised lungs of murine groups of mice. Lungs were imaged immediately after D-luciferin administration. The scale bar represents BLI signal intensity in photons flux/second. The color-coded BLI images are overlaid onto the photographic images of lungs. Intensity thresholds for all BLI images were kept the same. (B) BLI signal intensity from all murine groups was measured as total flux after assigning identical regions of interest on the BLI images of lungs. (C) Lungs were isolated three days after infection from all mice groups. Colony-forming units (CFU) were manually counted from lung homogenates, 24h after incubation at 37°C. No fungi were observed in the two control groups (N-IC and I-IC). Data is represented as mean±SEM (*P < 0.05, ****P<0.0001). HCA *n*=5, CY *n*=6, I-IC *n*=4, N-IC *n*=3.

3.4.4 Validation of ZPFCE-NP-labeled immune cell recruitment in the lungs and lymph nodes by histology and immunofluorescence imaging

To validate our imaging results, we performed PAS staining and immunofluorescence after sacrificing the animals three days after infection. Similar to ^{19}F MRI, we observed high pulmonary inflammation in the lung tissue of HCA group upon *A. fumigatus* challenge with minimal fungal invasion. In contrast, the CY group, showed as expected fungal growth and hyphal growth formation with invasion in nearby tissues and no visible inflammation (Fig. 6A). The two control

N-IC and I-IC mice groups showed normal lung tissue morphology with no fungal infection on day 3, validating the ^{19}F MRI findings.

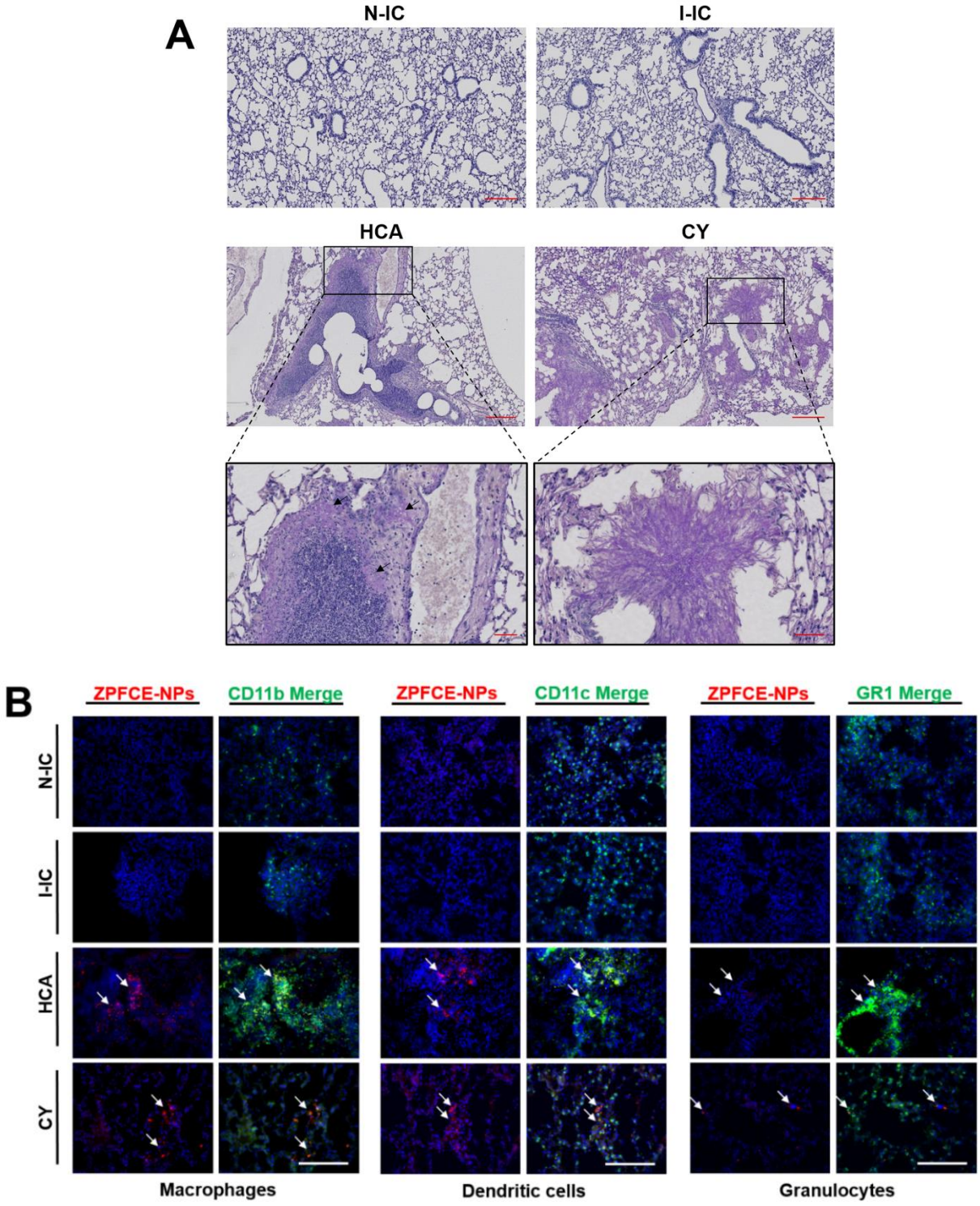

Fig. 6 Histological imaging elucidates diverse infection and inflammation patterns in immunocompromised groups. (A) Representative light microscopy of PAS-stained images showing histopathology from the PFA fixed lung sections of

different mice groups on day 3 post infection. Excessive immune cell infiltration near the bronchi and bronchiole upon pulmonary *A. fumigatus* infection in HCA mice showing profound inflammation-induced tissue destruction. Mild fungal infection observed in HCA mice (black arrows, HCA magnified image). Fungal dissemination shown in the CY mice resulted in compression of lung tissue with massive hyphal growth (magnified CY image). Scale bar images 200µm for (first-second row) and 50µm for magnified images (third row). (B) Immunofluorescence microscopy performed on fresh-frozen lung tissues showing the ZPFCE-NP labeled macrophages (anti CD11b) and dendritic cells (anti CD11c) recruited to the bronchioles (white arrows) in the lungs of HCA and CY mice. Granulocytes (anti GR1) were also found to be accumulated (white arrows) in high numbers in the HCA group compared to other groups. Scale bar is 100µm and staining represented as Blue=DAPI, Red=ZPFCE-NPs.

Immunofluorescence images also showed the presence of stringent inflammation resulting in higher influx of ZPFCE-NP labeled macrophages and dendritic cells in the lungs of HCA group in contrast to CY group (Fig. 6B, third-fourth row). Additionally, elevated recruitment of granulocytes was observed near the airways of HCA group compared to other groups. The N-IC and I-IC groups showed no visible inflammation or infection similar to ^{19}F MRI (Fig. 6B, first-second row). We also noticed differences in white blood cell counts, analyzed individually from the peripheral blood of different groups on day 3, indicating severe inflammation in HCA group reflected by an increase in the amount of neutrophils and lymphocytes in the blood contrast to the CY group (Fig. S3).

The non-infected model showed similar levels of neutrophils and lymphocytes as the I-IC model where immune cells were in the normal range. Notably, the cervical lymph nodes of HCA group showed high ZPFCE-NPs accumulation (Fig. S4). ZPFCE-NPs were also visualized in the OCT embedded lungs on day 3 by *ex vivo* fluorescence imaging, illustrating high fluorescent signal observed only in HCA group both in the lungs and in cervical lymph nodes (Fig. S5). Briefly, these results strongly support the ^{19}F MRI findings, demonstrating the feasibility of our established methodology for non-invasive monitoring of infection.

3.5 Discussion

With the increased amount of immunocompromised patients, it becomes more important to diagnose and follow up invasive pulmonary aspergillosis. Among the profound number of IPA clinical cases, 90% are caused by *A. fumigatus* (262, 263). For a better understanding of aspergillosis and for testing of novel antifungal compounds, preclinical animal models are essential. While methods for monitoring the dynamics of the immune cells upon *A.fumigatus* infection have been developed recently (204), these studies were not performed for longitudinal *in vivo* follow up to assess the interaction with the host's immune system non-invasively. Here, we have developed an approach that allows the non-invasive, dynamic monitoring of both, inflammatory processes and the infection in three animal models of IPA.

Several cell labeling approaches have been established to non-invasively visualize the mechanisms of immune reactions involved in various diseases by tracking the loci of inflammatory immune cells using ^{19}F MRI (185, 187, 188, 193). In this study, we focused on the quantification and localization of inflammation in IPA murine models of immune impairments induced by clinically used immunosuppressive drugs (243, 264, 265). PFCs have been used and tested as blood substitutes and thus proven to be safe in humans (154, 266). Here, we synthesized ZPFCE-NPs and studied their potential for the labeling of phagocytic immune cells. It has been shown that labeling with PFCE particles of different sizes could potentially modulate the immune function of dendritic cells (267). In this study, we showed the biological compatibility of ZPFCE-NPs for *in vivo* studies, where labeled macrophages retained their antigen processing and T cell activation capacity.

In our *in vivo* study, we have used ^{19}F MRI to quantify inflammation noninvasively and longitudinally after systemic injections of ZPFCE-NPs. The ^{19}F MRI signal detected in inflamed areas corresponds to the infiltration of labeled phagocytic cells in the region of interest (187, 190). We observed high ^{19}F MRI signal intensities in the lungs of the infected immunocompetent (I-IC) mice already 4h after the fungal infection, which has completely cleared after 24 hours, confirming the expected eradication of *A. fumigatus* conidia by the immune system. In the hydrocortisone (HCA) treated mice, the exacerbated intrusive recruitment of immune cells resulted not only the labeling of tissue-resident macrophages but also dendritic cells (186). Inflammation was found to be less pronounced in the cyclophosphamide (CY) treated mice, with increased fungal invasion in the

lungs. We did not observe any detectable fluorine signal in the lungs from the non-infected immunocompetent (N-IC) mice that have received ZPFCE-NPs, indicating absence of any inflammation in the lungs. Only in HCA mice, elevated accumulation of ZPFCE-NPs was observed in the nearby cervical lymph nodes to 3 days after infection as shown in the ^{19}F MR images.

In addition to ^{19}F MRI, *in vivo* ^{1}H imaging in these mouse models was able to document the lesion development occurring in the lungs upon fungal conidia challenge. As shown by our quantitative image analysis, we observed high lung lesion formation in CY mice two and three days after infection, which is consistent with profound fungal hyphal growth and invasion in lungs as reported before (215). ^{1}H MRI indicated only weak lesion formation in the infected HCA treated and I-IC groups. These results endorse the fact that the administration of cyclophosphamide as a frequently used immunosuppressive drug can lead to lethal IPA with mild initial inflammation in the lungs as indicated by ^{19}F MRI.

On the contrary hydrocortisone-based immunosuppression leads to less lesion formation by *A. fumigatus* but triggers acute inflammation leading to potentially lethal tissue destruction (204). The functional immune system of the infected-immunocompetent mice resulted in the rapid initial immune reaction and complete clearance of the fungi as shown in the ^{1}H MR images and also confirmed by histology. By using ^{19}F MRI, we were able to monitor the intricate dynamic profile of the host-pathogen interaction in pulmonary *A. fumigatus* infection *in vivo.* We documented the differences between immunocompetent hosts and animals treated with two different immunosuppressive compounds.

Collectively, we showed the potential of ^{19}F MRI and perfluorocarbon-based ZPFCE-NPs by successful tracking and quantifying the fluorine signal generated by innate immune cells, macrophages and dendritic cells in the lungs corresponding to the intensity of local inflammation. By being able to monitor both, the infection and immune reaction in live animals over time, it is possible to make treatment decisions rapidly and almost in real time. In the future, this will help in testing novel antifungal drugs or new approaches to influence the immune system providing a platform for studying immune cell therapies in patients together with the emerging ^{19}F MR imaging platform (155, 198, 268, 269).

3.6 Supplementary figures

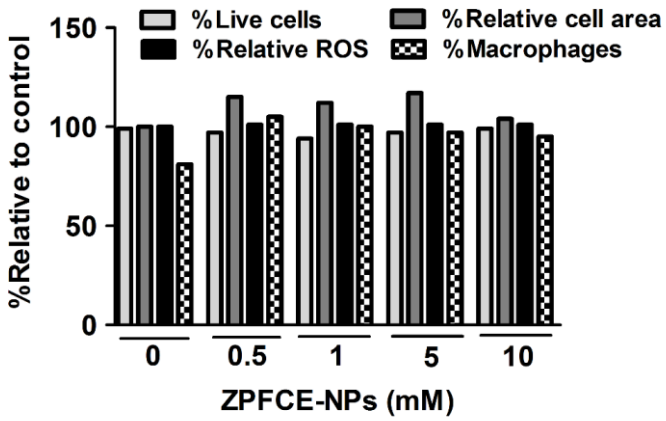

Fig. S1 ZPFCE-NP labeling did not show any biological alteration of macrophages. High-content InCell imaging was performed to evaluate potential cellular toxicity for macrophages upon ZPFCE-NP labeling. Histograms revealed the relative level of cell viability, cell area, formation of mitochondrial reactive oxygen species (ROS) and percentage of macrophages in the total population of immune cells exposed to 0, 0.5, 1, 5, and 10mM of ZPFCE-NPs. Data are represented as mean± SEM of the untreated control values. No statistically significant differences were detected.

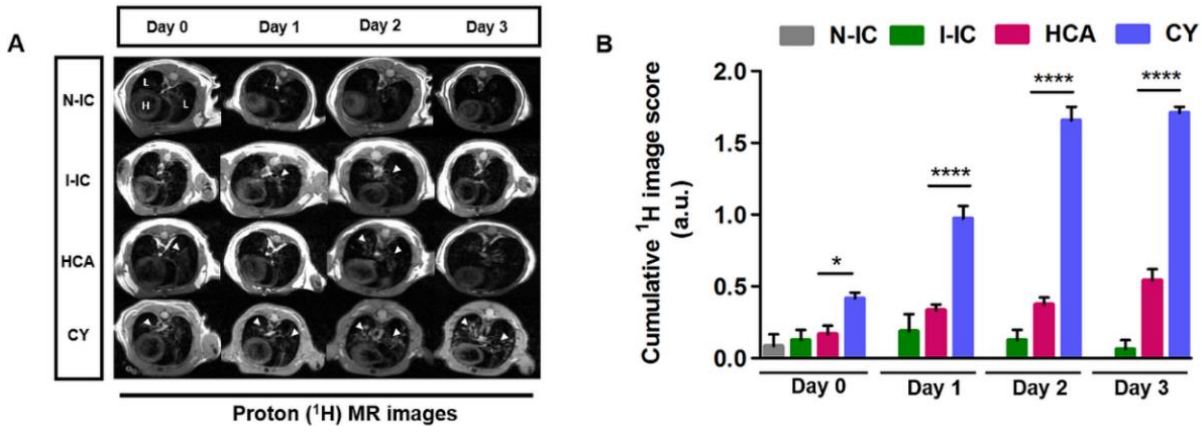

Fig. S2 *In vivo* quantification of anatomical changes using ^{1}H MR imaging confirms infection (IPA) and shows lesion development in immunocompromised mice. (A) ^{1}H MR images were acquired before ^{19}F MRI acquisition using a dual-tuned MR coil. ^{1}H MRI images were acquired daily from the day of infection for three days. Lesions caused by

A. fumigatus infection are seen as hyperintense (bright) regions (arrow). (B) Quantitative estimation of lung lesion development was performed based on the image signal intensities by applying cumulative image scoring method. (N-IC: Non-infected immunocompetent group, *n*=3; I-IC: Infected-immunocompetent group, *n*=4; HCA: Hydrocortisone acetate treated group, *n*=5; CY: Cyclophosphamide treated group, *n*=6). Data represented as mean±SEM. (* p<0.05, ****P<0.0001).

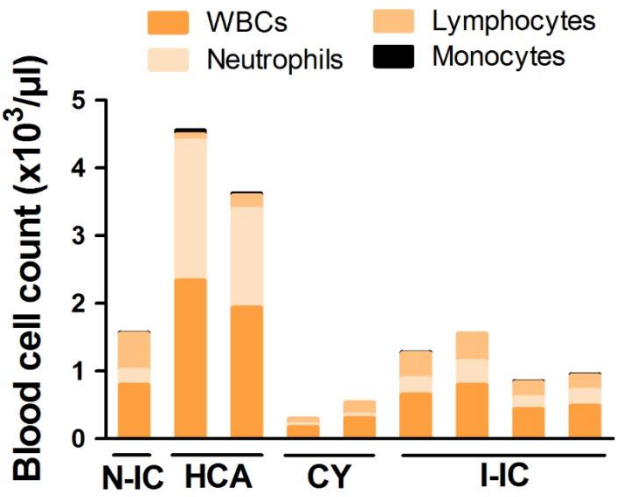

Fig. S3 Differential blood immune cell counting depicts patrolling immune cells in all murine groups. Samples from peripheral blood pool was analyzed for individual mice after cardiac puncturing. Blood samples were collected from different groups on the experimental end-point at day 3. Numbers of white blood cells (WBCs), neutrophils, lymphocytes and monocytes were measured and represented for individual animal.

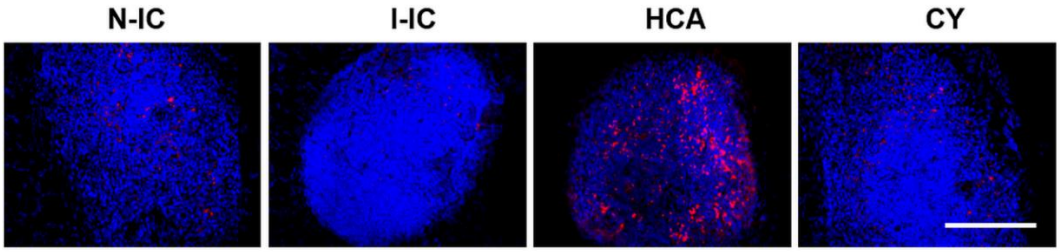

Fig. S4 Visualization of ZPFCE-NPs in cervical lymph nodes confirms *in vivo* ^{19}F MRI assessment for all mice groups. Fluorescent microscopy was performed on cryo-sectioned cervical lymph nodes where high accumulation of ZPFCE-NPs in the lymph nodes was shown in HCA group compared to other groups after animals have been sacrificed on day 3, after infection. Scale bar 100µm. Stainings: Blue=DAPI, Red=ZPFCE-NPs.

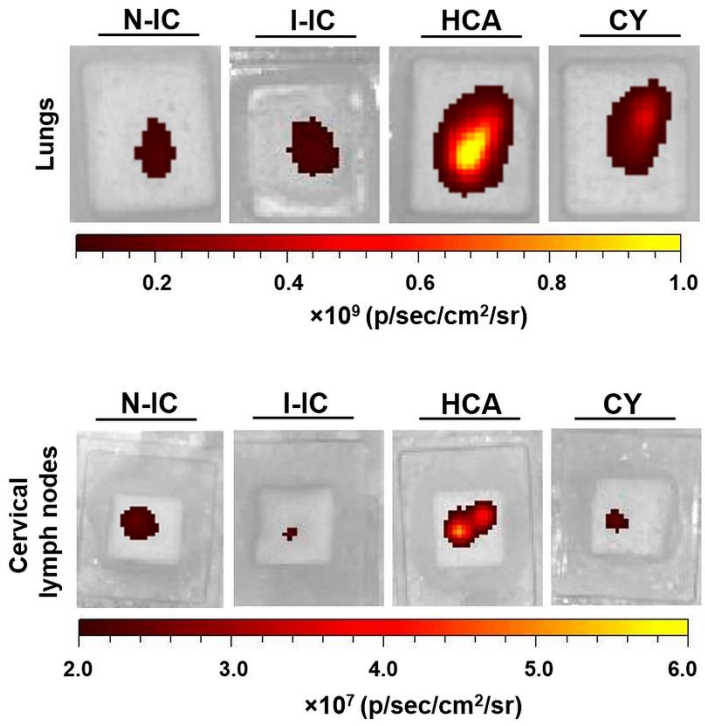

Fig. S5 *Ex vivo* fluorescence imaging of lungs and cervical lymph nodes using IVIS Spectrum system confirms ^{19}F MRI. Fluorescence images on the cryopreserved OCT-embedded lungs and cervical lymph nodes from all groups of mice were performed after the experimental end-point, three days post-infection. The scale bar represents fluorescence signal intensity. High signal intensities were detected in the lungs and lymph nodes of HCA-treated mice, confirming accumulation of ZPFCE-NP-labeled immune cells.

CHAPTER 4

Challenges for labeling and longitudinal tracking of adoptively transferred autoreactive T lymphocytes in an experimental type 1 diabetes model*

Shweta Saini, Hannelie Korf, Sayuan Liang, Rein Verbeke, Bella Manshian, Koen Raemdonck, Ine Lentacker, Conny Gysemans, Stefaan C. De Smedt, Uwe Himmelreich.

*Magnetic Resonance Materials in Physics, Biology and Medicine (2019),1352-8661

4.1 Abstract

Tracking the autoreactive T cell migration in the pancreatic region after labeling with fluorinated nanoparticles(1,2-dioleoyl-*sn*-glycero-3-phosphoethanolamine-N-[3-(2-pyridyldithio)propionate]-perfluoro-15-crown-5-ether nanoparticles, (PDP-PFCE NPs) in a diabetic murine model using ^{19}F MRI. Synthesis of novel PDP-PFCE fluorine nanoparticles was performed for *in vitro* labeling of T cells. Labeling conditions were optimized using different PDP-PFCE NPs concentrations. For *in vivo* ^{19}F MRI, mice were longitudinally followed after adoptive transfer of activated autoreactive labeled T cells in NOD.SCID mice. Established MR protocols were used for challenging T cell labeling in order to track inflammation in a model of diabetes after successful labeling of CD4+ and CD8+ T cells with PDP-PFCE NPs. However, T cells were difficult to be detected *in vivo* after their engraftment in animals. We showed successful *in vitro* labeling of T cells using novel fluorinated liposomal nanoparticles. However, insufficient and slow accumulation of labeled T cells and subsequent T cell proliferation in the pancreatic region remains as limitations of *in vivo* cell imaging by ^{19}F MRI.

4.2 Introduction

Autoimmune type 1 diabetes (T1D) results from a decline in insulin-producing pancreatic β-cells, resulting in hyperglycemia when β-cells are selectively destroyed by the autoimmune repertoire. The diagnosis of T1D mainly includes serological fasting blood glucose measurements and identification of genetic markers. Over the past years, some progress has been made for the *in vivo* visualization of pancreatic β-cells in both pre-clinical and clinical settings (270–274). In T1D, autoreactive T cells are the main culprits responsible for inflammation and the depletion of insulin producing pancreatic β-cells. However, the interplay between immune cells and β-cells remains poorly understood and was only visualized by invasive imaging techniques (230, 231). Non-invasive assessment of the onset of inflammation and autoimmunity is currently unavailable, but would improve monitoring of the disease and possible treatment. Several studies have been conducted to understand the role of T cells, where both CD4+ and CD8+ T cells are found to be crucial in the induction of T1D (275, 276). The ability to visualize immune cells after *in vitro* labeling with potential contrast agent could provide a powerful tool in order to understand the evolution of the disease and establish testing of novel therapeutic approaches. The potential value of non-

invasive imaging in elucidating underlying inflammatory processes includes monitoring the dynamics of cellular interactions and disease progression (254).

In this regard, *in vivo* cell imaging methods have gained momentum over the last decade (277, 278). Hereby, magnetic resonance imaging (MRI) is one of the most powerful *in vivo* imaging tools due to its high resolution and soft tissues contrast. For the visualization of specific cell types, MRI contrast agents are needed that are (a) highly specific to the targeted cell type, (b) are sensitive, (c) generate unambiguous contrast, (d) stably attach to/are incorporated by the cells, (e) not affecting cell biology and (f) generating longitudinal contrast changes (176).

Until now, most imaging applications for the *in vivo* visualization of inflammatory processes and cells of the immune system have mainly focused on models with high numbers of immune cell infiltrating at the site of injury or disease. The utilization of sensitive superparamagnetic iron oxide (SPIO) particles as contrast agents was often hampered by unfavorable background contrast, unspecific contrast origin and the inability to accurately quantify the extent of inflammation (279). Nowadays, fluorine (^{19}F) MRI has gained increased popularity also for the visualization of inflammatory processes where the MR signal from the ^{19}F atoms can be directly quantified (185, 188, 193, 280). As a potential contrast agent for ^{19}F MRI, perfluoro-15-crown-5-ether nanoparticles (PFCE-NPs) are promising due to the large number of equivalent fluorine atoms per molecule (266, 281). It has been shown that, when intravenously injected, PFCE-NPs do not extravasate but are phagocytosed mainly by macrophages allowing the measurement of immune cell infiltration corresponding to the inflammation in disease models.

On the other hand, it has been extremely challenging to label non-phagocytic immune cells like T cells for their *in vivo* follow-up after their engraftment in a suitable T1D model (282, 283). To overcome such challenges, chemical methods like the use of transfection agents are successfully applied to label non-phagocytic cells like T cells and visualize them in a murine model of diabetes (196). However, it has been reported that transfection agents may induce cellular toxicity or immune activation, potentially disturbing the normal physiological function of T cells (284). In order to achieve a sufficient cellular fluorine concentration for generating detectable ^{19}F MR signal without using transfection agents, we applied a lipid modification of PFCE NPs with PDP (1,2-

dioleoyl-*sn*-glycero-3-phosphoethanolamine-N-[3-(2-pyridyldithio)propionate]) (PDP-PFCE NPs), facilitating the interaction of T cell membrane with the nanoparticles (285).

In this study, we aimed to visualize islet antigen-specific (NOD-derived BDC2.5), autoreactive T cells labeled with novel PDP-PFCE NPs after adoptive transfer in NOD.SCID mice using ^{19}F MR imaging.

4.3 Materials and Methods

4.3.1 Animals

BDC2.5 T cell receptor (TCR)-Tg NOD mice aged 6-8 weeks (n=8) and NOD.SCID mice aged 5-6 weeks (n=13) were obtained from the breeding facility of Clinical and Experimental Endocrinology (KU Leuven, Leuven, Belgium). All animals were housed in micro-isolator IVC cages, fed with standard chow diet, and received tap water *ad libitum*. All *in vivo* experiments were approved by the institutional Animal Care and ethical Committee.

4.3.2 Synthesis of PFCE and PDP-PFCE nanoparticles

PFCE NPs were prepared, as described previously (256). Further, 40.2 wt % DOPE (1,2-dioleoyl-sn-glycero-3-phosphoethanolamine), 50 wt% PE-PDP (1,2-dioleoyl-sn-glycero-3-phosphoethanolamine-N-[3-(2-pyridyldithio)propionate]), and 9.8 wt% cholesterol (Avanti Polar Lipids, Alabaster, USA) all dissolved in chloroform was mixed with PFCE-NPs to synthesize PDP-PFCE NPs.

For flow cytometry, anionic PDP-PFCE NPs were incorporated with 2.5 wt% of the lipophilic DiR fluorescent dye (Thermo Scientific, Cramlington, UK). After evaporation of chloroform, the lipid film was hydrated in a 1:2:7 of glycerol, propanediol (Thermo Scientific) and MiliQ water to obtain total lipid concentration of 1.4×10^{-3} mmol ml^{-1}.

4.3.3 Isolation and activation of splenic T lymphocytes

Splenocytes obtained from BDC2.5 TCR-Tg NOD mice were maintained in RPMI 1640 medium (Invitrogen, Merelbeke, Belgium) supplemented with Glutamax (Gibco, Germany), 10% FCS, 10mM HEPES, 1mM glutamine, 1mM Na-pyruvate and 50µM 2-ME (Invitrogen, Merelbeke,

Belgium). After the lysis of red blood cells using NH_4Cl at room temperature, T cells were resuspended at 10^6 cells/mL. For T cell activation, splenocytes were pulsed with BDC2.5 mimotope (AnaSpec, Fremont, California, USA) at a concentration of 0.1µg/mL and incubated at 37°C for 72h as described (286). Purity of T cells was assessed ~90-95% for individual experiments using flow cytometry.

4.3.4 In vitro labeling of splenic-T cells with PDP-PFCE nanoparticles

After 72h of activation, T cells were washed with serum-free media and co-incubated with DiR-coupled fluorescent PDP-PFCE nanoparticles for 3h at 37°C. For flow cytometry, labeled T cells were washed for the removal of free nanoparticles with FACS buffer (Phosphate Buffer Saline (PBS) with 0.1 % BSA (Invitrogen, Merelbeke, Belgium) and 2mM EDTA (Merck, Darmstadt, Germany)). Pre-incubation with Fc receptor blocking antibody and cell surface staining was performed using an antibody mix of anti-CD4-FITC, anti-CD8-efluor450 and CD11/b-PE. Dead cells were excluded from each analysis by using Live/Dead yellow dye (Invitrogen, Merelbeke, Belgium).

4.3.5 Imaging of PDP-PFCE NP labeled T cells in phantoms and in vivo using ^{19}F MRI

Splenic T cells were labeled with PDP-PFCE NPs (total fluorine concentration: 20mM) and embedded in centrifugation tubes (Eppendorf, Rotselaar, Belgium) containing 2% agar (Merck, Darmstadt, Germany) and 5×10^5, 1×10^6, 2.5×10^6 or 5×10^6 cells (n=3), respectively. To mimic the *in vivo* environment, the same amount of labeled T cells suspended in 100µl sterile PBS were subcutaneously engrafted in mice before acquiring ^{19}F MR images. ^{19}F MRI was performed within 30 to 60 minutes following cell engraftment.

4.3.6 ^{19}F MR imaging of labeled T cells

All ^{19}F /^{1}H MR images were acquired on a preclinical 9.4T Bruker Biospec MR scanner (Bruker Biospec 94/20, Ettlingen, Germany). MR imaging was performed with a purpose-built dual tuned surface coil for ^{1}H (proton) and ^{19}F (fluorine) MR using the same orientation and placement of slice packages. For the monitoring of T cells, a first recipient group of NOD.SCID mice (*n*=5) received 1×10^6 and a second recipient group of NOD.SCID mice (*n*=5) received 5×10^6 BDC2.5-mimotope loaded PDP-PFCE labeled T cells *via* intravenous injections, (Fig. 1).

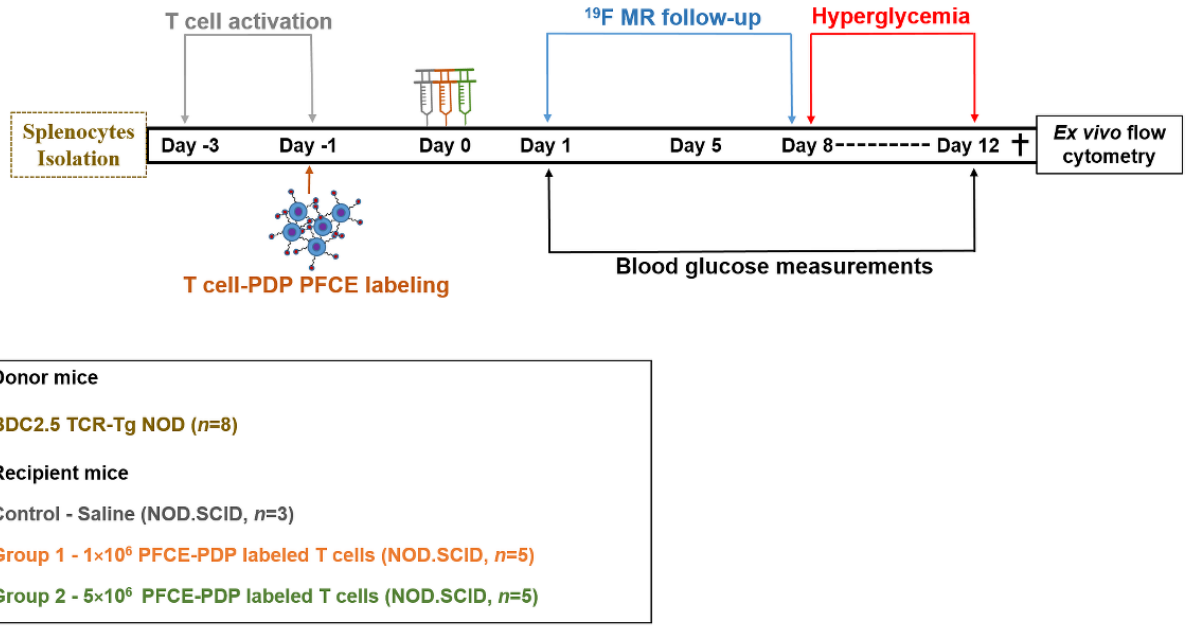

Fig. 1 Experimental timeline for the *in vitro* labeling and *in vivo* ^{19}F MR imaging after adoptive transfer of T cells in a T1D mouse model.

The control group received saline. For the T1D model, MR images were acquired in coronal orientation. For all acquisitions, a RARE (Rapid Acquisition with Relaxation Enhancement) MR sequence was used with the following parameters: Anatomical images were acquired with TE = 6.121ms, RARE factor = 8, flip angle = 180°, number of averages = 4, matrix size = 256×256, FOV = 40×40 mm, TR = 3500ms, spatial resolution = 0.156mm×0.156mm, slice thickness 1mm, total scan time= 5 minutes. Frequency shift from 400 MHz to 376 MHz was performed on the same coil for ^{19}F MRI. Fluorine images were acquired with TE = 6.11ms, flip angle = 180°, number of averages = 256, matrix size = 32×32, FOV = 40×40 mm, RARE factor =32, TR = 4500ms, spatial resolution = 1.25mm×1.25mm, slice thickness = 2mm, total scan time = 19 minutes.

For phantom experiments, anatomical images with TE = 6.121ms, RARE factor = 8, flip angle = 180°, TR = 3500ms, spatial resolution= 0.175mm×0.175mm, slice thickness 1mm were acquired. Parameters used for fluorine images were: TE = 6.11, rare factor=32, TR = 4500ms, spatial resolution = 1.406mm×1.406mm, slice thickness = 2mm.

4.3.7 In vivo estimation of fluorine concentrations in various organs

For the data processing, ^{1}H MR images were overlaid on the ^{19}F MR images using MeVislab software version 2.6.1 (MeVis Medical Solutions AG, Bremen, Germany). A reference tube with known number of ^{19}F atoms was places next to the liver of all animals. With the help of Gaussian smoothing and interval thresholding, ^{19}F MR images were masked as described previously (256). The regions of interest from ^{19}F MR images were manually delineated to obtain mean signal intensities relative to the reference for the quantification of fluorine atoms.

4.3.8 Ex vivo validation

For the T1D model, pancreases were isolated and prepared for flow cytometry from all NOD.SCID mice groups on day 9, after *in vivo* transfer of activated labeled T cell, as described previously (286). Briefly, pancreatic tissue was finely minced and suspended in RPMI complete medium containing 1mg/mL collagenase VIII and 0.02mg mL^{-1} DNAase I (Merck, Darmstadt, Germany) for tissue digestion. Single cell suspensions were obtained from homogenized tissues and strained using a 70µm nylon strainer (both from Miltenyi Biotec, Leiden, The Netherlands). Cells were surface-stained for flow cytometry using CD4+ and CD8+ T cell antibodies, for the identification of PDP-PFCE NPs labeled-T cells.

4.3.9 Flow cytometry and confocal microscopy

All antibodies used for flow cytometry were purchased from eBioscience (San Diego, California, USA). Flow cytometry was performed on a Gallios flow cytometer (Beckman Coulter, Analis, Suarlèe, Belgium), and data analyses was executed on FlowJo software®, (version 10.4.2, FlowJo LLC, Ashland, Oregon, USA). Confocal microscopy was performed on a Nikon Eclipse A1R microscope (Nikon, Tokyo, Japan).

4.3.10 ^{19}F Nuclear Magnetic Resonance (NMR) spectroscopy of cell suspensions

In order to assess the amount of fluorine label per cell, either 2.5×10^{5}, 5×10^{5}, 1×10^{6}, 2.5×10^{6} or 5×10^{6} PDP-PFCE labeled T cells were embedded in agar-filled Eppendorf tubes and imaged as described above or ^{19}F NMR experiments were performed by using a 400MHz NMR spectrometer with an Avance II console (Bruker Biospin GmbH, Rheinstetten, Germany) as described before

(270). For the latter cells were suspended in 5mm NMR tubes (Wilmad, Vineland, NJ, USA). A 5 mm broadband probe was used with an operating frequency for ^{19}F NMR of 376.50 MHz. For all ^{19}F NMR experiments, the following parameters were used: relaxation delay: 5 s, number of acquisitions: 1024, spectral width: 350 ppm and 128k data points. NMR data analyses/quantifications were performed using the TopSpin software (Bruker Biospin, Rheinstetten, Germany) by integrating ^{19}F NMR signals after phase and baseline corrections and comparison to an internal standard of known concentration.

As a reference compound, 5-fluorocytosine or sodium fluoride (0.1 ml, 5mM 19F concentration) was added to determine the chemical shift and ^{19}F concentration.

4.3.11 Statistical analysis

Data sets were analyzed using one-way ANOVA and Bonferroni's multiple comparison tests with Prism (version 6, GraphPad software, San Diego, USA). Data are represented as mean±SEM.

4.4 Results

4.4.1 In vitro labeling of NOD/BDC2.5 transgenic T cells with PDP-PFCE nanoparticles

Islet antigen-specific autoreactive T cells isolated from the spleen of NOD/BDC2.5 TCR Tg mice were isolated as described (287). T cells were activated with BDC 2.5 mimotope and labeled with PDP-PFCE NPs. Flow cytometry was performed for quantitative analysis of labeled T cells at 10 and 20mM PDP-PFCE NPs concentrations (Fig. 2).

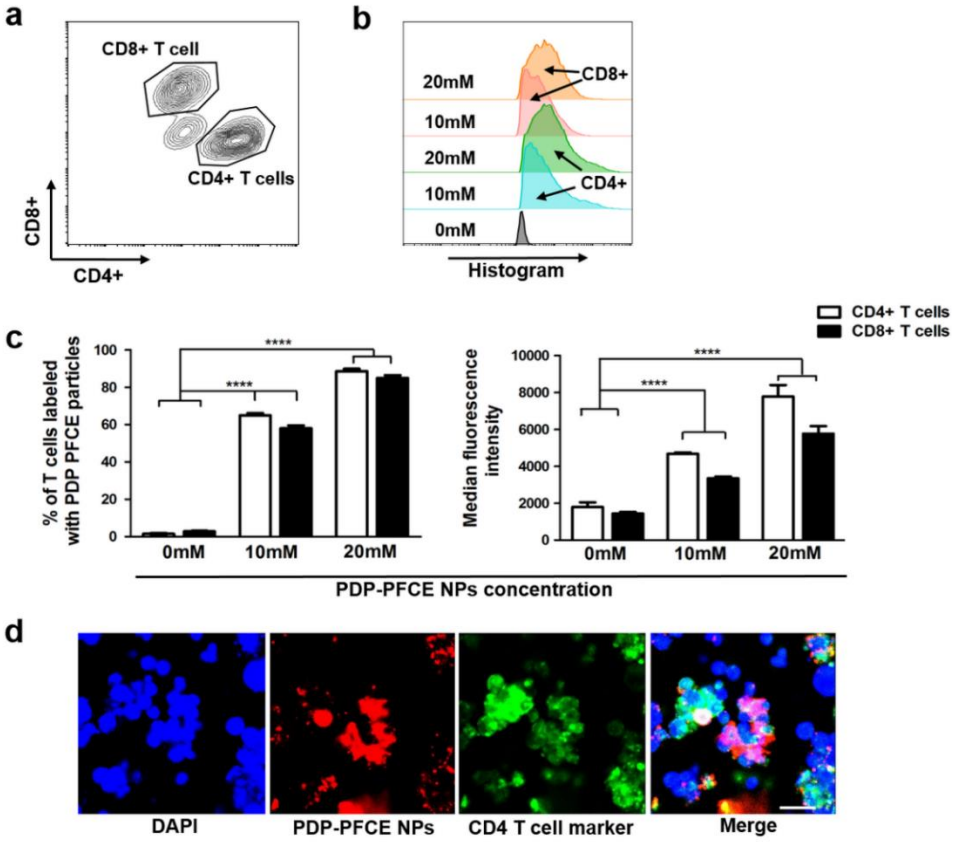

Fig. 2 Quantitative and qualitative analyses of T cells labeling with PDP-PFCE nanoparticles. a Specific T cell markers were used for the identification of CD4+ and CD8+ T cell populations. b Histogram representation of PDP-PFCE NPs labeled T cells at concentrations of 10 and 20mM, respectively. c Percentage of labeled CD4+ and CD8+ T cells and the median fluorescence intensities (MFI) were measured for fluorine concentrations up to 20mM PDP-PFCE by using flow cytometery (n=3, mean ± SEM, ****P<0.0001). d Qualitative confocal microscopy, showing CD4+ T cells labeled with PDP-PFCE NPs at the concentration of 20mM, (blue=nuclei, red=PDP-PFCE NPs, green= CD4+ T cell marker, scale bar = 20µm).

Both CD4+ and CD8+ viable T cells were analyzed for fluorine concentrations of 10 and 20mM to assess the association with PDP-PFCE NPs (Fig. 2a). A threshold median fluorescence intensity (MFI) was applied by implementing T cells without PDP-PFCE NPs (Fig. 2b). Consequently, the frequency of PDP-PFCE labeled cells and particles/cell was determined following exposure to two different particle concentrations (Fig. 2c). Maximal T cell labeling with PDP-PFCE NPs was observed at a fluorine concentration of 20mM. For the qualitative analysis of the PDP-PFCE NPs labeled T cells and further confirmation of label association, T cells were analyzed by confocal microscopy using a fluorine concentration of 20mM (Fig. 2d).

4.4.2 ^{19}F MR imaging and NMR spectroscopy of PDP-PFCE NPs labeled T cells

To estimate the detectable number of PDP-PFCE NPs labeled T cells, phantoms that contained different numbers of labeled T cells were prepared after labeling T cells with PDP-PFCE NPs using a total fluorine concentration of 20mM. As expected, a linear correlation was observed between the ^{19}F MRI signal intensity with the number of PDP-PFCE NPs labeled T cells (Fig. 3 a-b). The lowest detectable amount of T cells was approximately 5×10^5. The signal-to-noise ratio (SNR) for 5×10^5 PDP-PFCE NP labeled T cells in phantoms was 18.

Results obtained from ^{19}F NMR spectroscopy confirmed linear correlation between the number of ^{19}F spins with the amount of labeled T cells (Fig. 3c). Based on ^{19}F NMR spectroscopy, T cells contained on average $7\pm2\times10^{12}$ fluorine atoms/ cell. In order to test the detection limits of PDP-PFCE labeled T cells *in vivo*, we subcutaneously engrafted different amounts of labeled T cells subcutaneously in healthy mice. Based on the *in vivo* ^{19}F MR imaging, we were also able to detect down to 5×10^5 labeled T cells with an SNR of approximately 8 (Fig. 3 d-e).

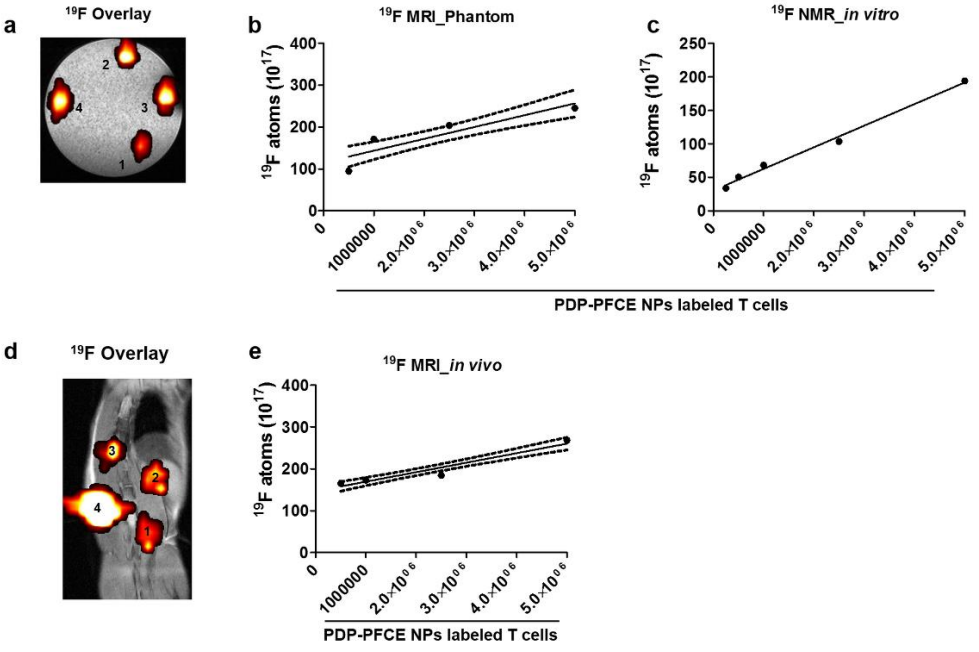

Fig. 3 *In vitro* and *in vivo* ^{19}F MR cell imaging and estimation of fluorine spins of PDP-PFCE NPs labeled T cells. a-b Overlay of fluorine signal obtained from phantom with different amounts of PDP-PFCE NPs labeled T cells and representation of the correlation between fluorine concentration and the number of PDP-PFCE NPs labeled T cells at different cell concentrations, (R= 0.9881), respectively. c ^{19}F NMR spectroscopy based quantification of fluorine atoms

from T cell (R= 0.9856). The signal intensity of PDP-PFCE NPs was compared to an internal chemical shift and concentration reference. d-e Subcutaneous implantation of different concentrations of PDP-PFCE labeled T cells in mice, for the quantification of fluorine signal and estimation of detection threshold (R= 0.9229). The PDP PFCE concentration used for labeling T cells was 20mM. 1= 5×10^5, 2= 1×10^6, 3= 2.5×10^6 and 4= 5×10^6.

4.4.3 In vivo assessment of autoreactive T cells labeled with PDP-PFCE NPs post-adoptive transfer in NOD.SCID mice

Autoreactive T cells were loaded with BDC2.5 mimotope and labeled with 20mM PDP-PFCE nanoparticles. The adoptive transfer of PDP-PFCE NPs labeled T cells in NOD.SCID mice was performed via intravenous injection where group 1 and 2 received 1×10^6 and 5×10^6 T cells, respectively. The control group did not receive T cells.

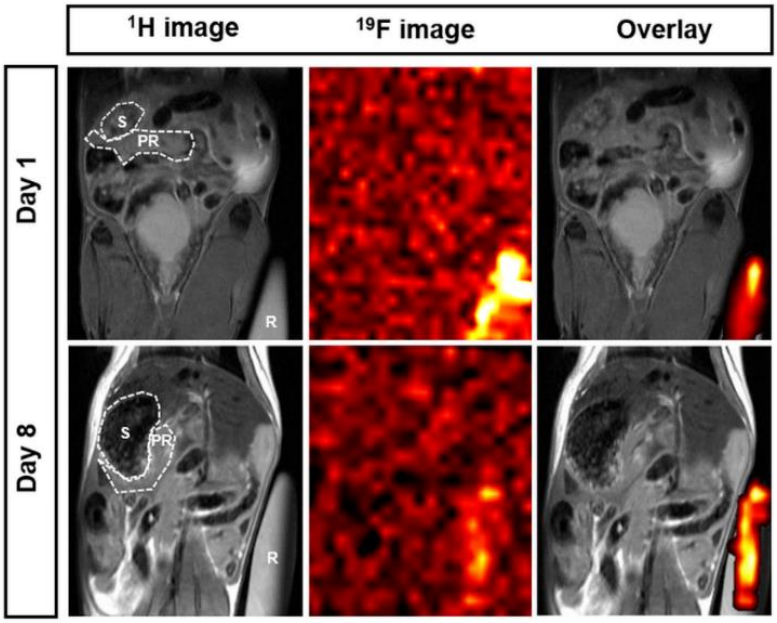

Fig. 4 Longitudinal *in vivo* MR imaging to follow-up PDP-PFCE NPs labeled T cells after adoptive transfer in a T1D model. All groups of animals were monitored by acquiring ^{1}H and ^{19}F MR images of the pancreatic regions from day 1 to day 8. The images shown above are from a representative animal that has received 5×10^6 labeled T cells. A fluorine reference (30mM) was placed next to the animal for the quantification of ^{19}F signal.

After 24h following adoptive transfer of PDP-PFCE NPs labeled T cells, ^{19}F MR images were acquired from all groups of NOD.SCID mice for up to 8 days. We did not observe any ^{19}F MRI

detectable fluorine signal from the pancreatic or other regions of all groups of NOD.SCID mice at any of the ^{19}F MR imaging time-points (Fig. 4).

4.4.4 Determination of T1D onset and ex vivo quantification of T cells in the pancreas

To verify whether transferred labelled T cells were functional *in vivo* and the loss of label was not because of cell death or dysfunctional T cells, we monitored blood glucose level and performed *ex vivo* flow cytometry. The onset of T1D was determined by recording the blood glucose levels on all non-fasted NOD.SCID animals from day 1 until day 12, post adoptive transfer of PDP-PFCE labeled T cells. As expected, animals receiving 5×10^6 labeled T cells showed an earlier onset of T1D (day 6) than animals receiving 1×10^6 T cells (day 10), as shown in Fig. 5a. The control group featured normal blood glucose concentrations.

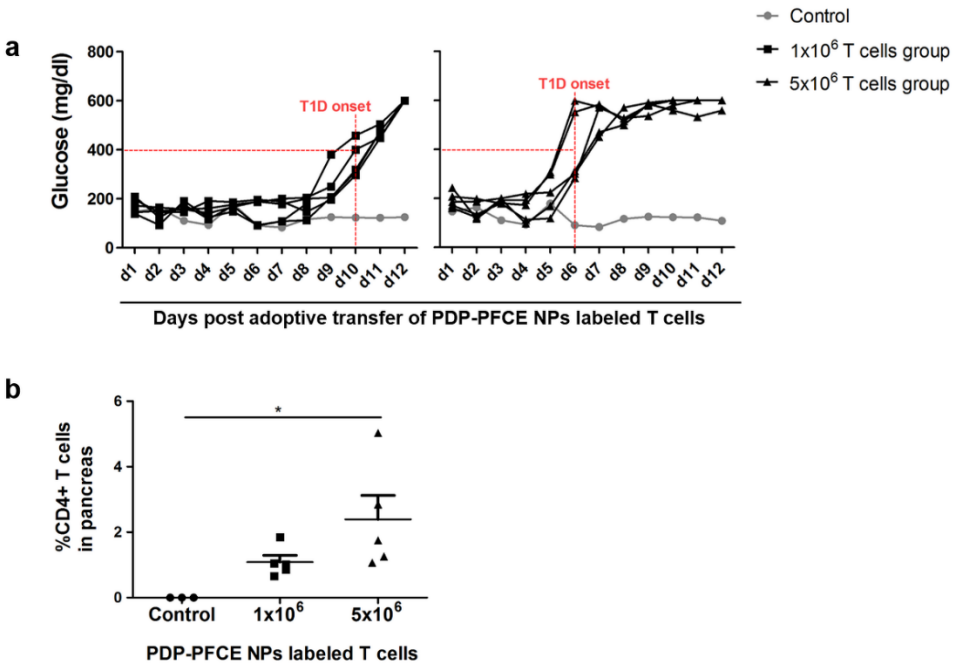

Fig. 5 Onset of type 1 diabetes and *ex vivo* flow cytometry of the pancreas. a After the labeled T cells engraftment, blood glucose level was measured for up to 12 days from non-fasted NOD.SCID animals to determine the onset of T1D. b *Ex vivo* flow cytometry on pancreases, showing the presence of CD4+ T cells detected on day 12 post transplantation in both mice groups (NOD.SCID mice, n=5, mean±SEM, *P< 0.05).

To quantify the number of migrating PDP-PFCE NPs labeled T cells in the pancreas, we performed *ex vivo* flow cytometry on day 12. We did not observe PDP-PFCE NPs labeled T cells as confirmed by flow cytometry. However, CD4+ T cells were observed in both the recipient NOD.SCID groups

with a higher percentage in the group receiving more cells (Fig. 5b). This shows that the T cells were functional and effectively migrated to the pancreas although, no association of PDP-PFCE NPs was observed with the isolated T cells.

4.4.5 In vitro assessment of PDP-PFCE label dilution in T cells

In order to explain the low degree of T cell labeling in the pancreatic region, we have assessed the dilution of PDP-PFCE NPs labeling of T cells with continued proliferation *in vitro*. Hereby, 5×10^6 T cells were labeled with 20mM PDP-PFCE nanoparticles and labeling was assessed at different time-points using flow cytometry.

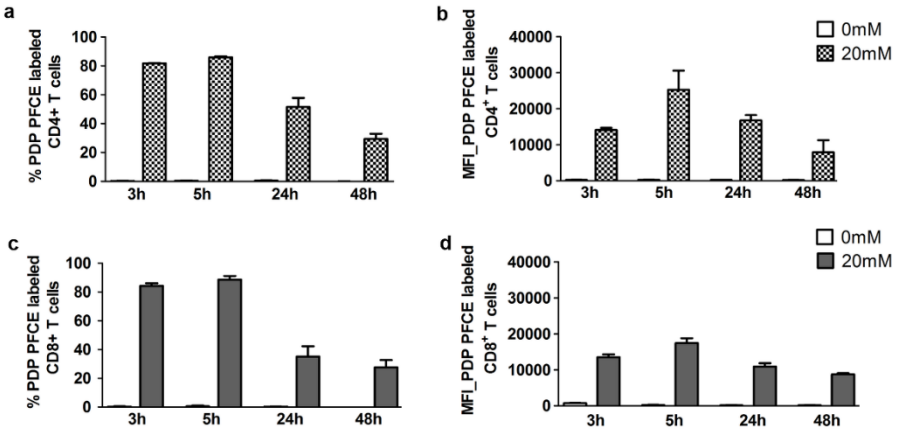

Fig. 6 *In vitro* assessment of PDP-PFCE labeling on BDC 2.5 activated T cells. **a-d** Quantification of the labeling and MFI of CD4+ and CD8+ T cells with PDP-PFCE particles (20mM fluorine concentration) for assessment of the label dilution for up to 48h, respectively (mean±SEM).

We found a decrease in the number of CD4+ and CD8+T cells labeled with PDP-PFCE nanoparticles after 24h (Fig. 6a,c). The median fluorescence intensities showed that the number of PDP-PFCE nanoparticles associated with T cells decreased rapidly over time (Fig. 6b-d).

4.5 Discussion

In T1D, the breach of tolerance mechanisms results in the emergence of self-reactive T cells, which infiltrate the islets along with monocytes/macrophages and destroy the pancreatic β-cells (276, 288). As inflammation is a hallmark of autoimmune diseases like T1D, it is important to assess the

onset and progression of these immunological processes. The high contrast specificity of ^{19}F MR imaging when compared to the use of SPIO agents is hence a promising imaging tool, which has been exploited for *in vitro* and *in vivo* visualization of tracer labeled immune cells and to quantify inflammation (149, 185, 186, 190, 196). In this study, we employed adoptive transfer of novel PDP-PFCE tracer-labeled autoreactive T cells into immunodeficient T1D susceptible animals. We followed the T cell recipient NOD.SCID mice aiming to visualize pancreatic inflammation by longitudinal ^{19}F MRI.

Delivery of magnetic nanoparticles (MNPs) *in vivo* has already been successful in demonstrating changes in the pancreatic vasculature of diabetic mouse models, after accumulation of labeled nanoparticles in infiltrating macrophages (289). However, labeling of non-phagocytic immune cells like T cells is challenging, as they do not follow the endocytic pathway for cellular uptake. While transfection agents are readily used to enhance the labeling of T cells also for ^{19}F MRI based tracking (196), chemical methods may affect physiological immune function of labeled T cells (290). Other large scale industrial processes were also exploited to label T cells by using commercially available ^{19}F tracers for monitoring T cell immunotherapy, however this procedure is difficult to implement for small scale laboratory experiments (291). We therefore assessed whether lipid modification of PFCE containing nanoparticles can facilitate their interaction with the T cell membrane, where we successfully labeled CD4+ and CD8+ T cells *in vitro* with PDP-PFCE nanoparticles. Comparison with previous attempts to label T cells with fluorine containing contrast agents for *in vivo* monitoring showed labeling efficiencies between 1 to 22×10^{12} fluorine atoms per cell (196, 283). Without using transfection agents, we were able to achieve T cell labeling in a similar concentration range (7×10^{12} fluorine atoms per T cell). From our ^{19}F MR imaging data of phantoms, we were able to quantify T cells in a range from 0.5 to 5 million T cells labeled with PDP-PFCE NPs, potentially suitable for accurate and quantitative cell tracking.

However, *in vivo* ^{19}F MR images showed no detectable fluorine signal from the pancreatic region of NOD.SCID recipient mice, engrafted with different amounts of labeled T cells. Transplanted animals became diabetic five days after adoptive transfer of labeled T cells, indicating that the engrafted T cells were able to migrate to the pancreas for the destruction of β-cells. Further, based on our *in vitro* PDP-PFCE label dilution experiments, we can conclude that the PDP-PFCE label was

probably diluted due to T cell proliferation in the pancreatic region. Based on these findings, T cells were sufficiently labeled with PDP-PFCE NPs for up to 48h, but the number of particles/cell was not sufficient to achieve detectable *in vivo* ^{19}F MR signal after sufficient local accumulation of T cells in the pancreatic region five days after engraftment. As measured by the ^{19}F MRI experiments of phantoms, the detectability threshold was estimated to be ~10^{16} fluorine atoms/voxel, which is comparable with previous publications (155, 292). This is sufficient for models of relative rapid local *in vivo* accumulation of labeled cells like the LPS model (188), but the *in vivo* detection of PDP-PFCE NPs labeled T cells in a T1D model remains elusive and challenging by using ^{19}F MR imaging. This illustrates the 'biological' requirements for making *in vivo* ^{19}F MRI based cell imaging successful: (a) sufficiently high amounts of locally accumulated labeled cells are needed, and (b) cell proliferation and associated label dilution should be minimal.

If these 'biological' requirements cannot be met, 'technical' improvements are needed like the development of more efficient fluorinated nanoparticles to achieve labeling of T cells, that is sufficient for *in vivo* monitoring by ^{19}F MRI. Synthesis of fluorine tracers with high number of fluorine atoms is required to compensate for the dilution after the cell divisions. To avoid the utilization of transfection agents, which have been used with fluorinated contrast agents for in vivo monitoring of T cells (196) we have used NPs with a modified surface (PDP-PFCE NPs). Although, we have achieved almost as high cellular fluorine concentrations as have been achieved with transfection agents (196) we failed to monitor T cell infiltration *in vivo*. Considering the efforts also taken by other research groups, this is not completely unexpected (283). Using terminally divided T cells or higher numbers of engrafted T cells than routinely used in this model are 'biological' modifications for achieving high *in vitro* labeling and *in vivo* visualization upon transfer in T1D model. However, as proliferation of T cells is their characteristic feature for the generation of adaptive immune response, such a model would be irrelevant to study inflammation in this disease model.

In conclusion, the utilization of transfection agents is currently the only approach that has resulted in sufficiently high fluorine concentrations for *in vivo* monitoring of T cells. As the utilization of transfection agents for diagnostic imaging in the clinic is currently not approved, other ways for achieving sufficient sensitivity of *in vivo* ^{19}F MRI of non-phagocytic cells may include more sensitive

and dedicated ^{19}F coils like cryogen cooled coils and improved processing methods like, compressed sensing techniques (293, 294).

However, it remains to be seen if these improvements will be sufficient to overcome the detectability limitations of ^{19}F MRI cell imaging applications for non-phagocytic cells. These improvements will further aid in the translation of preclinical methods to the clinical settings.

CHAPTER 5

Fluorine MR imaging probes dynamic migratory profiles of perfluorocarbon-loaded dendritic cells in a type 1 diabetes model*

Shweta Saini, An-Sofie Vanherwegen, Sayuan Liang, Rein Verbeke, Hannelie Korf, Ine Lentacker, Stefaan C. De Smedt, Conny Gysemans, Uwe Himmelreich.

*In preparation for publication in Journal of Molecular Imaging and Biology, Springer

5.1 Abstract

The pathogenesis of type 1 diabetes (T1D) involves presentation of islet-specific self-antigens by dendritic cells (DCs) to auto reactive T cells resulting in the destruction of insulin -producing pancreatic beta cells. We aimed to study the homing of diabetes-prone DCs to the pancreas and nearby organs with and without the presence of pancreatic stress to detect early onset of T1D. *In vitro* labeling of activated bone marrow-derived DCs (BMDCs) from NOD mice was performed using Zonyl perfluoro-15-crown-5-ether nanoparticles (ZPFCE-NPs). Internalization of particles was confirmed by confocal microscopy. NOD.SCID mice with or without stress to the pancreas, as induced by low dose streptozotocin (STZ) administration, were compared. Diabetogenic BMDCs loaded with BDC2.5 mimotope were pre-labeled with ZPFCE-NPs and adoptively transferred into NOD.SCID recipients. Longitudinal *in vivo* fluorine MRI (^{19}F MRI) was performed at 24h, 36h and 48h after transfer of BMDCs. For *ex vivo* quantification of labeled cells, ^{19}F NMR and flow cytometry were performed to validate *in vivo* ^{19}F MRI data. *In vitro* flow cytometry and confocal microscopy confirmed high uptake of nanoparticles in BMDCs during the process of maturation. Migration/homing of activated and ZPFCE-NPs labeled BMDCs to different organs was monitored and quantified longitudinally, showing highest cell density in the pancreas. Based on ^{19}F MRI, STZ-induced mild insulitis, along with high accumulation of ZPFCE-NP labeled BMDCs in the pancreatic region when compared to the vehicle group. In contrast, the vehicle-treated group featured elevated homing of labeled BMDCs to the pancreatic draining lymph nodes after 72h. We showed the potential of ^{19}F MRI for the non-invasive visualization and quantification of migrating immune cells during pancreatic inflammation. Without intrinsic background signal, ^{19}F MRI serves as a highly specific *in vivo* non-invasive tool to study the migration of diabetic-prone BMDCs in a T1D model. This approach could particularly be of interest for the longitudinal assessment of established or novel immunomodulatory and/or cell-based therapeutic approaches in preclinical models.

5.2 Introduction

Type 1 diabetes (T1D) is an autoimmune disease, resulting in the destruction of insulin-producing pancreatic beta cells. The disease mainly occurs in young children and during adolescents (216, 276, 295). The exact pathogenesis of T1D is still not fully understood, but is believed to be a

complex interplay between genetic risk and environmental triggers (296–298). The initiation of the disease involves the recruitment of immune cells surrounding and invading the islets of Langerhans (222, 288). Insulitis can also be induced by chemicals, such as streptozotocin (STZ) leading to acute or chronic injury of pancreatic tissue (299, 300).

Dendritic cells (DCs) are professional antigen-presenting cells that possess the ability to link innate and adaptive immunity by priming antigen-specific T cell responses. In addition, DCs are also involved in the induction of both central and peripheral tolerance (301–304). Studies in mouse models of T1D show that DCs are the main culprits for triggering pancreatic inflammation as they present islet-specific-autoantigens to islet antigen-specific T cells in the draining pancreatic lymph nodes (pLN) (225, 305).

The pathogenesis of T1D initiated by DCs after priming autoreactive T cells in the pancreatic draining lymph nodes is well studied in murine models of T1D (306–308). Many preclinical and clinical studies have investigated the multifactorial function of DCs during onset and progression of the autoimmune T1D (184). However, the kinetics of diabetogenic DC´s homing to the pancreas and pLN are still not fully understood due to the lack of methods that would allow longitudinal *in vivo* tracking of cells in individual animals or patients. Nowadays, T1D is generally diagnosed by performing blood tests, oral glucose tolerance tests and/or invasive biopsy of the pancreas. Unfortunately, these methods do not always reflect the actual inflammatory events occurring in the pancreas.

In this regard, non-invasive imaging of immune cells, provides a powerful tool to elucidate the inflammatory processes taking place in the pancreatic region upon an autoimmune trigger (11, 289, 309, 310). Over the past decade, imaging of the pancreas in rodent models has improved by using dedicated imaging techniques like magnetic resonance imaging (MRI), positron emission tomography (PET) or optical imaging techniques mainly based on novel contrast agents and tracers for pancreatic imaging (256, 309, 311, 312). Although, proton (^{1}H) MRI has been used for the visualization of inflammation in brain (313, 314), it’s application in the abdomen remains elusive due to hypointense background signal. In contrast, it has been shown that fluorine-19 MR imaging (^{19}F MRI) can track *in vivo* inflammatory events occurring in various diseases with

the help of *in vitro* and *in vivo* cell labeling applications using fluorinated contrast agents (176, 185, 186, 188, 315).

In this regard, ^{19}F MRI proves to be an effective and specific method to detect immune cells and their homing to even in the abdomen with the help of sensitive fluorine contrast agents like perfluorocarbons (PFCs). Perfluoro-15-crown-5-ether based nanoparticles (PFCE-NPs) contain 20 identical fluorine atoms and exhibit inert chemical properties, permitting it's wide use for the labeling and tracking of immune cells (281, 316). Recent developments of dedicated ^{19}F MR coils facilitate the dynamic tracking of PFC-loaded DCs in tumor patients undergoing immunotherapy (198, 317).

Therefore, it is imperative to combine ^{19}F MRI with biologically compatible fluorine contrast agents generating a relatively high signal-to-noise ratio for the evaluation of underlying inflammatory reactions in murine models of T1D disease. In the current manuscript, we employed newly synthesized PFCE-NPs based on zonyl fluorosurfactant to generate zonyl perfluoro-15-crown-5-ether nanoparticles (ZPFCE-NPs). ZPFCE-NPs were used to visualize and quantify the homing of labeled activated murine bone marrow-derived DCs (BMDCs) *in vivo* in immunodeficient diabetes-prone mice using ^{19}F MRI.

5.3 Materials and methods

5.3.1 Synthesis and characterization of fluorinated Zonyl-PFCE nanoparticles

The synthesis of biochemically inert perfluoro-15-crown-5-ether (PFCE) nanoparticles was performed as described previously (257). The anionic ZPFCE-NPs were further, prepared by incorporating additional zonyl FSP® surfactant to the PFCE particles. For the *in vitro* and *in vivo* experiments, ZPFCE-NPs were coupled with a DiR fluorescent dye (Molecular Probes, Invitrogen, Merelbeke, Belgium). The ZPFCE nanoparticles were subjected to a size and zeta potential quality control using a Malvern Zetasizer nano-ZS (Malvern Instruments Ltd, Worcestershire, UK).

5.3.2 Animals

Non-obese diabetic (NOD) mice (*n*=30) were originally obtained from Prof. Wu (Department of Endocrinology, Peking Union Medical College Hospital, Beijing, China) and were bred and housed

under semi-barrier conditions in the animal facility of KU Leuven. NOD.CB17-Prkdcscid/J (NOD.SCID) mice (*n*=18) were bred under specific pathogen-free conditions from stocks purchased from The Jackson Laboratory (Bar Harbor, ME, USA) in the animal facility of KU Leuven. Animals were housed at 22 °C on a fixed 12h light-dark cycle, with ad libitum access to food and water. Experiments were performed in accordance with regional, national and international standards on animal welfare. In particular, European Union Directive 2010/63/EU, and approved and overseen by the Animal Care and Ethical Committees of the KU Leuven.

5.3.3 Generation and labeling of BMDCs with ZPFCE-NPs

Bone marrow-derived dendritic cells (BMDCs) were generated from 3 to 4 week-old NOD mice as previously described (286). In brief, bone marrow precursor cells were isolated from the femora and tibiae and subsequently cultured in RPMI 1640 medium supplemented with Glutamax-I, 25 mM HEPES (Thermo Fisher Scientific, Merelbeke, Belgium), 10% heat-inactivated fetal calf serum (FCS, Merck, Darmstadt, Germany), 100 U/ml Penicillin, 100 mg/ml Streptomycin (Thermo Fisher Scientific, Merelbeke, Belgium), and 50 µM 2-mercaptoethanol (Thermo Fisher Scientific, Merelbeke, Belgium) in the presence of 20 ng/ml murine recombinant (r) IL-4 (Peprotech, Rocky Hill, NJ, USA) and 20 ng/ml murine rGM-CSF (Peprotech, Rocky Hill, NJ, USA) for 8 days. At day 3 and day 6 cytokines were refreshed. At day 8 of BMDC culture, CD11c+ cells were isolated by positive magnetic cell sorting (MACS, Miltenyi, Biotec, St-Louis, MO, USA). Subsequently, cells were matured for 24h in the presence of 1 µg/ml lipopolysaccharide (LPS, Merck, Darmstadt, Germany) and 20 ng/ml murine interferon r(IFN)-γ (Peprotech, Rocky Hill, NJ, USA) (Fig. 1).

During maturation, BMDCs were labeled with 20 mM of ZPFCE-NPs by adding the NPs to the medium for 24h. On day 9, mature BMDCs were harvested and pulsed with 10 µg/ml of BDC2.5 mimotope (AnaSpec, Freemont, CA, USA) for 2h at 37°C prior to *in vivo* injection.

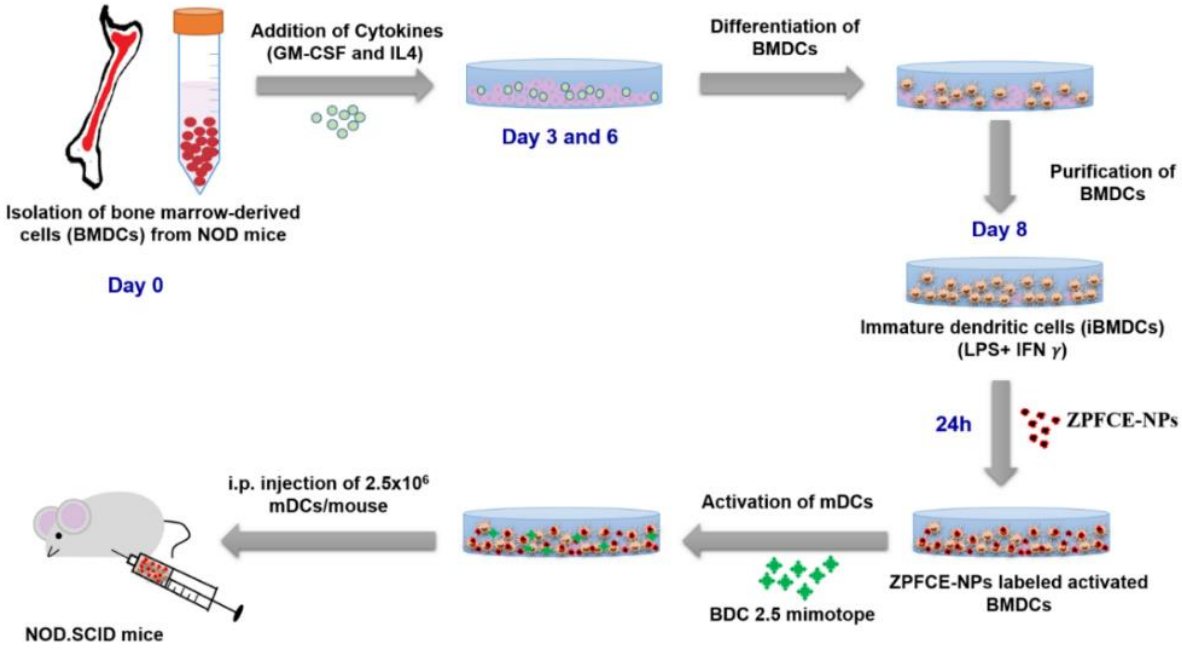

Fig. 1 Schematic representation showing harvesting of bone marrow derived and ZPFCE-NPs labeled dendritic cells. Antigen loaded pre-labeled dendritic cells were adoptively transferred into the NOD.SCID murine model for follow-up by ^{19}F MRI.

5.3.4 Flow cytometry

The *in vitro* labeling of BMDCs with ZPFCE-NPs was optimized at various concentrations (0, 1, 5 and 20 mM) and validated by flow cytometry. For the identification of ZPFCE-NPs labeled DCs, 2.5×10^5 BMDCs were first incubated with Fc receptor blocking antibody (Thermo Fisher Scientific, RRID:AB_467134) to minimize non-specific binding. Subsequently, cells were surface stained with a cocktail of the following antibodies against: major histocompatibility complex (MHC-II) I-A/I-E (Thermo Fisher Scientific, RRID:AB_465231), CD11c (Thermo Fisher Scientific, RRID:AB_465553) and F4/80 (Thermo Fisher Scientific, RRID:AB_914344). Doublets were excluded based on signal height and width. Dead cells were stained by Zombie Yellow Fixable Viability Kit (BioLegend, 423104, San Diego, CA, USA) according to manufacturer's guidelines and excluded from analysis. Samples were read on a Gallios™ Flow Cytometer (Beckman Coulter, Analis, Suarlée, Belgium) and analyzed with the FlowJo software v10.1 (TreeStar, Ashland, OR, USA).

5.3.5 Confocal microscopy

BMDCs labeled with ZPFCE-NPs were fixed in 4% PFA. Microscopy was performed using a confocal microscope (Nikon Eclipse A1R microscope, VIB 11, Center for the Biology of Disease, KU Leuven). Data were analyzed using the NIS Element software v4.10 (Nikon, Tokyo, Japan) and processed in Fiji software v1.49a (South Carolina, USA).

5.3.6 MR Imaging of phantom and longitudinal in vivo follow-up of ZPFCE-NPs-labeled BMDCs using ^{19}F MRI

Phantoms were prepared by embedding ZPFCE-NPs labeled BMDCs using agarose (2%) gel in Eppendorf tubes at 1×10^6, 2.5×10^6 and 5×10^6 cells ml^{-1} concentrations as described (318). Eppendorf tube with agar was used as a positive control. For *in vivo* ^{19}F MR imaging, one group of 5 to 6-week-old NOD.SCID female mice were injected intraperitoneally (i.p.) with 50 mg/kg streptozotocin (STZ) in citrate buffer, three days prior the adoptive transfer of DCs. The vehicle group received i.p. injections of sterile saline. After 72h, mice were engrafted with 2.5×10^6 BDC2.5-mimotope-loaded BMDCs derived from NOD mice and labeled with ZPFCE-NPs (Fig. 2). Control mice were injected i.p. with sterile saline. For *in vivo* ^{19}F MR imaging, animals were anesthetized by i.p. administration of a solution of 45-60 mg kg^{-1} ketamine (Nimatek, Eurovet animal health, AE Bladel, The Netherlands) and 0.6-0.8 mg kg^{-1} medetomidine (Domitor, The Orion Pharma, Espoo, Finland). *In vivo* MR images were acquired at 24h, 36h and 48h after the engraftment of ZPFCE-NPs labeled BMDCs using a purpose-built dual tuned $^1H/^{19}F$ purpose-built MR coil to acquire anatomical and fluorine images of liver and pancreatic region (319).

All MR experiments were performed on a 9.4T preclinical MR scanner (Bruker Biospec 94/20, Ettlingen, Germany) using a 2D RARE (Rapid Acquisition with Relaxation Enhancement) sequence with the following acquisition parameters: coronal slice orientation; for ^1H MRI: repetition time (TR) = 3500 ms, flip angle = 180°, Matrix size = 256×256, FOV = 50×40 mm, averages = 4, echo time (TE) = 6.121 ms, RARE factor = 8, in plane spatial resolution = 0.195mm×0.156mm, number of slices= 18, slice thickness = 1mm, total scan time = 5 minutes. Frequency shift from 400 MHz to 376 MHz was performed on the same coil for ^{19}F MR imaging. For ^{19}F MRI: TE= 4.86 ms, flip angle = 180°, Matrix size = 32×32, FOV = 50×40 mm, averages = 256, RARE factor=16, TR= 5388

ms, flip angle = 180°, spatial resolution= 1.56mm×1.25mm, number of slices= 9, slice thickness= 2 mm, total scan time = 25 minutes. Respiration rate and rectal body temperature of all animals was monitored throughout the experiment and maintained at 60-90 min^{-1} and at 37°C, respectively.

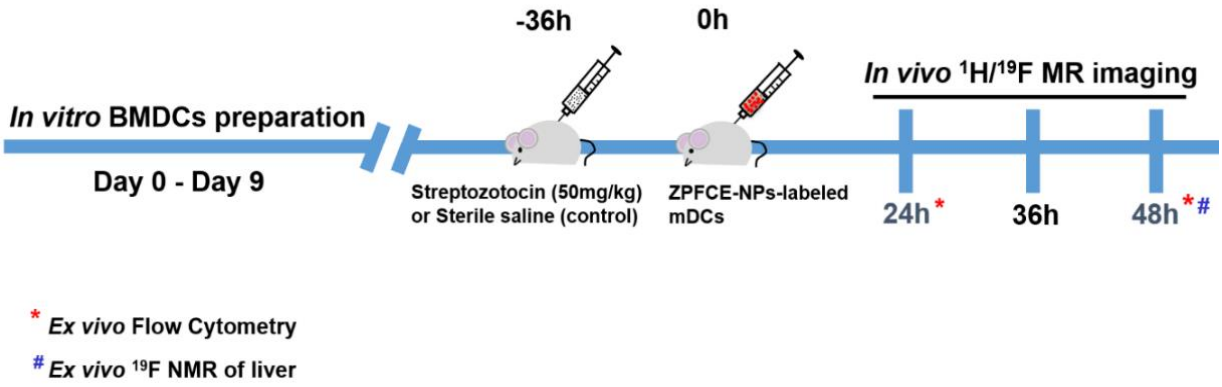

Fig. 2 Experimental timeline showing the induction of pancreatic stress by streptozotocin and administration of ZPFCE-NPs labeled BMDCs for their longitudinal follow-up. ZPFCE-NPs labeled BMDCs were quantified *ex vivo* by flow cytometry at 24h and 48h and *in vivo* using ^{19}F MR imaging at 24h, 36h and 48h. *Ex vivo* ^{19}F NMR spectroscopy of liver samples was performed at 48h after euthanizing the animal.

A reference Eppendorf tube (Eppendorf, Rotselaar, Belgium) containing 20mM ZPFCE-NPs embedded in 1% agar (Merck, Darmstadt, Germany) was placed parallel to the lower abdomen and was used for the quantification of fluorine atoms. After the MR data acquisition, anesthesia was reversed by i.p. injections of atipamezole (Antisedan, The Orion Pharma, Espoo, Finland).

5.3.7 Quantification of in vivo ^{19}FMR Images

^{1}H MR images were co-registered to ^{19}F MR images using MeVislab software v2.6.1 (MeVis Medical Solutions AG, Bremen, Germany). An interval threshold value (three times higher than the background noise) was applied to all ^{19}F MR images. ^{19}F MR images were masked using a Gaussian filter. The regions of interest containing fluorine signal were delineated and the mean of signal intensities were quantified using MeVislab software v2.6.1. For the identification of the pancreas and pLN, a mouse atlas for the abdomen was matched with the acquired anatomical ^{1}H MR images. The respective regions were delineated in the ^{1}H MR images. Regions were then

transferred to the co-registered ^{19}F MR images for quantification. The slice orientation and field-of-view were kept the same for exact overlay of MR images.

5.3.8 Ex vivo quantification of ZPFCE-NPs labeled BMDCs in excised organs

Pancreas and pLN were extracted from mice after 24h and 48h after injection of BDC2.5 mimotope-loaded ZPFCE-NPs-labeled BMDCs. Pancreases were minced into small fragments and digested in pre-warmed digestion medium containing 1mg/ml collagenase VIII (SERVA, Heidelberg, Germany) and 20 µg ml^{-1} DNase I (AppliChem, Darmstadt, Germany). Enzymatic digestion was performed for 30 min at 37°C, under continuous rotation using a rotarod. All single-cell suspensions were passed through a 70µm strainer (Miltenyi Biotec, Leiden, The Netherlands). Red blood cells were lysed using NH_4Cl at 37°C. For flow cytometry analysis, cells were stained as described above.

5.3.9 Ex vivo ^{19}F NMR spectroscopy

ZPFCE-NPs-labeled BMDCs that migrated to the liver 24h and 48h post injection were quantified from excised tissue samples *ex vivo* by determining fluorine concentrations using ^{19}F NMR spectroscopy. Livers were dissected and homogenized in PBS solution and transferred to 5 mm NMR tubes (Wilmad, Vineland, NJ, USA). For the acquisition of data, an NMR spectrometer (400MHz) with an Avance II console (Bruker Biospin GmbH, Rheinstetten, Germany) was used. An operating frequency of 376.50 MHz was used for ^{19}F NMR. The following parameters were used for data acquisition: relaxation delay: 5 s, number of acquisitions: 1024, spectral width: 350 ppm and 128k data points. A reference tube containing 20mM ZPFCE-NPs prepared in agar was added for quantification. Data analyses were performed after phase and baseline correction by peak integration using the TopSpin software (Bruker Biospin, Rheinstetten, Germany).

5.3.10 Statistical analysis

Statistical significance was determined using One-way ANOVA tests with Bonferroni's multiple comparison tests. Results were expressed as mean values ± SEM. All statistical analyses were performed using GraphPad Prism v5.3 (GraphPad software, La Jolla, CA, USA).

5.4 Results

5.4.1 Composition and quantification of fluorinated ZPFCE nanoparticles for BMDCs labeling

Anionic ZPFCE-NPs were synthesized by addition of the zonyl FSP fluorosurfactant to the lipid layers of PFCE-NPs in order to reduce their diameter to ~280 nm. The zeta potential of ZPFCE-NPs was -75 mV, indicating a high stability of these particles (Fig. 3a). The core compound of the ZPFCE-NPs consisted of 20 identical fluorine atoms. The size distribution of ZPFCE-NPs is indicated as the polydispersity index (PdI) ~ 0.312.

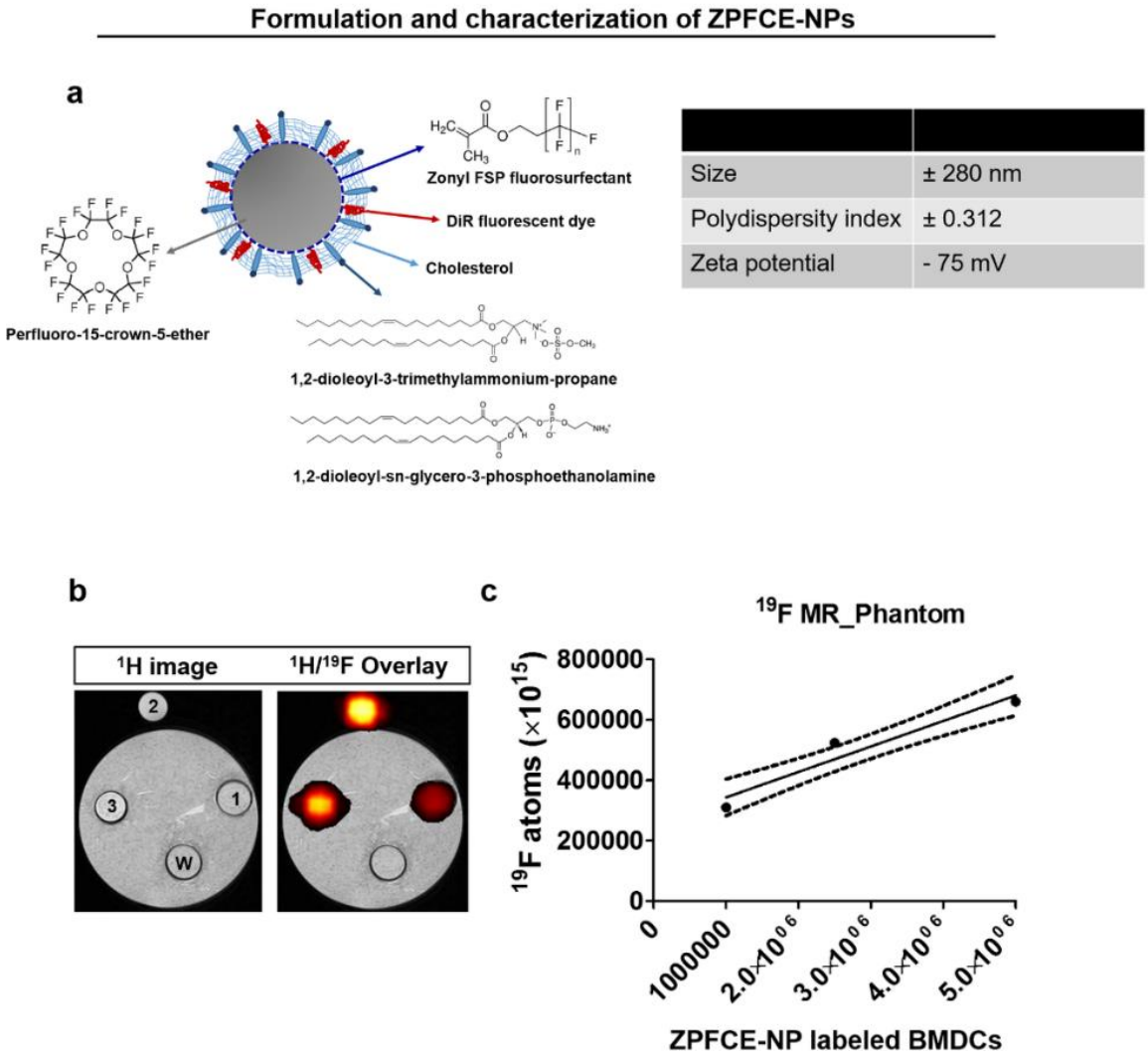

Fig. 3 Chemical composition, characteristic features of ZPFCE-NPs and *in vitro* characterization by ^{19}F MR imaging of ZPFCE-NPs loaded BMDCs in agar phantoms. **a** Illustrative image of lipid encapsulated PFCE-NPs consisting of

perfluoro-15-crown-5-ether with 20-identical fluorine atoms surrounded by zonyl fluorosurfactant. The lipid layers were conjugated with near infrared DiR fluorescent dye for microscopic imaging experiments. Zeta potential and polydispersity index indicate the stability and heterogeneity of ZPFCE-NPs. **b** ^{1}H and $^{1}H/^{19}F$ MR overlaid images of agar phantoms containing cells that were labeled for 24h with 20mM ZPFCE-NPs (fluorine concentration) were overlaid on the ^{1}H MR images. ^{19}F MR images are indicated as hot spots using pseudo color. Labeled BMDCs were centrifuged and counted prior to fixation in agar. (**1**= 1×10^{6}, **2**= 2.5×10^{6}, **3**= 5×10^{6}, **w**= water). **c** Quantification of the fluorine content was performed by delineation of 'hot spots' marked as the regions of interest based on the ^{19}F MR images (R= 0.9047).

The near infrared DiR fluorescent dye was incorporated in the particles in order to confirm the labeling of BMDCs. For the quantification of fluorine atoms taken up by BMDCs, *in vitro* ^{19}F MRI phantom experiments were performed. BMDCs were labeled with 20mM ZPFCE-NPs for 24h and cells were embedded in agar at quantities of 1×10^{6} ml^{-1}, 2.5×10^{6} ml^{-1} and 5×10^{6} ml^{-1}, respectively for ^{1}H and ^{19}F MR imaging. (Fig. 3b-c). BMDCs showed a linear correlation in uptake of the ZPFCE-NPs at all the cellular concentrations.

5.4.2 In Vitro Characterization of ZPFCE-NPs Labeled BMDCs

First, we performed *in vitro* labeling experiments to find the optimal procedure to achieve high cellular uptake. After purification of $CD11c^{+}$ cells on day 8, BMDCs were either matured for 24h in the presence of ZPFCE-NPs (indicated as iDCs) or matured for 24h after which ZPFCE-NPs were added for an additional 24h (indicated as mDCs). For both conditions, 1 mM, 5 mM and 20 mM ZPFCE-NPs were used. The uptake of ZPFCE-NPs was quantified in $CD11c^{+}$ $MHC\text{-}II^{+}$ BMDC rich population using flow cytometry. The percentage of BMDCs associated with ZPFCE-NPs was found to be significantly higher when ZPFCE-NPs were added during maturation compared to when adding the ZPFCE-NPs after maturation (Fig. 4a). Moreover, the amount of ZPFCE-NPs taken up by the maturing BMDCs increased as indicated by the significant increase in mean fluorescence intensity (MFI) (Fig. 4b). This confirms that DCs, and in particular immature DCs, are specialized in antigen capture (39, 302). Both percentages and MFIs indicated the most efficient labeling of BMDCs with 20 mM ZPFCE-NPs (Fig. 4 a-b).

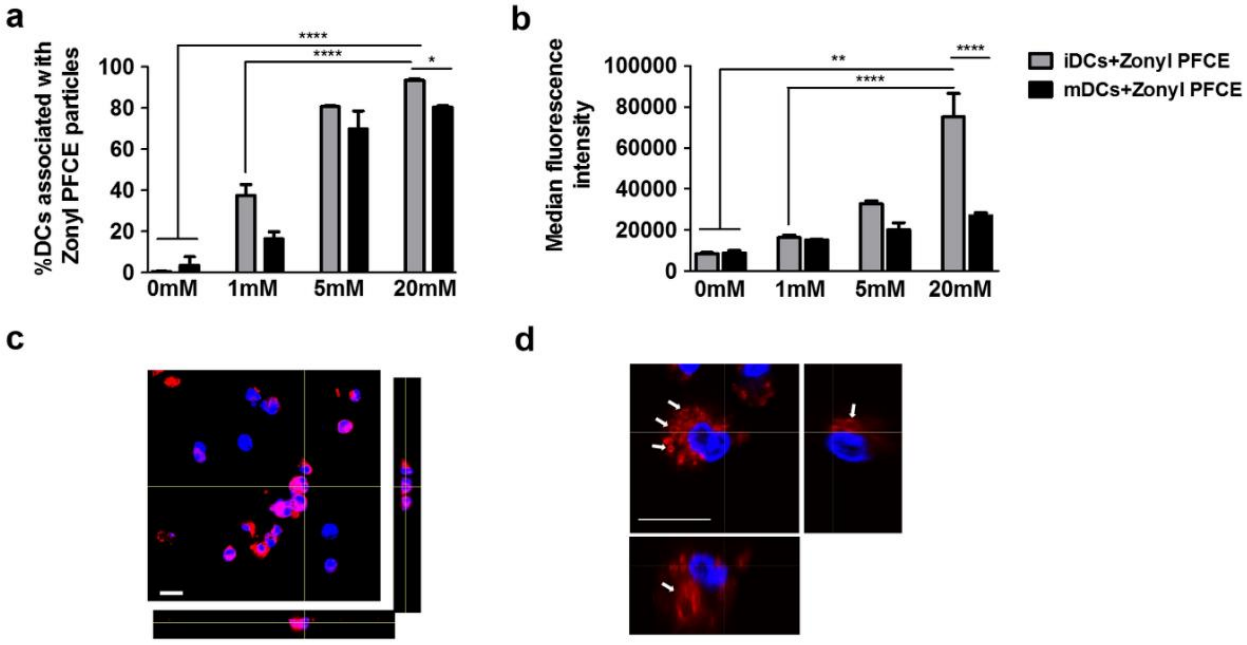

Fig. 4 *In vitro* analysis of ZPFCE-NPs labeled BMDCs. BMDCs were matured for 24h in the presence of 1 mM, 5 mM or 20 mM ZPFCE-NPs (iDCs) or matured for 24h after which 1 mM, 5 mM or 20 mM ZPFCE-NPs were added for an additional 24h (mDCs). **a** Percentage of ZPFCE-NP^{+} cells and, **b** mean fluorescence intensity (MFI) of ZPFCE-NPs in the CD11c^{+} MHC-II^{+} BMDC population was determined by flow cytometry (*n*=3). **c-d** Representative confocal microscopy images are shown as z-stacks in three dimensions of fixed iDCs confirming internalization of nanoparticles by iDCs. Nuclei were stained with Hoechst dye (blue), ZPFCE-NPs (red) are indicated with white arrows. The scale bar is 20µm. Data are represented as mean±SEM. (NOD mice, *n*=3, *p<0.05, **p<0.01, ****P<0.0001).

Further, confocal microscopy illustrated the internalization of the ZPFCE-NPs as three-dimensional scanning microscopy images of cells, confirming efficient cytoplasmic uptake of nanoparticles by BMDCs at the 20mM concentration (Fig. 4c-d).

5.4.3 ^{19}F MR Imaging of the Pancreatic Region After Adoptive Transfer of ZPFCE-NPs Labeled BMDCs

NOD/ShiLtSz-Prkdc^{scid} mice are insulitis-free and do not develop T1D spontaneously. In our experimental set-up, we used NOD.SCID mice to track the *in vivo* migration of BDC2.5 mimotope-loaded ZPFCE-NPs-labeled BMDCs. To induce beta cell injury, one group of mice was pre-treated

with a single injection of 50 mg/kg STZ. Prior to the adoptive transfer, BMDCs were analyzed using flow cytometry to ensure viability and sufficient uptake of ZPFCE-NPs. In these experiments ~98% of the BMDCs are ZPFCE-NPs positive (Supple. Fig. S1a) with significantly higher particle-cell association compared to the controls (Supple. Fig. S1b). Based on these results, 2.5×10^6 BDC2.5 mimotope-loaded ZPFCE-NPs labeled BMDCs were engrafted in the vehicle- and STZ-treated groups. Control NOD.SCID mice received i.p. injection of saline.

^{19}F MR imaging of all mice groups was performed. Images of the pancreatic region and liver were quantified for their fluorine content. Based on the anatomical ^{1}H MR images and overlay with a mouse atlas, regions of interest that correspond to the respective organs were transferred to the ^{19}F MR images and quantified relative to the external ^{19}F reference. The temporal profile of the homing of ZPFCE-NPs labeled activated BMDCs in which, compared between the vehicle and the STZ-treated group. A significantly higher accumulation of labeled cells was detected in the pancreas of the STZ-treated group 48h post transfer compared to the vehicle-treated group (Fig. 5 a,d). Interestingly, high fluorine signal intensities were observed and quantified in the pLNs of the vehicle group as compared to the STZ-treated group (Fig. 5b). Finally, low ^{19}F signal intensity from the liver of both vehicle and STZ-treated groups was acquired, indicating the deposition of a small number ZPFCE-NPs labeled BMDCs in this organ (Fig. 5c).

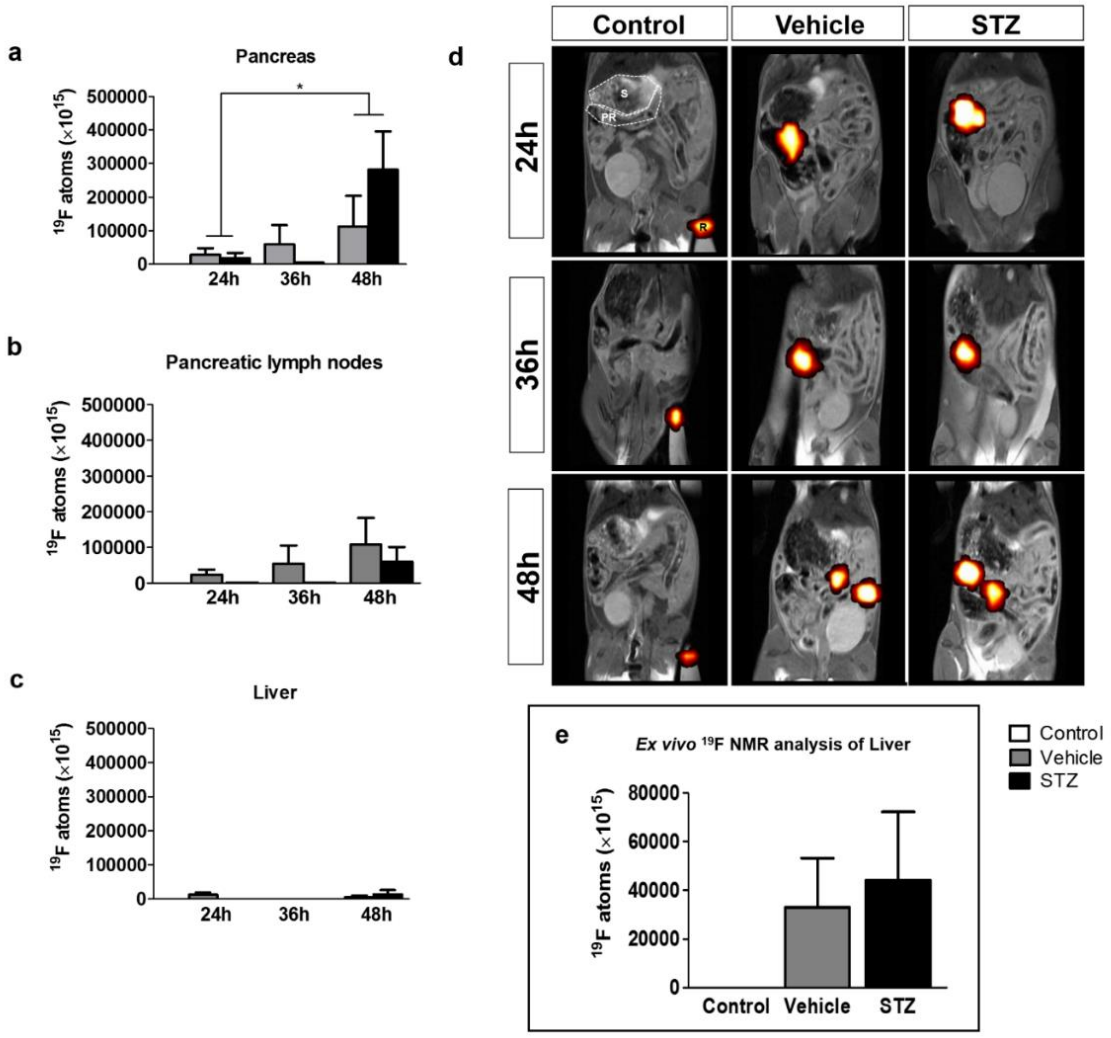

Fig. 5 Quantification and distribution of ZPFCE-NP Labeled BMDCs. At 24h, 36h and 48h after adoptive transfer of BDC2.5 mimotope-loaded and ZPFCE-NP labeled BMDCs, ^{19}F MRI was performed to assess the cell distribution *in vivo*. **a-c** Fluorine signal was quantified as the number of fluorine atoms/voxel in organs of high ZPFCE-NP accumulation (pancreatic region and liver) based on the overlay of ^{19}F and anatomical ^{1}H MR images relative to an external reference of known concentration (R). **d** *In vivo* ^{19}F MR images of the abdominal region of control animals (no BMDCs), vehicle- and STZ-treated NOD.SCID mice (NOD.SCID, *n* = 13) showing fluorine signal due to accumulation of the ZPFCE-NP-labeled BMDCs 24h (top), 36h (middle) and 48h (bottom) after cell engraftment. **e** *Ex vivo* ^{19}F NMR spectroscopy was used for the quantification of fluorine content in the liver (NOD.SCID, *n* = 5). Data represented as mean ± SEM, *p<0.05. R= ^{19}F 20 mM reference.

Additionally, *ex vivo* ^{19}F NMR spectroscopy was performed on liver homogenates to cross-validate quantification of *in vivo* ^{19}F MRI data, after euthanasia of the animals and 48h after cell

engraftment. The ^{19}F NMR data confirm *in vivo* ^{19}F MRI. No significant differences in the migration of ZPFCE-NPs labeled BMDCs in vehicle and STZ-treated mice were observed (Fig. 5e).

5.4.4 Validation of In vivo ^{19}F MRI by Flow Cytometry After Adoptive Transfer in NOD.SCID Mice

For further confirmation of the *in vivo* monitoring of BDC2.5 mimotope-loaded and ZPFCE-NP labeled BMDCs and their migration towards the pancreas and pLNs, a small cohort of NOD-SCID mice was euthanized 24h and 48h after adoptive transfer. Migration of labeled BMDCs towards the pancreas and pLNs was then assessed by flow cytometry (Fig. 6). More ZPFCE-NP labeled BMDCs were seen after 48h compared to the 24h time-point. However, no differences in the accumulation of ZPFCE-NP labeled BMDCs were observed between the pancreases of vehicle- and STZ-treated mice groups. A strong reduction in ZPFCE-NPs labeled BMDCs was seen in the pLNs of STZ-treated animals but not for the vehicle-treated animals after 48h when compared to the animals euthanized after 24h after 48h, suggesting that most of the ZPFCE-NP labeled BMDCs might have migrated to the pancreas (Fig. 6g).

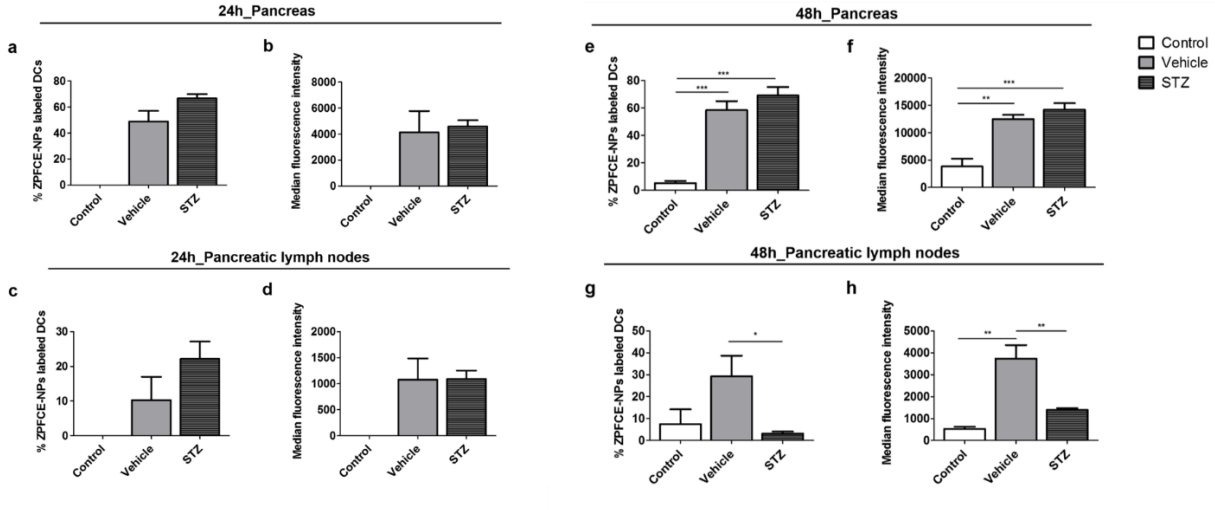

Fig. 6 Quantification of ZPFCE-NPs-labeled BMDCs isolated from control, vehicle and STZ-treated NOD.SCID mice 24h (a-d) and 48h (e-h) after intraperitoneal engraftment by flow cytometry. The percentage of ZPFCE-NPs$^+$ cells in the CD11c$^+$ MHC-II$^+$ DC population was determined in the pancreas (a, e) and pLN (c, g). MFI of ZPFCE-NPs in the CD11c$^+$ MHC-II$^+$ DC population determined in the pancreas (b, f) and pLN (d, h). Bar graphs represent mean ± SEM (n = 8). *p<0.05, **p<0.01, ***P<0.001.

5.5 Discussion

Monitoring inflammation as hallmark in the pathogenesis of various diseases is gaining high interest for a better understanding of diseases and their treatment (225, 320–322). Here we studied a mouse model of T1D with and without STZ-induced pancreatic injury with mild pancreatic inflammation. We aimed to track and quantify the migration of adoptively transferred ZPFCE-NP-labeled BMDCs towards the pancreas. DCs play a crucial role in the balance between immunity and tolerance (323–325). This has resulted in an increased interest in DCs. Applications also include the use of DCs in immunotherapy (326–330). In T1D, DCs are key players in both the prevention and induction of this autoimmune disorder. DCs have been extensively studied preclinically in NOD mice (301, 302, 331). Together with self-reactive T cells, DCs are involved in all stages of T1D (332). Although, the role of DCs in mouse models of T1D have been studied previously (286), non-invasive follow up of individual animals over time would provide a better insight in the sequential events and migration of DCs within the host. In this regard, we employed ZPFCE-NP labeled BMDCs in order to track migration of labeld BMDC under conditions of mild inflammation. Successful preclinical studies conducted on the tracking of DCs using MRI and superparamagnetic nanoparticles have been further optimized for future applications in humans (333, 334). Other studies investigated the labeling of DCs with multifunctional nanoparticles incorporated with therapeutic agents, such as anticancer drugs for theranostic applications using ^{19}F MRI (184, 257).

Imaging techniques, such as ^{19}F MRI are very promising tools for the non-invasive longitudinal study and tracking of labeled cells (198, 256, 281, 335, 336). An advantage of ^{19}F MRI based cell labeling strategies is the lack of background signal and the ease to combine it with anatomical information retreived from ^{1}H MRI. One disadvantage of ^{19}F MRI is its poor sensitivity (337). PFCEs are the preferred choice for ^{19}F MRI based cell tracking, since their 20 identical fluorine atoms partially help to overcome the methods sensitivity problems (255, 338). Here, we report on modified PFCE-based particles for the BMDCs labeling that are smaller and more stable than those reported in the literature.This has resulted in a relatively high uptake of ZPFCE-NPs by BMDCs when added during the maturation process. This results in high NP accumulation that is required for *in vivo* tracking of labeled cells by ^{19}F MRI (337). PFCEs are biologically inert

compounds. Their encapsulation within liposomes is well studied with no known biological side-effects on the cells during or after the labeling procedures (176, 254, 339, 340). It has previously been shown that different sizes of PFCE-NPs used for cell labeling results in immunogenic DCs (261). In the current study, no adverse effects of ZPFCE-NPs labeling were detected on BMDC on the viablility, phenotype and function when using a concentration of 20 mM ZPFCE-NPs as cells were able to retain their functional properties.

Using ^{19}F MR imaging, we showed that BDC2.5 mimotope-loaded ZPFCE-NP labeled BMDCs migrated with high affinity towards the pancreas after chemically induced (low dose STZ) inflammation. The increased homing of BDC2.5 mimotope-loaded ZPFCE-NP-labeled BMDCs was observed in the pancreatic region of STZ-treated group compared to the vehicle-treated group at 48h. This could be the result of the disrupted pancreatic vasculature due to STZ-induced inflammation. We identified high accumulation of fluorine atoms in the pLN of the vehicle group. Based on the *ex vivo* flow cytometry analyses of pancreas, no significant differences were found in the number of ZPFCE-NP labeled BMDCs of both injected groups at 24h and 48h. However, significantly elevated homing of ZPFCE-NP-labeled BMDCs was noticed in the pLNs of the vehicle group in contrast to the STZ-treated group. Apart from the pancreatic region, low ^{19}F signal was also detected in the liver (286), in our study this might have resulted from dead ZPFCE-NP labeled BMDCs or free nanoparticles released from dead cells, as previously shown.

In the current manuscript we established a labeling protocol for BMDCs using newly synthesized ZPFCE-NPs. Moreover, we provided a ^{19}F MRI platform for the non-invasive imaging and quantification of BDC2.5 mimotope-loaded ZPFCE-NP-labeled BMDCs in T1D mouse model under mild pancreatic inflammation. Further studies will help in the evaluation of the labeling and ^{19}F MR imaging of DCs for longitudinal follow-up of tolerogenic DCs in T1D animals with a future translation (341, 342). Apart from this, this imaging approach can also be implemented for the development of theranostic applications using fluorinated nanoparticles for the DC vaccines in cancer, while it is already ongoing in humans (198, 269).

Briefly, we showed successful labeling of BMDCs with biologically compatible ZPFCE-NPs for the *in vivo* and longitudinal follow-up of mild pancreatic inflammation in a T1D mouse model using

^{19}F MRI. Our findings depict the feasibility of using ^{19}F MRI and ZPFCE-NPs for monitoring and quantifying the dynamics of inflammation in T1D. Our work will contribute in the further assessment of novel cellular-based immunotherapies such as tolerogenic DC vaccines not only in T1D studies but also for the development of cancer vaccines.

5.6 Supplementary material

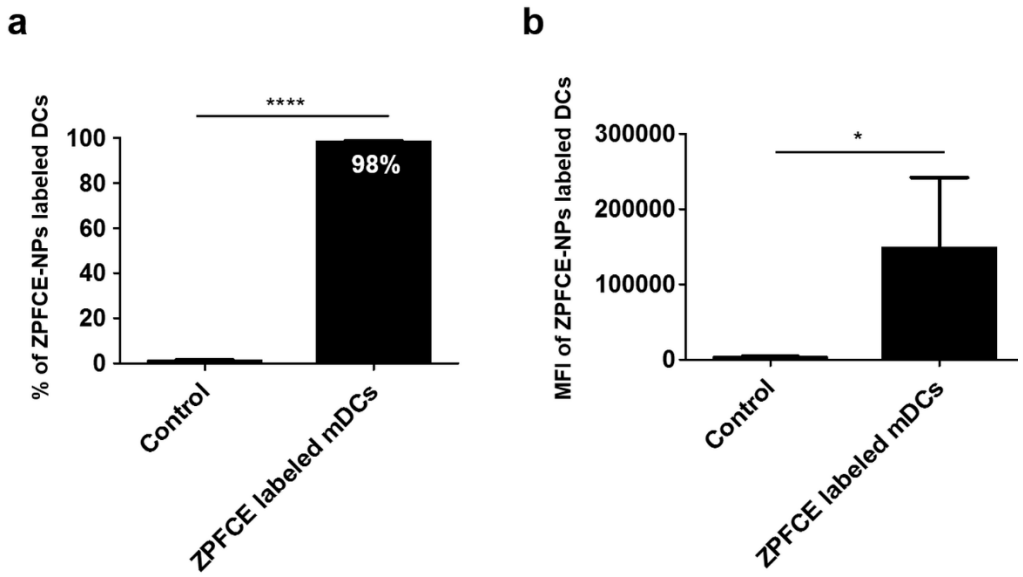

Fig. S1 *In vitro* flow cytometry analyses of DCs 24h after labeling with ZPFCE-NPs and prior to adoptive transfer in NOD.SCID mice, **a** percentage of ZPFCE-NPs labeled DCs and, **b** number of particles per cell (median fluorescence intensity). Data represented as mean±SEM. (*n*=3, *p<0.05, ****P<0.0001).

CHAPTER 6

General discussion and future perspectives

In many diseases, inflammation is a first response to the pathophysiological conditions originated from injury or infection in living beings. Inflammation is a natural phenomenon where the body attempts to save life by triggering innate and adaptive immunity. However, if immune cells become dysregulated or are attenuated by immunosuppressive drugs, uncontrolled inflammation can result in autoimmune disease or lethal infections. From the adhesion of immune cells to the endothelial cell wall to their invasion into tissue, each event is tightly controlled by cytokine and chemokine signaling (185). Depending on the trigger, inflammation can be acute or chronic. Since immune cells are actively involved in the initiation of inflammation, they are of high interest for understanding the mechanisms of the body's defense system.

Noninvasive molecular imaging techniques are readily used for immune cell tracking to elucidate the biological role in different underlying pathophysiological conditions (3). These imaging techniques allow the longitudinal assessment of various immune cells in their native biological environment. In this context, cellular therapeutics are gaining momentum where manipulated cells are administered in the patient's body to help combating the disease. Recent studies demonstrate increased used of immune cells in cancer and autoimmune diseases for therapeutic applications (1). Many different imaging modalities like MRI, CT, BLI, FLI, PET etc. are used in combination with imaging agents for studying the inflammatory patterns occurring in different disorders (149, 191, 343–346). In many cases, these modalities are combined with multimodal approaches to extract anatomical and quantitative molecular information. Each of these different imaging techniques has their own advantages and disadvantages.

In this thesis, we have exploited different MRI techniques. Thanks to its non-ionizing nature and high contrast soft tissue of MRI, it provides anatomical information and contrast for tracking of immune cells. Since conventional ^{1}H MR imaging lacks specific information/contrast on particular cell types, we combined ^{1}H MRI with ^{19}F MRI. ^{19}F MRI provides contrast for direct cell tracking and quantification when used with potent fluorinated contrast agents. In this thesis, we studied different disease models, where inflammation plays a critical role. With help of different fluorinated contrast agents, we showed labeling, tracking and quantification of different immune cells types using *in vivo* ^{19}F MRI.

Firstly, we studied macrophages, which is a professional phagocytic immune cell for the optimization of cell labeling methods using perfluorocarbon-based nanoparticles (Chapter 3). Previous publications have successfully demonstrated the *in vivo* labeling of macrophages by systemic administration of PFCE-NPs in order to trace inflammation occurring in various disorders (255, 347). With the help of ^{19}F MRI, pulmonary acute inflammation was studied using a lipopolysaccharide (LPS) induced mouse model, where PFCE-NPs were administered for the quantification of *in vivo* labeled macrophage in lungs (188).

In our study, we tested modified ZPFCE-NPs. The potential use of any type of nanomaterial for cell labeling can hamper or damage the normal physiological function of cells. Therefore, relevant nanotoxicity tests should be conducted to ensure the safety and suitability of these nanomaterials for *in vitro* and *in vivo* cell labeling applications. In this context, studies have been conducted to assess several cellular mechanisms upon labeling with nanomaterials like the formation of reactive oxygen species, cell morphology, cell viability, differentiation and activation etc. (348, 349). Based on our *in vitro* nanotoxicity assays, we found that ZPFCE-NPs are biocompatible, as they did not induce direct toxicity in primary murine macrophages for concentrations up to 10 mM.

We further studied the biological function of macrophages, which is the presentation of antigens to T cells. We found no abnormal behavior of ZPFCE-NP labeled macrophages as they retained their antigen presentation and T cell activation function. After satisfactory validations of nanosafety and *in vitro* labeling assays, the optimal dose of ZPFCE-NPs was confirmed for *in vivo* labeling of macrophages. To establish a modus operandi for the *in vivo* tracking and labeling of macrophages, we used a pulmonary fungal infection model. Here, we performed *in vivo* labeling of macrophages using ZPFCE-NPs and assessed their migration to the pulmonary site of infection in an invasive pulmonary aspergillosis mouse model (IPA). IPA is a fungal disease, which in case of immunosuppressive medications can be lethal for patients. For example, patients with organ transplants receive these drugs in order to suppress immune system. These patients but also patients with an otherwise impaired immune system (for example, HV) are more susceptible to airborne *Aspergillus fumigatus* invasion. Depending on the type of immune suppression, the effect of different types of immune suppression varies in terms of the immune response.

We demonstrated dynamic longitudinal quantification of macrophages in the pulmonary region of IPA mice under corticosteroid based and cyclophosphamide immunosuppression. For the *in vivo* labeling of macrophages, we intravenously injected ZPFCE-NPs and performed ^{19}F MRI using home-built ^{1}H/^{19}F surface coil at different time-points of the disease. Using ^{19}F MRI, we noninvasively monitored and quantify inflammation in the fungal invaded pulmonary area. We showed that the fluorine signal in the inflamed region directly correspond to the infiltrated ZPFCE-NPs labeled phagocytes. This is in agreement with previous studies where macrophages were used for the estimation of inflammation in various disease models using ^{19}F MRI (188, 315, 347, 350, 351). In our study, we observed differences between healthy animals and animals with impaired immune system in their reaction against an *A. fumigatus* challenge. High fluorine signal intensities were observed in the lungs of infected immunocompetent mice at 4h post infection, which decreased significantly within 24h after the fungal conidia were cleared by immune cells.

On the other hand, immunocompromised mice showed distinctive immune responses where, hydrocortisone exposed animals, depicted exacerbated inflammation with lower degree of infection and vice-versa for the cyclophosphamide exposed group. The innate immune system, which also plays a major role in the eradication of *A. fumigatus* conidia, was found to be functional in hydrocortisone group, triggering an acute inflammation in the pulmonary region (204). This leads to the recruitment of phagocytes towards the site of inflammation as shown by ^{19}F MR images on day 2 and day 3.

Less pronounced inflammation in cyclophosphamide group indicated the malfunctioning of innate immune cells resulting in elevated fungal invasion in the lungs. Quantification of lung image intensities from the ^{1}H MR images acquired for different mouse groups also indicated a strong lesion development in the lungs of cyclophosphamide-treated animals, 2 and 3 days after infection. Poelmans *et al*. also reported similar pattern, where significantly high MR signal intensities from *A. fumigatus* lesion were shown in mice treated with cyclophosphamide (215). Independent of the labeled immune cells extravasating in the inflamed tissue, other mechanisms like transcytosis or passive leakage of these nanoparticles can still happen. Therefore, it is important to confirm the findings using ex vivo imaging of organs/ histology. Here, we confirmed our *in vivo* imaging findings with the help of *ex vivo* fluorescence imaging, histology and

immunohistochemistry. We observed heavy influx of immune cells in the hydrocortisone-treated group leading to excessive tissue damage with less invasion of *A. fumigatus* in contrast to the cyclophosphamide-treated group.

As discussed by Temme *et al.* apart from the tissue resident macrophages, other immune cells like monocytes, dendritic cells etc. also take up nanoparticles (186). Interestingly, we also found identical pattern where dendritic cells were found in the cervical lymph node region of hydrocortisone-treated animals on day 3 post infection when compared to cyclophosphamide-treated animals. Fluorescence imaging and immune-histochemical staining, also confirm the presence of ZPFCE-NPs labeled cell in cervical lymph nodes of hydrocortisone-treated animals. The imaging platform we established for the assessment of intricate immune profile can further improve our knowledge on the host-pathogen interactions in healthy and immunosuppressed murine models with and without therapeutic intervention. Using ^{19}F MRI and newly synthesized ZPFCE-NPs, we demonstrated the difference in the immune reaction against an *A. fumigatus* challenge between two clinically relevant immunocompromised mouse groups in a longitudinal *in vivo* follow up study. In future, our imaging platform will not only aid in the evaluation of novel antifungal drugs in patients but also will advance our knowledge regarding the *in vivo* follow-up of immune cell therapies using ^{19}F MRI.

In vivo imaging of tumor-specific T cells attracted interest for the development of potential T cell-based therapeutic strategies against cancer (352, 353). T cells are also key players in most autoimmune disorders and are of high interest for gaining insights and deeper understanding of autoimmunity. T1D is an autoimmune diseases with an early onset, studied widely due to the increasing number of cases every year (354, 355). Self-reactive T cells play a major role in the pathogenesis of this disorder by infiltrating the pancreatic islets together with macrophages. This results in destruction of insulin producing beta cells, which ultimately increases the glucose level in the blood. Inflammation is an indication for the onset of T1D in the pancreas. This illustrates the need for studying inflammatory processes longitudinally from a pre-symptomatic stage through the progression of T1D. As mentioned previously (Chapter 1), labeling of phagocytic immune cells is widely described approach with a high success rate due to the phagocytic/endocytic properties of the cells. However, labeling and *in vivo* tracking of non-

phagocytic cells like T cells is challenging requiring optimized methods to facilitate the uptake of contrast agents. In this context, chemical techniques like transfection have been used for the labeling of T cells. Srinivas *et al*., demonstrated successful labeling of T cells using PFPE nanoparticles using transfecting agents (196). However, the use of transfection agents can hamper the normal physiological function of T cells.

Therefore, our second goal was to label and monitor autoreactive T cells without using transfection agents, in post adoptive transfer in a type -1 diabetes mouse model (Chapter 4). In order to label T cells, we performed lipid modification of PFCE nanoparticles to synthesis PDP-PFCE NPs. Hereby, we aimed to facilitate a stable coupling of the T cell membrane with the nanoparticles. Activated T cells showed high *in vitro* coupling with PDP-PFCE NPs at concentrations of 20mM. Based on *in vitro* data, labeling efficiency was observed to be $7x10^{12}$ fluorine atoms per T cell, which was comparable to the T cell labeling achieved by using transfection agents (283, 356). Our phantom experiments also indicated the feasibility of PDP-PFCE NPs to track labeled T cells by *in vivo* ^{19}F MRI for cell densities of approximately 1000/voxel.

However, the *in vivo* ^{19}F MRI signal intensity after adoptive transfer of different amounts of PDP-PFCE NP labeled T cells in T1D mice appeared elusive. While, all transplanted mice developed T1D based on the increased blood glucose level, indicating that engrafted T cells were viable and fully functional, local PDP-PFCE label was insufficient for *in vivo* detection by ^{19}F MRI. In order to fully understand the reason behind the non-detectability of T cells in mice, we performed additional *in vitro* experiment where with the help of flow cytometry we observed rapid dilution of our PDP-PFCE label due to T cell proliferation. These findings show that despite of sufficient T cell labeling for up to 48h, number of locally accumulated T cells and the nanoparticles/cell were not enough for the *in vivo* detection of T cell accumulation in the pancreas using ^{19}F MRI. We determined a detectability threshold based on our phantom experiments, which was ~10^{16} fluorine atoms/voxel and was sufficient for the generation of detectable fluorine signal in animal models with relatively higher recruitment of immune cells at the site of inflammation (188).

Other research groups found limitations for *in vivo* tracking of labeled T cells in tumor models using ^{19}F MRI with no success (283). So far, only transfection agents were described to label T cells for successful *in vivo* detection (182). However, these chemicals are not approved for clinical

use, limiting their application to preclinical studies. Considering the limitations of ^{19}F MRI for the *in vivo* detection of PDP-PFCE NP labeled T cells, there is room for improvement for successful *in vivo* ^{19}F MRI-based cell imaging applications. These improvements should be able to overcome the cell proliferation related label dilution. For example, the use of terminally proliferated or increased concentration of T cells for the adoptive transfer in animal models could overcome limitations in preclinical research. However, these methods could lead to potential issues related to ethics and to disease models that do not represent a clinical situation. As for the induction of T1D, it is important to use proliferating T cells. Apart from these biological advancements, technical aspects also need to be considered. Such technical improvements include the development of fluorine contrast agents with heavy payload of fluorine atoms to compensate for the dilution of label upon cell division. Potential use of highly sensitive cryogen-cooled ^{19}F MR coils in combination with advanced image processing strategies like compressed-sensing could further improve the *in vivo* tracking of non-phagocytic T cells using ^{19}F MRI (293, 294).

Being professional antigen presenting cells, dendritic cells are also crucial in the initiation and progression of T1D. We therefore, studied the migration of these cells towards pancreas in a T1D mouse model after labeling DCs *in vitro* with a fluorinated contrast agent (Chapter 5). As a mediator between innate and adaptive immunity, DCs residing in the pancreas present beta cell-derived antigens to naïve islet-specific CD4+ and CD8+ T cells in the draining lymph nodes. In our study, we aim to label NOD-derived DCs with Zonyl PFCE-NPs for the visualization and quantification of DCs with and without STZ-induced mild pancreatic stress using *in vivo* ^{19}F MRI.

These innate immune cells are of high interest not only for studying mechanisms of autoimmune disorders but also as DC vaccines against cancer like melanoma (357). They have also been studied for the same at the clinical setting using ^{19}F MRI (198, 269, 358). MRI is used for tracking the homing of DCs to lymph nodes upon labeling with SPIO particles (151, 333). This approach has also been used clinically for the follow up of cancer treatment like melanoma patients (334). Other imaging modalities like optical imaging, PET and CT have also been used to study the migratory profile of DCs towards nearby lymph nodes (359, 360). Fluorine MR imaging however, offers higher specificity and direct quantification of labeled DCs *in vivo* after transplantation of labelled cells both in mice and in humans (184, 269).

In our study, we used highly stable ZPFCE-NPs with a relatively small hydrodynamic diameter for increased cellular uptake. By triggering pancreatic stress by STZ administration, we followed the migratory pattern of labeled bone marrow-derived DCs (BMDCs) primed with beta cell-specific antigen. Our ^{19}F MRI data indicated increased homing of activated ZPFCE-NP labeled BMDCs towards the pancreatic region. The quantification of fluorine atoms from the pancreatic region indicated differences between the total fluorine content accumulated in STZ- and vehicle-treated mice. The ZPFCE-NP labeled BMDCs also migrated to nearby pancreatic lymph nodes. Uptake in the liver was also detectable by ^{19}F MRI, but was relatively low compared to the pancreas. No significant differences were observed in the pancreatic region of the STZ- and vehicle-treated mice after 24h and 48h as reported by flow cytometry. However, pancreatic lymph nodes of the vehicle-treated group showed significantly increased numbers of ZPFCE-NP-labeled BMDCs compared to STZ- treated animals 48h after transplantation. These investigations suggests that most of the labeled BMDCs migrated to the pancreatic region because of pancreatic inflammation, reducing their availability for draining pancreatic lymph nodes. In the future, our imaging platform will aid in the labeling and longitudinal *in vivo* tracking of tolerogenic DCs for the treatment of autoimmunity.

In summary, this research showed the potential and limitations of ^{19}F MR imaging for the labeling of immune cells and their *in vivo* tracking in different disease models in mice. With clinically safe contrast agents like PFC-based fluorinated nanoparticles, ^{19}F MRI not only proved to be a powerful imaging modality for numerous preclinical studies but also showed it's potential for translation to humans. For cell imaging, ^{19}F MRI offers many applications, mostly for the follow-up of phagocytic cells with less success in the tracking of non-phagocytic cells due to the sensitivity issues of ^{19}F MRI. As a result, this emerging technology requires further improvements through multiple channels, like more sensitive imaging hardware, more rapid MR sequences, improved image processing and analysis tools or more sensitive, biocompatible contrast agents.

We hope that in the near future, multidisciplinary scientific collaborations from experts of biology, physics, chemistry and medical doctors will boost the advancement of this field to overcome the existing issues with ^{19}F MRI.

References

1. Jeong HJ, Lee BC, Ahn BC, Kang KW. 2016. Development of Drugs and Technology for Radiation Theragnosis. Nucl Eng Technol.
2. Aarntzen EHJG, Srinivas M, Radu CG, Punt CJA, Boerman OC, Figdor CG, Oyen WJG, De Vries IJM. 2013. In vivo imaging of therapy-induced anti-cancer immune responses in humans. Cell Mol Life Sci.
3. Lee HW, Gangadaran P, Kalimuthu S, Ahn BC. 2016. Advances in Molecular Imaging Strategies for in Vivo Tracking of Immune Cells. Biomed Res Int.
4. Seth A, Park HS, Hong KS. 2017. Current perspective on in vivo molecular imaging of immune cells. Molecules.
5. Rudin M, Weissleder R. 2003. Molecular imaging in drug discovery and development. Nat Rev Drug Discov.
6. Kelkar SS, Reineke TM. 2011. Theranostics: Combining imaging and therapy. Bioconjug Chem.
7. Pysz MA, Gambhir SS, Willmann JK. 2010. Molecular imaging: current status and emerging strategies. Clin Radiol.
8. Park SM, Aalipour A, Vermesh O, Yu JH, Gambhir SS. 2017. Towards clinically translatable in vivo nanodiagnostics. Nat Rev Mater.
9. Hammoud DA. 2016. Molecular Imaging of Inflammation: Current Status. J Nucl Med.
10. Kumita S, Kobayashi Y, Kiriyama T, Tomiyama T, Hayash H, Ishihara K. 2013. Molecular imaging in atherosclerosis. Japanese J Clin Radiol.
11. Wu C, Li F, Niu G, Chen X. 2013. PET imaging of inflammation biomarkers. Theranostics.
12. Gounis MJ, Van Der Marel K, Marosfoi M, Mazzanti ML, Clarençon F, Chueh JY, Puri AS, Bogdanov AA. 2015. Imaging inflammation in cerebrovascular disease. Stroke.
13. Briley-Saebo KC, Amirbekian V, Vucic E, Mani V, Fisher EA, Aguinaldo JGS, Amirbekian S, Frias JC, Hyafil F, Weinreb DB, Lipinski MJ, Fayad ZA. 2007. Detecting and assessing macrophages in vivo to evaluate atherosclerosis noninvasively using molecular MRI . Proc Natl Acad Sci.
14. Daldrup-Link HE, Golovko D, Ruffell B, DeNardo DG, Castaneda R, Ansari C, Rao J, Tikhomirov GA, Wendland MF, Corot C, Coussens LM. 2011. MRI of tumor-associated macrophages with clinically applicable iron oxide nanoparticles. Clin Cancer Res.
15. Wiart M, Davoust N, Pialat JB, Desestret V, Moucharaffie S, Cho TH, Mutin M, Langlois JB, Beuf O, Honnorat J, Nighoghossian N, Berthezène Y. 2007. MRI monitoring of neuroinflammation in mouse focal ischemia. Stroke.
16. Venneti S, Lopresti BJ, Wiley CA. 2013. Molecular imaging of microglia/macrophages in the brain. Glia.
17. Van Der Laken CJ, Elzinga EH, Kropholler MA, Molthoff CFM, Van Der Heijden JW,

Maruyama K, Boellaard R, Dijkmans BAC, Lammertsma AA, Voskuyl AE. 2008. Noninvasive imaging of macrophages in rheumatoid synovitis using 11C-(R)-PK11195 and positron emission tomography. Arthritis Rheum.

18. Nahrendorf M, Zhang H, Hembrador S, Panizzi P, Sosnovik DE, Aikawa E, Libby P, Swirski FK, Weissleder R. 2008. Nanoparticle PET-CT imaging of macrophages in inflammatory atherosclerosis. Circulation.
19. Signore A, Mather SJ, Piaggio G, Malviya G, Dierckx RA. 2010. Molecular imaging of inflammation/infection: Nuclear medicine and optical imaging agents and methods. Chem Rev.
20. Yatim KM, Lakkis FG. 2015. A brief journey through the immune system. Clin J Am Soc Nephrol.
21. Janeway CA, Medzhitov R. 2002. Innate Immune Recognition. Annu Rev Immunol.
22. Burke B, Sumner S, Maitland N, Lewis CE. 2002. Macrophages in gene therapy: cellular delivery vehicles and in vivo targets. J Leukoc Biol.
23. Aderem A, Underhill DM. 2002. MECHANISMS OF PHAGOCYTOSIS IN MACROPHAGES. Annu Rev Immunol.
24. Davies LC, Jenkins SJ, Allen JE, Taylor PR. 2013. Tissue-resident macrophages. Nat Immunol.
25. Bowdish DME. 2016. Macrophage Activation and PolarizationEncyclopedia of Immunobiology.
26. Chawla A. 2010. Control of macrophage activation and function by PPARs. Circ Res.
27. Murray PJ, Wynn TA. 2011. Protective and pathogenic functions of macrophage subsets. Nat Rev Immunol.
28. Li Y, Liu TM. 2018. Discovering macrophage functions using in Vivo optical imaging techniques. Front Immunol.
29. Germain RN. 2002. t-cell development and the CD4-CD8 lineage decision. Nat Rev Immunol.
30. Swain SL, Bradley LM, Croft M, Tonkonogy S, Atkins G, Weinberg AD, Duncan DD, Hedrick SM, Dutton RW, Huston G. 1991. Helper T-Cell Subsets: Phenotype, Function and the Role of Lymphokines in Regulating their Development. Immunol Rev.
31. Luckheeram RV, Zhou R, Verma AD, Xia B. 2012. CD4 + T Cells: Differentiation and Functions . Clin Dev Immunol.
32. Trapani JA, Smyth MJ. 2002. Functional significance of the perforin/granzyme cell death pathway. Nat Rev Immunol.
33. Zhang N, Bevan MJ. 2011. CD8+ T Cells: Foot Soldiers of the Immune System. Immunity.
34. Shu CJ, Radu CG, Shelly SM, Vo DD, Prins R, Ribas A, Phelps ME, Witte ON. 2009. Quantitative PET reporter gene imaging of CD8+ T cells specific for a melanoma-expressed self-antigen. Int Immunol.
35. Liu L, Ye Q, Wu Y, Hsieh WY, Chen CL, Shen HH, Wang SJ, Zhang H, Hitchens TK, Ho C.

2012. Tracking T-cells in vivo with a new nano-sized MRI contrast agent. Nanomedicine Nanotechnology, Biol Med.

36. Voisine C, Trinité B, Josien R. 2002. Dendritic cells. Rev Fr des Lab.
37. Steinman RM, Inaba K, Turley S, Pierre P, Mellman I. 1999. Antigen capture, processing, and presentation by dendritic cells: Recent cell biological studies. Hum Immunol.
38. Cella M, Sallusto F, Lanzavecchia A. 1997. Origin, maturation and antigen presenting function of dendritic cells. Curr Opin Immunol.
39. Steinman RM. 1991. The dendritic cell system and its role in immunogenicity. Annu Rev Immunol.
40. Sabado RL, Balan S, Bhardwaj N. 2017. Dendritic cell-based immunotherapy. Cell Res.
41. Nencioni A, Grünebach F, Schmidt SM, Müller MR, Boy D, Patrone F, Ballestrero A, Brossart P. 2008. The use of dendritic cells in cancer immunotherapy. Crit Rev Oncol Hematol.
42. Palucka K, Banchereau J, Mellman I. 2010. Designing vaccines based on biology of human dendritic cell subsets. Immunity.
43. Vivier E, Tomasello E, Baratin M, Walzer T, Ugolini S. 2008. Functions of natural killer cells. Nat Immunol.
44. Brittenden J, Heys SD, Ross J, Eremin O. 1996. Natural killer cells and cancer. Cancer.
45. Brownell AL, Jain RK, Shoup TM, Brownell GL. 1993. Imaging of Activated Natural Killer Cells in Mice by Positron Emission Tomography: Preferential Uptake in Tumors. Cancer Res.
46. Meier R, Piert M, Piontek G, Rudelius M, Oostendorp RA, Senekowitsch-Schmidtke R, Henning TD, Wels WS, Uherek C, Rummeny EJ, Daldrup-Link HE. 2008. Tracking of [18F]FDG-labeled natural killer cells to HER2/neu-positive tumors. Nucl Med Biol.
47. Edinger M, Cao YA, Verneris MR, Bachmann MH, Contag CH, Negrin RS. 2003. Revealing lymphoma growth and the efficacy of immune cell therapies using in vivo bioluminescence imaging. Blood.
48. Tavri S, Jha P, Meier R, Henning TD, Müller T, Hostetter D, Knopp C, Johansson M, Reinhart V, Boddington S, Sista A, Wels WS, Daldrup-Link HE. 2018. Optical Imaging of Cellular Immunotherapy against Prostate Cancer. Mol Imaging.
49. Maglione PJ, Chan J. 2009. How B cells shape the immune response against Mycobacterium tuberculosis. Eur J Immunol.
50. Dunkelberger JR, Song WC. 2010. Complement and its role in innate and adaptive immune responses. Cell Res.
51. Walther M, Gebhardt P, Grosse-Gehling P, Würbach L, Irmler I, Preusche S, Khalid M, Opfermann T, Kamradt T, Steinbach J, Saluz HP. 2011. Implementation of 89 Zr production and in vivo imaging of B-cells in mice with 89 Zr-labeled anti-B-cell antibodies by small animal PET/CT. Appl Radiat Isot.
52. Thorek DLJ, Tsao PY, Arora V, Zhou L, Eisenberg RA, Tsourkas A. 2010. In vivo, multimodal imaging of B cell distribution and response to antibody immunotherapy in

mice. PLoS One.

53. Tanaka A, Sakaguchi S. 2017. Regulatory T cells in cancer immunotherapy. Cell Res.

54. Radford KJ, Tullett KM, Lahoud MH. 2014. Dendritic cells and cancer immunotherapy. Curr Opin Immunol.

55. Hinz T, Buchholz CJ, Van Der Stappen T, Cichutek K, Kalinke U. 2006. Manufacturing and quality control of cell-based tumor vaccines: A scientific and a regulatory perspective. J Immunother.

56. Sadelain M, Rivière I, Riddell S. 2017. Therapeutic T cell engineering. Nature.

57. Maude SL, Barrett D, Teachey DT, Grupp SA. 2014. Managing cytokine release syndrome associated with novel T cell-engaging therapies. Cancer J (United States).

58. Milone MC, Bhoj VG. 2018. The Pharmacology of T Cell Therapies. Mol Ther - Methods Clin Dev.

59. Kumar A, Herbein G. 2014. The macrophage: a therapeutic target in HIV-1 infection. Mol Cell Ther.

60. De Palma M, Lewis CE. 2013. Macrophage regulation of tumor responses to anticancer therapies. Cancer Cell.

61. Cahalan MD, Parker I, Wei SH, Miller MJ. 2002. Two-photon tissue imaging: Seeing the immune system in a fresh light. Nat Rev Immunol.

62. Sivasubramanian M, Hsia Y, Lo L-W. 2014. Nanoparticle-facilitated functional and molecular imaging for the early detection of cancer. Front Mol Biosci.

63. Ravanetti F, Vos W, Ruscitti F, Stellari FF, Villetti G, Cacchioli A, Essers J, Ridwan Y, Donofrio G, van Heijningen P. 2018. A Multimodal Imaging Approach Based on Micro-CT and Fluorescence Molecular Tomography for Longitudinal Assessment of Bleomycin-Induced Lung Fibrosis in Mice. J Vis Exp.

64. Gallastegui A, Cheung J, Southard T, Hume KR. 2018. Volumetric and linear measurements of lung tumor burden from non-gated micro-CT imaging correlate with histological analysis in a genetically engineered mouse model of non-small cell lung cancer. Lab Anim.

65. Bell RD, Rudmann C, Wood RW, Schwarz EM, Rahimi H. 2018. Longitudinal micro-CT as an outcome measure of interstitial lung disease in TNF-transgenic mice. PLoS One.

66. Rodt T, von Falck C, Dettmer S, Halter R, Maus R, Ask K, Kolb M, Gauldie J, Länger F, Hoy L, Welte T, Galanski M, Maus UA, Borlak J. 2010. Micro-computed tomography of pulmonary fibrosis in mice induced by adenoviral gene transfer of biologically active transforming growth factor-β1. Respir Res.

67. Li M, Jirapatnakul A, Biancardi A, Riccio ML, Weiss RS, Reeves AP. 2013. Growth pattern analysis of murine lung neoplasms by advanced semi-automated quantification of micro-CT images. PLoS One.

68. Døhn UM, Ejbjerg BJ, Hasselquist M, Narvestad E, Møller J, Thomsen HS, Østergaard M. 2008. Detection of bone erosions in rheumatoid arthritis wrist joints with magnetic resonance imaging, computed tomography and radiography. Arthritis Res Ther.

69. Tomlinson JE, Redding WR, Berry C, Smallwood JE. 2003. Computed tomographic anatomy of the equine tarsus. Vet Radiol Ultrasound.

70. Gilula LA. 2013. Wrist and handMusculoskeletal Diseases 2013-2016: Diagnostic Imaging and Interventional Techniques.

71. Chhour P, Kim J, Benardo B, Tovar A, Mian S, Litt HI, Ferrari VA, Cormode DP. 2017. Effect of gold nanoparticle size and coating on labeling monocytes for CT tracking. Bioconjug Chem.

72. Zhang XD, Wu HY, Wu D, Wang YY, Chang JH, Zhai Z Bin, Meng AM, Liu PX, Zhang LA, Fan FY. 2010. Toxicologic effects of gold nanoparticles in vivo by different administration routes. Int J Nanomedicine.

73. Cho WS, Cho M, Jeong J, Choi M, Cho HY, Han BS, Kim SH, Kim HO, Lim YT, Chung BH, Jeong J. 2009. Acute toxicity and pharmacokinetics of 13 nm-sized PEG-coated gold nanoparticles. Toxicol Appl Pharmacol.

74. Jia YP, Ma BY, Wei XW, Qian ZY. 2017. The in vitro and in vivo toxicity of gold nanoparticles. Chinese Chem Lett.

75. Deshpande N, Lutz AM, Ren Y, Foygel K, Tian L, Schneider M, Pai R, Pasricha PJ, Willmann JK. 2012. Quantification and Monitoring of Inflammation in Murine Inflammatory Bowel Disease with Targeted Contrast-enhanced US. Radiology.

76. Lindner JR. 2009. Molecular imaging of cardiovascular disease with contrast-enhanced ultrasonography. Nat Rev Cardiol.

77. Marshall D, Pedley RB, Boden JA, Boden R, Melton RG, Begent RHJ. 1996. Polyethylene glycol modification of a galactosylated streptavidin clearing agent: Effects on immunogenicity and clearance of a biotinylated anti-tumour antibody. Br J Cancer.

78. Quaia E. 2007. Microbubble ultrasound contrast agents: An update. Eur Radiol.

79. De Cock I, Zagato E, Braeckmans K, Luan Y, de Jong N, De Smedt SC, Lentacker I. 2015. Ultrasound and microbubble mediated drug delivery: acoustic pressure as determinant for uptake via membrane pores or endocytosis. J Control Release.

80. Geers B, De Wever O, Demeester J, Bracke M, De Smedt SC, Lentacker I. 2013. Targeted liposome-loaded microbubbles for cell-specific ultrasound-triggered drug delivery. Small.

81. Biqin D, Sun C, Zhang HF. 2017. Optical Detection of Ultrasound in Photoacoustic Imaging. IEEE Trans Biomed Eng.

82. Sadikot RT, Blackwell TS. 2005. Bioluminescence imaging. Proc Am Thorac Soc.

83. Chamma E, Daradich A, Côté D, Yun SH. 2014. Intravital MicroscopyPathobiology of Human Disease: A Dynamic Encyclopedia of Disease Mechanisms.

84. Tsang SH, Sharma T. 2018. Optical coherence tomographyAdvances in Experimental Medicine and Biology.

85. Siraj N, El-Zahab B, Hamdan S, Karam TE, Haber LH, Li M, Fakayode SO, Das S, Valle B, Strongin RM, Patonay G, Sintim HO, Baker GA, Powe A, Lowry M, Karolin JO, Geddes CD, Warner IM. 2016. Fluorescence, Phosphorescence, and Chemiluminescence. Anal Chem.

86. Keyaerts M, Caveliers V, Lahoutte T. 2012. Bioluminescence imaging: Looking beyond

the light. Trends Mol Med.

87. de Almeida PE, van Rappard JRM, Wu JC. 2011. In vivo bioluminescence for tracking cell fate and function. Am J Physiol Circ Physiol.

88. Feng G, Mellor RH, Bernstein M, Keller-Peck C, Nguyen QT, Wallace M, Nerbonne JM, Lichtman JW, Sanes JR. 2000. Imaging neuronal subsets in transgenic mice expressing multiple spectral variants of GFP. Neuron.

89. Ntziachristos V. 2006. FLUORESCENCE MOLECULAR IMAGING. Annu Rev Biomed Eng.

90. Merchant FA, Periasamy A. 2007. Fluorescence ImagingMicroscope Image Processing.

91. Martelli C, Dico A Lo, Diceglie C, Lucignani G, Ottobrini L. 2016. Optical imaging probes in oncology. Oncotarget.

92. Frangioni J V. 2003. In vivo near-infrared fluorescence imaging. Curr Opin Chem Biol.

93. Luo S, Zhang E, Su Y, Cheng T, Shi C. 2011. A review of NIR dyes in cancer targeting and imaging. Biomaterials.

94. Tavri S, Jha P, Meier R, Henning TD, Mueller T, Hostetter D, Knopp C, Johansson M, Reinhart V, Boddington S, Sista A, Wels WS, Daldrup-Link HE. 2009. Optical Imaging of Cellular Immunotherapy against Prostate Cancer. Mol Imaging.

95. Youniss FM, Sundaresan G, Graham LJ, Wang L, Berry CR, Dewkar GK, Jose P, Bear HD, Zweit J. 2014. Near-infrared imaging of adoptive immune cell therapy in breast cancer model using cell membrane labeling. PLoS One.

96. Staderini M, Martín MA, Bolognesi ML, Menéndez JC. 2015. Imaging of β-amyloid plaques by near infrared fluorescent tracers: A new frontier for chemical neuroscience. Chem Soc Rev.

97. Sakudo A. 2016. Near-infrared spectroscopy for medical applications: Current status and future perspectives. Clin Chim Acta.

98. Sharma P, Brown S, Walter G, Santra S, Moudgil B. 2006. Nanoparticles for bioimaging. Adv Colloid Interface Sci.

99. Clift MJD, Brandenberger C, Rothen-Rutishauser B, Brown DM, Stone V. 2011. The uptake and intracellular fate of a series of different surface coated quantum dots in vitro. Toxicology.

100. Bottrill M, Green M. 2011. Some aspects of quantum dot toxicity. Chem Commun.

101. Keyaerts M, Caveliers V, Lahoutte T. 2014. Bioluminescence ImagingComprehensive Biomedical Physics.

102. Marques SM, Esteves Da Silva JCG. 2009. Firefly bioluminescence: A mechanistic approach of luciferase catalyzed reactions. IUBMB Life.

103. Hastings JW. 1996. Chemistries and colors of bioluminescent reactions: A reviewGene.

104. Kim JE, Kalimuthu S, Ahn BC. 2015. In Vivo Cell Tracking with Bioluminescence Imaging. Nucl Med Mol Imaging (2010).

105. Welsh DK, Noguchi T. 2012. Cellular bioluminescence imaging. Cold Spring Harb Protoc.

106. Byrne FL, McCarroll JA, Kavallaris M. 2016. Analyses of tumor burden in vivo and

metastasis ex vivo using luciferase-expressing cancer cells in an orthotopic mouse model of neuroblastomaMethods in Molecular Biology.

107. Jenkins DE, Hornig YS, Oei Y, Dusich J, Purchio T. 2005. Bioluminescent human breast cancer cell lines that permit rapid and sensitive in vivo detection of mammary tumors and multiple metastases in immune deficient mice. Breast Cancer Res.

108. Close DM, Xu T, Sayler GS, Ripp S. 2011. In vivo bioluminescent imaging (BLI): Noninvasive visualization and interrogation of biological processes in living animals. Sensors.

109. Luker KE, Smith MCP, Luker GD, Gammon ST, Piwnica-Worms H, Piwnica-Worms D. 2004. Kinetics of regulated protein-protein interactions revealed with firefly luciferase complementation imaging in cells and living animals. Proc Natl Acad Sci.

110. Zhang X, Edwards JP, Mosser DM. 2009. The expression of exogenous genes in macrophages: Obstacles and opportunities. Methods Mol Biol.

111. Zhu A, Marcus DM, Shu H-KG, Shim H. 2012. Application of Metabolic PET Imaging in Radiation Oncology. Radiat Res.

112. Kumar R, Basu S, Torigian D, Anand V, Zhuang H, Alavi A. 2008. Role of modern imaging techniques for diagnosis of infection in the era of 18F-fluorodeoxyglucose positron emission tomography. Clin Microbiol Rev.

113. Sharma P, Mukherjee A, Karunanithi S, Bal C, Kumar R. 2014. Potential role of18F-FDG PET/CT in patients with fungal infections. Am J Roentgenol.

114. Veeramachaneni R, Gulick J, Halldorsson AO, Van TT, Zhang PL, Herrera GA. 2001. Benign myoepithelioma of the lung: A case report and review of the literature. Arch Pathol Lab Med 125:1494–1496.

115. Hot A, Maunoury C, Poiree S, Lanternier F, Viard JP, Loulergue P, Coignard H, Bougnoux ME, Suarez F, Rubio MT, Mahlaoui N, Dupont B, Lecuit M, Faraggi M, Lortholary O. 2011. Diagnostic contribution of positron emission tomography with [18F]fluorodeoxyglucose for invasive fungal infections. Clin Microbiol Infect.

116. Yaghoubi SS, Jensen MC, Satyamurthy N, Budhiraja S, Paik D, Czernin J, Gambhir SS. 2009. Noninvasive detection of therapeutic cytolytic T cells with 18 F-FHBG PET in a patient with glioma. Nat Clin Pract Oncol.

117. Peñuelas I, Haberkorn U, Yaghoubi S, Gambhir SS. 2005. Gene therapy imaging in patients for oncological applications. Eur J Nucl Med Mol Imaging.

118. Peñuelas I, Mazzolini G, Boán JF, Sangro B, Martí-Climent J, Ruiz M, Ruiz J, Satyamurthy N, Qian C, Barrio JR, Phelps ME, Richter JA, Gambhir SS, Prieto J. 2005. Positron emission tomography imaging of adenoviral-mediated transgene expression in liver cancer patients. Gastroenterology.

119. Herschman HR. 2004. PET reporter genes for noninvasive imaging of gene therapy, cell tracking and transgenic analysis. Crit Rev Oncol Hematol.

120. Gambhir SS, Yaghoubi SS. 2010. Molecular imaging with reporter genesMolecular Imaging with Reporter Genes.

121. Yaghoubi SS, Campbell DO, Radu CG, Czernin J. 2012. Positron emission tomography reporter genes and reporter probes: Gene and cell therapy applications. Theranostics.

122. Gregory Ashby F. 2015. An introduction to fMRIAn Introduction to Model-Based Cognitive Neuroscience.

123. Sujlana P, Skrok J, Fayad LM. 2018. Review of dynamic contrast-enhanced MRI: Technical aspects and applications in the musculoskeletal system. J Magn Reson Imaging.

124. Huber L, Uludağ K, Möller HE. 2017. Non-BOLD contrast for laminar fMRI in humans: CBF, CBV, and CMRO2. Neuroimage.

125. Warbrick T, Rosenberg J, Shah NJ. 2017. The relationship between BOLD fMRI response and the underlying white matter as measured by fractional anisotropy (FA): A systematic review. Neuroimage.

126. Anzidei M, Menichini G, Catalano C. 2013. Mr-angiographyCardiovascular Ct and Mr Imaging: From Technique to Clinical Interpretation.

127. de Figueiredo EHMSG, Borgonovi AFNG, Doring TM. 2011. Basic concepts of mr imaging, diffusion mr imaging, and diffusion tensor imaging. Magn Reson Imaging Clin N Am.

128. Purcell EM, Torrey HC, Pound R V. 1946. Resonance absorption by nuclear magnetic moments in a solid [7]. Phys Rev.

129. Xiao YD, Paudel R, Liu J, Ma C, Zhang ZS, Zhou SK. 2016. MRI contrast agents: Classification and application (Review). Int J Mol Med.

130. Becker ED. 2007. Pulse SequencesHigh Resolution NMR.

131. Bitar R, Leung G, Perng R, Tadros S, Moody AR, Sarrazin J, McGregor C, Christakis M, Symons S, Nelson A, Roberts TP. 2006. MR Pulse Sequences: What Every Radiologist Wants to Know but Is Afraid to Ask. RadioGraphics.

132. Shokrollahi H. 2013. Structure, synthetic methods, magnetic properties and biomedical applications of ferrofluids. Mater Sci Eng C.

133. Ali A, Zafar H, Zia M, ul Haq I, Phull AR, Ali JS, Hussain A. 2016. Synthesis, characterization, applications, and challenges of iron oxide nanoparticles. Nanotechnol Sci Appl.

134. Di Marco M, Sadun C, Port M, Guilbert I, Couvreur P, Dubernet C. 2007. Physicochemical characterization of ultrasmall superparamagnetic iron oxide particles (USPIO) for biomedical application as MRI contrast agents. Int J Nanomedicine.

135. Bietenbeck M, Florian A, Sechtem U, Yilmaz A. 2015. The diagnostic value of iron oxide nanoparticles for imaging of myocardial inflammation - Quo vadis? J Cardiovasc Magn Reson.

136. Weinstein JS, Varallyay CG, Dosa E, Gahramanov S, Hamilton B, Rooney WD, Muldoon LL, Neuwelt EA. 2010. Superparamagnetic iron oxide nanoparticles: Diagnostic magnetic resonance imaging and potential therapeutic applications in neurooncology and central nervous system inflammatory pathologies, a review. J Cereb Blood Flow Metab.

137. Egawa EY, Kitamura N, Nakai R, Arima Y, Iwata H. 2015. A DNA hybridization system for labeling of neural stem cells with SPIO nanoparticles for MRI monitoring post-

transplantation. Biomaterials.

138. Wang L, Potter WM, Zhao Q. 2015. In vivo quantification of SPIO nanoparticles for cell labeling based on MR phase gradient images. Contrast Media Mol Imaging.

139. So PW, Kalber T, Hunt D, Farquharson M, Al-Ebraheem A, Parkes HG, Simon R, Bell JD. 2010. Efficient and rapid labeling of transplanted cell populations with superparamagnetic iron oxide nanoparticles using cell surface chemical biotinylation for in vivo monitoring by MRI. Cell Transplant.

140. Ittrich H, Peldschus K, Raabe N, Kaul M, Adam G. 2013. Superparamagnetic iron oxide nanoparticles in biomedicine: Applications and developments in diagnostics and therapy. RoFo Fortschritte auf dem Gebiet der Rontgenstrahlen und der Bildgeb Verfahren.

141. Cai QY, Lee H, Kim EJ, Moon H, Chang K, Rho J, Hong KS. 2012. Magnetic resonance imaging of superparamagnetic iron oxide-labeled macrophage infiltrates in acute-phase renal ischemia-reperfusion mouse model. Nanomedicine Nanotechnology, Biol Med.

142. Smirnov P, Lavergne E, Gazeau F, Lewin M, Boissonnas A, Doan BT, Gillet B, Combadière C, Combadière B, Clément O. 2006. In vivo cellular imaging of lymphocyte trafficking by MRI: A tumor model approach to cell-based anticancer therapy. Magn Reson Med.

143. Kircher M, Allport J, Graves E, Love V, Josephson L, Lichtman A, Weissleder R. 2003. In vivo high resolution three-dimensional imaging of antigen-specific cytotoxic T-lymphocyte trafficking to tumors. Cancer Res.

144. Yang CT, Chuang KH. 2012. Gd(iii) chelates for MRI contrast agents: From high relaxivity to “smart”, from blood pool to blood-brain barrier permeable. Medchemcomm.

145. Caschera L, Lazzara A, Piergallini L, Ricci D, Tuscano B, Vanzulli A. 2016. Contrast agents in diagnostic imaging: Present and future. Pharmacol Res.

146. Murakami T, Baron RL, Peterson MS, Oliver JH, Davis PL, Confer SR, Federle MP. 1996. Hepatocellular carcinoma: MR imaging with mangafodipir trisodium (Mn-DPDP). Radiology.

147. Inoue T, Majid T, Pautler RG. 2011. Manganese enhanced MRI (MEMRI): Neurophysiological applications. Rev Neurosci.

148. Sepúlveda MR, Dresselaers T, Vangheluwe P, Everaerts W, Himmelreich U, Mata AM, Wuytack F. 2012. Evaluation of manganese uptake and toxicity in mouse brain during continuous MnCl2 administration using osmotic pumps. Contrast Media Mol Imaging.

149. Ahrens ET, Bulte JWM. 2013. Tracking immune cells in vivo using magnetic resonance imaging. Nat Rev Immunol.

150. Lucignani G, Ottobrini L, Martelli C, Rescigno M, Clerici M. 2006. Molecular imaging of cell-mediated cancer immunotherapy. Trends Biotechnol.

151. Wu C, Xu Y, Yang L, Wu J, Zhu W, Li D, Cheng Z, Xia C, Guo Y, Gong Q, Song B, Ai H. 2015. Negatively Charged Magnetite Nanoparticle Clusters as Efficient MRI Probes for Dendritic Cell Labeling and in Vivo Tracking. Adv Funct Mater.

152. Mansfield P, Maudsley AA. 1977. Medical imaging by NMR. Br J Radiol.

153. Holland GN, Bottomley PA, Hinshaw WS. 1977. 19F magnetic resonance imaging. J Magn

Reson.

154. Ruiz-Cabello J, Barnett BP, Bottomley PA, Bulte JWM. 2011. Fluorine (19F) MRS and MRI in biomedicine. NMR Biomed.

155. Amiri H, Srinivas M, Veltien A, van Uden MJ, de Vries IJM, Heerschap A. 2015. Cell tracking using 19F magnetic resonance imaging: Technical aspects and challenges towards clinical applications. Eur Radiol 25:726–735.

156. Wolf W. 1977. A Model for Prediction of Chemotherapy Response to 5-Fluorouracil Based on the Differential Distribution of 5-[18F]Fluorouracil in Sensitive versus Resistant Lymphocytic Leukemia in Mice. Cancer Res.

157. Stevens AN, Morris PG, Iles RA, Sheldon PW, Griffiths JR. 1984. 5-Flourouracil metabolism monitored in vivo by19F NMR. Br J Cancer.

158. Hull WE, Port RE, Herrmann R, Britsch B, Kunz W. 1988. Metabolites of 5-Fluorouracil in Plasma and Urine, as Monitored by 19F Nuclear Magnetic Resonance Spectroscopy, for Patients Receiving Chemotherapy with or without Methotrexate Pretreatment. Cancer Res.

159. Diasio RB, Harris BE. 1989. Clinical Pharmacology of 5-Fluorouracil. Clin Pharmacokinet.

160. Major PP, Egan E, Herrick D, Kufe DW. 1982. 5-Fluorouracil Incorporation in DNA of Human Breast Carcinoma Cells. Cancer Res.

161. Longley DB, Harkin DP, Johnston PG. 2003. 5-Fluorouracil: Mechanisms of action and clinical strategies. Nat Rev Cancer.

162. Bartusik D, Aebisher D. 2014. 19F applications in drug development and imaging-a review. Biomed Pharmacother.

163. Kruger SJ, Nagle SK, Couch MJ, Ohno Y, Albert M, Fain SB. 2016. Functional imaging of the lungs with gas agents. J Magn Reson Imaging.

164. Fox M, Gaudet J, Foster P. 2016. Fluorine-19 MRI Contrast Agents for Cell Tracking and Lung Imaging. Magn Reson Insights 8:53.

165. Pérez-Sánchez JM, Pérez De Alejo R, Rodríguez I, Cortijo M, Peces-Barba G, Ruiz-Cabello J. 2005. In vivo diffusion weighted19F MRI using SF6. Magn Reson Med.

166. Kuethe DO, Caprihan A, Gach HM, Lowe IJ, Fukushima E. 2000. Imaging obstructed ventilation with NMR using inert fluorinated gases. J Appl Physiol.

167. Wolf U, Scholz A, Heussel CP, Markstaller K, Schreiber WG. 2006. Subsecond fluorine-19 MRI of the lung. Magn Reson Med.

168. Adolphi NL, Kuethe DO. 2008. Quantitative mapping of ventilation-perfusion ratios in lungs by19F MR imaging of T1of inert fluorinated gases. Magn Reson Med.

169. Scholz AW, Wolf U, Fabel M, Weiler N, Heussel CP, Eberle B, David M, Schreiber WG. 2009. Comparison of magnetic resonance imaging of inhaled SF6with respiratory gas analysis. Magn Reson Imaging.

170. Schreiber WG, Eberle B, Laukemper-Ostendorf S, Markstaller K, Weiler N, Scholz A, Bürger K, Heussel CP, Thelen M, Kauczor HU. 2001. Dynamic19F-MRI of pulmonary ventilation using sulfur hexafluoride (SF6) gas. Magn Reson Med.

171. Couch MJ, Ball IK, Li T, Fox MS, Littlefield SL, Biman B, Albert MS. 2013. Pulmonary Ultrashort Echo Time ^{19} F MR Imaging with Inhaled Fluorinated Gas Mixtures in Healthy Volunteers: Feasibility. Radiology.

172. Wu L, Wen X, Wang X, Wang C, Sun X, Wang K, Zhang H, Williams T, Stacy AJ, Chen J, Schmieder AH, Lanza GM, Shen B. 2018. Local intratracheal delivery of perfluorocarbon nanoparticles to lung cancer demonstrated with magnetic resonance multimodal imaging. Theranostics.

173. Simberg D, Mattrey R. 2009. Targeting of perfluorocarbon microbubbles to selective populations of circulating blood cells. J Drug Target.

174. Waxman K. 1986. Perfluorocarbons as blood substitutes. Ann Emerg Med.

175. Gomes L, Gomes ER, Gomes, Lígia; Gomes ER, Gomes L, Gomes ER. 2007. Perfluorocarbons Compounts Used as Oxygen Carriers: From Liquid Ventilation to Blood Substitutes. Rev da Fac Ciências da Saúde (Artigos em Inglês).

176. Srinivas M, Heerschap A, Ahrens ET, Figdor CG, de Vries IJM. 2010. 19F MRI for quantitative in vivo cell tracking. Trends Biotechnol 28:363–370.

177. D'Hollander A, Jans H, Velde G Vande, Verstraete C, Massa S, Devoogdt N, Stakenborg T, Muyldermans S, Lagae L, Himmelreich U. 2017. Limiting the protein corona: A successful strategy for in vivo active targeting of anti-HER2 nanobody-functionalized nanostars. Biomaterials.

178. Schmid F, Höltke C, Parker D, Faber C. 2013. Boosting 19F MRI - SNR efficient detection of paramagnetic contrast agents using ultrafast sequences. Magn Reson Med.

179. Hu L, Zhang L, Chen J, Lanza GM, Wickline SA. 2011. Diffusional mechanisms augment the fluorine MR relaxation in paramagnetic perfluorocarbon nanoparticles that provides a "relaxation switch" for detecting cellular endosomal activation. J Magn Reson Imaging.

180. de Vries A, Moonen R, Yildirim M, Langereis S, Lamerichs R, Pikkemaat JA, Baroni S, Terreno E, Nicolay K, Strijkers GJ, Grüll H. 2014. Relaxometric studies of gadolinium-functionalized perfluorocarbon nanoparticles for MR imaging. Contrast Media Mol Imaging.

181. Malaisse WJ, Zhang Y, Louchami K, Sharma S, Dresselaers T, Himmelreich U, Novotny GW, Mandrup-Poulsen T, Waschke D, Leshch Y, Thimm J, Thiem J, Sener A. 2012. 19F-heptuloses as tools for the non-invasive imaging of GLUT2-expressing cells. Arch Biochem Biophys.

182. Srinivas M, Turner MS, Janjic JM, Morel PA, Laidlaw DH, Ahrens ET. 2009. In vivo cytometry of antigen-specific T cells using19F MRI. Magn Reson Med.

183. Saini S, Korf H, Liang S, Verbeke R, Manshian B, Raemdonck K, Lentacker I, Gysemans C, De Smedt SC, Himmelreich U. 2019. Challenges for labeling and longitudinal tracking of adoptively transferred autoreactive T lymphocytes in an experimental type-1 diabetes model. Magn Reson Mater Physics, Biol Med.

184. Ahrens ET, Flores R, Xu H, Morel PA. 2005. In vivo imaging platform for tracking immunotherapeutic cells. Nat Biotechnol 23:983–987.

185. Stoll G, Basse-Lüsebrink T, Weise G, Jakob P. 2012. Visualization of inflammation using

19F-magnetic resonance imaging and perfluorocarbons. Wiley Interdiscip Rev Nanomedicine Nanobiotechnology 4:438–447.

186. Temme S, Bönner F, Schrader J, Flögel U. 2012. 19F magnetic resonance imaging of endogenous macrophages in inflammation. Wiley Interdiscip Rev Nanomedicine Nanobiotechnology 4:329–343.

187. Flogel U, Ding Z, Hardung H, Jander S, Reichmann G, Jacoby C, Schubert R, Schrader J. 2008. In vivo monitoring of inflammation after cardiac and cerebral ischemia by fluorine magnetic resonance imaging. Circulation 118:140–148.

188. Ebner B, Behm P, Jacoby C, Burghoff S, French BA, Schrader J, Flögel U. 2010. Early assessment of pulmonary inflammation by 19F MRI in vivo. Circ Cardiovasc Imaging 3:202–210.

189. Zhong J, Narsinh K, Morel PA, Xu H, Ahrens ET. 2015. In vivo quantification of inflammation in experimental autoimmune encephalomyelitis rats using fluorine-19 magnetic resonance imaging reveals immune cell recruitment outside the nervous system. PLoS One 10:1–13.

190. van Heeswijk RB, Pellegrin M, Flögel U, Gonzales C, Aubert J-F, Mazzolai L, Schwitter J, Stuber M. 2015. Fluorine MR Imaging of Inflammation in Atherosclerotic Plaque in Vivo. Radiology 275:421–429.

191. Bulte JWM. 2014. Tracking Immune Cells In Vivo Using Magnetic Resonance Imaging 13.

192. Hertlein T, Sturm V, Kircher S, Basse-Lüsebrink T, Haddad D, Ohlsen K, Jakob P. 2011. Visualization of abscess formation in a murine thigh infection model of Staphylococcus aureus by 19F-magnetic resonance imaging (MRI). PLoS One 6:e18246.

193. Jacoby C, Borg N, Heusch P, Sauter M, Bönner F, Kandolf R, Klingel K, Schrader J, Flögel U. 2014. Visualization of immune cell infiltration in experimental viral myocarditis by 19F MRI in vivo. Magn Reson Mater Physics, Biol Med 27.

194. Ahrens ET, Young W Bin, Xu H, Pusateri LK. 2011. Rapid quantification of inflammation in tissue samples using perfluorocarbon emulsion and fluorine-19 nuclear magnetic resonance. Biotechniques.

195. Kadayakkara DK, Ranganathan S, Young W Bin, Ahrens ET. 2012. Assaying macrophage activity in a murine model of inflammatory bowel disease using fluorine-19 MRI. Lab Investig.

196. Srinivas M, Morel PA, Ernst LA, Laidlaw DH, Ahrens ET. 2007. Fluorine-19 MRI for visualization and quantification of cell migration in a diabetes model. Magn Reson Med 58:725–734.

197. Helfer BM, Balducci A, Nelson AD, Janjic JM, Gil RR, Kalinski P, De Vries IJM, Ahrens ET, Mailliard RB. 2010. Functional assessment of human dendritic cells labeled for in vivo 19F magnetic resonance imaging cell tracking. Cytotherapy.

198. Ahrens ET, Helfer BM, O'Hanlon CF, Schirda C. 2014. Clinical cell therapy imaging using a perfluorocarbon tracer and fluorine-19 MRI. Magn Reson Med 72:1696–1701.

199. Guidry J, Kollipara R, Downing C, Lee M, Tyring SK. 2017. Fungal infectionsClinical and Basic Immunodermatology: Second Edition.

200. Latgé JP. 1999. Aspergillus fumigatus and Aspergillosis. Clin Microbiol Rev.

201. Mccormick A, Loeffler J, Ebel F. 2010. Aspergillus fumigatus: Contours of an opportunistic human pathogen. Cell Microbiol.

202. Dagenais TRT, Keller NP. 2009. Pathogenesis of Aspergillus fumigatus in Invasive Aspergillosis. Clin Microbiol Rev 22:447–465.

203. Curi ALL, Benchimol EI, Vasconcelos-Santos DV. 2016. AspergillosisIntraocular Inflammation.

204. Kalleda N, Amich J, Arslan B, Poreddy S, Mattenheimer K, Mokhtari Z, Einsele H, Brock M, Heinze KG, Beilhack A. 2016. Dynamic immune cell recruitment after murine pulmonary Aspergillus fumigatus infection under different immunosuppressive regimens. Front Microbiol 7:1–15.

205. Dagenais TRT, Keller NP. 2009. Pathogenesis of Aspergillus fumigatus in Invasive Aspergillosis. Clin Microbiol Rev 22:447–465.

206. Lionakis MS, Kontoyiannis DP. 2003. Glucocorticoids and invasive fungal infections. Lancet 362:1828–1838.

207. Hohl TM. 2017. Immune responses to invasive aspergillosis. Curr Opin Infect Dis 30:364–371.

208. Sales-campos H, Tonani L, Regina M, Kress VZ. 2013. The Immune Interplay between the Host and the Pathogen in Aspergillus fumigatus Lung Infection 2 . Aspergillus fumigatus Virulence Factors. Biomed Res Int 2013:1–14.

209. Broek A, Keuning F, Soeharto R, Prop N. 1983. Immune suppression and histophysiology of the immune response. Virchows Arch B 43:43–54.

210. Stork CM, Schreffler SM. 2014. CyclophosphamideEncyclopedia of Toxicology: Third Edition.

211. Al-Homsi AS, Roy TS, Cole K, Feng Y, Duffner U. 2015. Post-transplant high-dose cyclophosphamide for the prevention of graft-versus-host disease. Biol Blood Marrow Transplant.

212. Fitzhugh CD, Hsieh MM, Taylor T, Coles W, Roskom K, Wilson D, Wright E, Jeffries N, Gamper CJ, Powell J, Luznik L, Tisdale JF. 2017. Cyclophosphamide improves engraftment in patients with SCD and severe organ damage who undergo haploidentical PBSCT. Blood Adv.

213. Emadi A, Jones RJ, Brodsky RA. 2009. Cyclophosphamide and cancer: Golden anniversary. Nat Rev Clin Oncol.

214. Ahlmann M, Hempel G. 2016. The effect of cyclophosphamide on the immune system: implications for clinical cancer therapy. Cancer Chemother Pharmacol.

215. Poelmans J, Hillen A, Vanherp L, Govaerts K, Maertens J, Dresselaers T, Himmelreich U, Lagrou K, Vande Velde G. 2016. Longitudinal, in vivo assessment of invasive pulmonary aspergillosis in mice by computed tomography and magnetic resonance imaging. Lab Invest 96:692–704.

216. Pietropaolo M. Pathogenesis of type 1 diabetes mellitus.

Http://WwwUptodateCom/Contents/Pathogenesis-of-Type-1-Diabetes-Mellitus 121–127.

217. La Greca AM, MacKey ER. 2009. Type 1 diabetes mellitusBehavioral Approaches to Chronic Disease in Adolescence: A Guide to Integrative Care.

218. Kawasaki E. 2014. Type 1 Diabetes and Autoimmunity. Clin Pediatr Endocrinol.

219. Yeung WCG, Rawlinson WD, Craig ME. 2011. Enterovirus infection and type 1 diabetes mellitus: Systematic review and meta-analysis of observational molecular studies. BMJ.

220. Coppieters KT, Boettler T, von Herrath M. 2012. Virus infections in type 1 diabetes. Cold Spring Harb Perspect Med.

221. Honeyman MC, Coulson BS, Stone NL, Gellert SA, Goldwater PN, Steele CE, Couper JJ, Tait BD, Colman PG, Harrison LC. 2000. Association between rotavirus infection and pancreatic islet autoimmunity in children at risk of developing type 1 diabetes. Diabetes.

222. Cabrera SM, Henschel AM, Hessner MJ. 2016. Innate inflammation in type 1 diabetes. Transl Res.

223. Wållberg M, Cooke A. 2013. Immune mechanisms in type 1 diabetes. Trends Immunol 34:583–591.

224. Szablewski L. 2014. Role of immune system in type 1 diabetes mellitus pathogenesis. Int Immunopharmacol.

225. Lehuen A, Diana J, Zaccone P, Cooke A. 2010. Immune cell crosstalk in type 1 diabetes. Nat Rev Immunol.

226. De Ferranti SD, De Boer IH, Fonseca V, Fox CS, Golden SH, Lavie CJ, Magge SN, Marx N, McGuire DK, Orchard TJ, Zinman B, Eckel RH. 2014. Type 1 diabetes mellitus and cardiovascular disease a scientific statement from the american heart association andamerican diabetes association. Circulation.

227. Chillarón JJ, Flores Le-Roux JA, Benaiges D, Pedro-Botet J. 2014. Type 1 diabetes, metabolic syndrome and cardiovascular risk. Metabolism.

228. Ryan EA, Paty BW, Senior PA, Bigam D, Alfadhli E, Kneteman NM, Lakey JRT, Shapiro AMJ. 2005. Five-year follow-up after clinical islet transplantation. Diabetes.

229. Moore A. 2009. Advances in beta-cell imaging. Eur J Radiol.

230. Alanentalo T, Asayesh A, Morrison H, Lorén CE, Holmberg D, Sharpe J, Ahlgren U. 2007. Tomographic molecular imaging and 3D quantification within adult mouse organs. Nat Methods 4:31–33.

231. Alanentalo T, Lorén CE, Larefalk A, Sharpe J, Holmberg D, Ahlgren U. 2008. High-resolution three-dimensional imaging of islet-infiltrate interactions based on optical projection tomography assessments of the intact adult mouse pancreas. J Biomed Opt 13:054070.

232. Margalit A, Kavanagh K. 2015. The innate immune response to Aspergillus fumigatus at the alveolar surface. FEMS Microbiol Rev.

233. Khanna N, Stuehler C, Lünemann A, Wójtowicz A, Bochud P, Leibundgut-Landmann S. 2016. Host response to fungal infections – how immunology and host genetics could

help to identify and treat patients at risk. Swiss Med Wkly 1–12.

234. Roilides E, Katsifa H, Walsh TJ. 1998. Pulmonary host defences against Aspergillus fumigatus. Res Immunol.

235. Berenguer J, Allende MC, Lee JW, Garrett K, Lyman C, Ali NM, Bacher J, Pizzo PA, Walsh TJ. 1995. Pathogenesis of pulmonary aspergillosis: Granulocytopenia versus cyclosporine and methylprednisolone-induced immunosuppression. Am J Respir Crit Care Med 152:1079–1086.

236. Krenke R, Grabczak EM. 2011. Tracheobronchial manifestations of Aspergillus infections. ScientificWorldJournal 11:2310–29.

237. Garth JM, Steele C. 2017. Innate Lung Defense during Invasive Aspergillosis: New Mechanisms. J Innate Immun.

238. Shaikh S, Verma H, Yadav N, Jauhari M, Bullangowda J. 2012. Applications of Steroid in Clinical Practice: A Review. ISRN Anesthesiol 2012:1–11.

239. Stephens-Romero SD, Mednick AJ, Feldmesser M. 2005. The pathogenesis of fatal outcome in murine pulmonary aspergillosis depends on the neutrophil depletion strategy. Infect Immun 73:114–125.

240. Nawada R, Amitani R, Tanaka E, Niimi A, Suzuki K, Murayama T, Kuze F. 1996. Murine model of invasive pulmonary aspergillosis following an earlier stage, noninvasive Aspergillus infection. J Clin Microbiol 34:1433–1439.

241. Kamberi M, Brummer E, Stevens DA. 2002. Regulation of bronchoalveolar macrophage proinflammatory cytokine production by dexamethasone and granulocyte-macrophage colony-stimulating factor after stimulation by Aspergillus conidia or lipopolysaccharide. Cytokine 19:14–20.

242. Brummer E, Maqbool A, Stevens DA. 2001. In vivo GM-CSF prevents dexamethasone suppression of killing of Aspergillus fumigatus conidia by bronchoalveolar macrophages. J Leukoc Biol 70:868–872.

243. Balloy V, Huerre M, Latgé J-P, Chignard M. 2005. Differences in patterns of infection and inflammation for corticosteroid treatment and chemotherapy in experimental invasive pulmonary aspergillosis. Infect Immun 73:494–503.

244. Wang Y, Chen L, Liu X, Cheng D, Liu G, Liu Y, Dou S, Hnatowich DJ, Rusckowski M. 2013. Detection of Aspergillus fumigatus pulmonary fungal infections in mice with99mTc-labeled MORF oligomers targeting ribosomal RNA. Nucl Med Biol 40:89–96.

245. Brock M, Jouvion G, Droin-Bergère S, Dussurget O, Nicola MA, Ibrahim-Granet O. 2008. Bioluminescent Aspergillus fumigatus, a new tool for drug efficiency testing and in vivo monitoring of invasive aspergillosis. Appl Environ Microbiol 74:7023–7035.

246. Rolle A-M, Hasenberg M, Thornton CR, Solouk-Saran D, Männ L, Weski J, Maurer A, Fischer E, Spycher PR, Schibli R, Boschetti F, Stegemann-Koniszewski S, Bruder D, Severin GW, Autenrieth SE, Krappmann S, Davies G, Pichler BJ, Gunzer M, Wiehr S. 2016. ImmunoPET/MR imaging allows specific detection of *Aspergillus fumigatus* lung infection in vivo. Proc Natl Acad Sci 113:E1026–E1033.

247. Vanherp L, Poelmans J, Hillen A, Govaerts K, Belderbos S, Buelens T, Lagrou K,

Himmelreich U, Vande Velde G. 2018. Bronchoscopic fibered confocal fluorescence microscopy for longitudinal in vivo assessment of pulmonary fungal infections in free-breathing mice. Sci Rep 8:3009.

248. Poelmans J, Himmelreich U, Vanherp L, Zhai L, Hillen A, Holvoet B, Belderbos S, Brock M, Maertens J, Velde GV, Lagrou K. 2018. A multimodal imaging approach enables in vivo assessment of antifungal treatment in a mouse model of invasive pulmonary aspergillosis. Antimicrob Agents Chemother 62.

249. Wu YL, Ye Q, Foley LM, Hitchens TK, Sato K, Williams JB, Ho C. 2006. In situ labeling of immune cells with iron oxide particles: an approach to detect organ rejection by cellular MRI. Proc Natl Acad Sci U S A 103:1852–1857.

250. Ho C, Hitchens TK. 2004. A non-invasive approach to detecting organ rejection by MRI: monitoring the accumulation of immune cells at the transplanted organ. Curr Pharm Biotechnol 5:551–566.

251. Schwarz S, Wong JE, Bornemann J, Hodenius M, Himmelreich U, Richtering W, Hoehn M, Zenke M, Hieronymus T. 2012. Polyelectrolyte coating of iron oxide nanoparticles for MRI-based cell tracking. Nanomedicine Nanotechnology, Biol Med 8:682–691.

252. De Temmerman M-L, Soenen SJ, Symens N, Lucas B, Vandenbroucke RE, Libert C, Demeester J, De Smedt SC, Himmelreich U, Rejman J. 2014. Magnetic layer-by-layer coated particles for efficient MRI of dendritic cells and mesenchymal stem cells. Nanomedicine 9:1363–1376.

253. Srinivas M, Cruz LJ, Bonetto F, Heerschap A, Figdor CG, de Vries IJM. 2010. Customizable, multi-functional fluorocarbon nanoparticles for quantitative in vivo imaging using19F MRI and optical imaging. Biomaterials 31:7070–7077.

254. Srinivas M, Boehm-Sturm P, Figdor CG, de Vries IJ, Hoehn M. 2012. Labeling cells for in vivo tracking using19F MRI. Biomaterials 33:8830–8840.

255. Jacoby C, Temme S, Mayenfels F, Benoit N, Krafft MP, Schubert R, Schrader J, Flögel U. 2014. Probing different perfluorocarbons for in vivo inflammation imaging by19F MRI: Image reconstruction, biological half-lives and sensitivity. NMR Biomed 27:261–271.

256. Liang S, Louchami K, Holvoet B, Verbeke R, Deroose CM, Manshian B, Soenen SJ, Lentacker I, Himmelreich U. 2018. Tri-modal In vivo Imaging of Pancreatic Islets Transplanted Subcutaneously in Mice. Mol Imaging Biol.

257. Dewitte H, Geers B, Liang S, Himmelreich U, Demeester J, De Smedt SC, Lentacker I. 2013. Design and evaluation of theranostic perfluorocarbon particles for simultaneous antigen-loading and19F-MRI tracking of dendritic cells. J Control Release 169:141–149.

258. Manshian BB, Moyano DF, Corthout N, Munck S, Himmelreich U, Rotello VM, Soenen SJ. 2014. High-content imaging and gene expression analysis to study cell-nanomaterial interactions: The effect of surface hydrophobicity. Biomaterials 35:9941–9950.

259. Petraitiene R, Petraitis V, Groll AH, Sein T, Schaufele RL, Francesconi A, Bacher J, Avila NA, Walsh TJ. 2002. Antifungal efficacy of caspofungin (MK-0991) in experimental pulmonary aspergillosis in persistently neutropenic rabbits: Pharmacokinetics, drug disposition, and relationship to galactomannan antigenemia. Antimicrob Agents

Chemother 46:12–23.

260. Petraitis V, Petraitiene R, Sarafandi A a, Kelaher AM, Lyman C a, Casler HE, Sein T, Groll AH, Bacher J, Avila N a, Walsh TJ. 2003. Combination therapy in treatment of experimental pulmonary aspergillosis: synergistic interaction between an antifungal triazole and an echinocandin. J Infect Dis 187:1834–1843.

261. Waiczies H, Lepore S, Janitzek N, Hagen U, Seifert F, Ittermann B, Purfürst B, Pezzutto A, Paul F, Niendorf T, Waiczies S. 2011. Perfluorocarbon particle size influences magnetic resonance signal and immunological properties of dendritic cells. PLoS One 6.

262. Lin S-J, Schranz J, Teutsch SM. 2001. Aspergillosis Case-Fatality Rate: Systematic Review of the Literature. Clin Infect Dis 32:358–366.

263. Massam J, Bitnun A, Solomon M, Somers GR, Guerguerian AM, Van Wylick R, Waters V. 2011. Invasive aspergillosis in cystic fibrosis: A fatal case in an adolescent and review of the literature. Pediatr Infect Dis J 30:178–180.

264. Stergiopoulou T, Meletiadis J, Roilides E, Kleiner DE, Schaufele R, Roden M, Harrington S, Dad L, Segal B, Walsh TJ. 2007. Host-dependent patterns of tissue injury in invasive pulmonary aspergillosis. Am J Clin Pathol 127:349–355.

265. Woodruff CA, Hebert AA. 2002. Neonatal primary cutaneous aspergillosis: Case report and review of the literature. Pediatr Dermatol 19:439–444.

266. Janjic JM, Ahrens ET. 2009. Fluorine-containing nanoemulsions for MRI cell tracking. Wiley Interdiscip Rev Nanomedicine Nanobiotechnology.

267. Waiczies H, Lepore S, Janitzek N, Hagen U, Seifert F, Ittermann B, Purfürst B, Pezzutto A, Paul F, Niendorf T, Waiczies S. 2011. Perfluorocarbon particle size influences magnetic resonance signal and immunological properties of dendritic cells. PLoS One 6:1–9.

268. Hertlein T, Sturm V, Jakob P, Ohlsen K. 2013. 19F Magnetic Resonance Imaging of Perfluorocarbons for the Evaluation of Response to Antibiotic Therapy in a Staphylococcus aureus Infection Model. PLoS One 8.

269. Fink C, Gaudet JM, Fox MS, Bhatt S, Viswanathan S, Smith M, Chin J, Foster PJ, Dekaban GA. 2018. 19F-perfluorocarbon-labeled human peripheral blood mononuclear cells can be detected in vivo using clinical MRI parameters in a therapeutic cell setting. Sci Rep 8.

270. Liang S, Louchami K, Kolster H, Jacobsen A, Zhang Y, Thimm J, Sener A, Thiem J, Malaisse W, Dresselaers T, Himmelreich U. 2016. In vivo and ex vivo 19-fluorine magnetic resonance imaging and spectroscopy of beta-cells and pancreatic islets using GLUT-2 specific contrast agents. Contrast Media Mol Imaging 11:506–513.

271. Kriz J, Jirak D, Berkova Z, Herynek V, Lodererova A, Girman P, Habart D, Hajek M, Saudek F. 2012. Detection of pancreatic islet allograft impairment in advance of functional failure using magnetic resonance imaging. Transpl Int 25:250–260.

272. Malosio ML, Esposito A, Brigatti C, Palmisano A, Piemonti L, Nano R, Maffi P, Cobelli F De, Maschio A Del, Secchi A. 2015. MR Imaging Monitoring of Iron Labeled Pancreatic Islets in a Small Series of Patients: Islets Fate in Successful, Unsuccessful and Auto-Transplantation. Cell Transplant 24:2285–2296.

273. Medarova Z, Moore A. 2008. Non-invasive detection of transplanted pancreatic islets, p.

88–97. *In* Diabetes, Obesity and Metabolism.

274. Arifin DR, Bulte JWM. 2011. Imaging of pancreatic islet cells. Diabetes Metab Res Rev 27:761–6.

275. Peterson JD, Haskins K. 1996. Transfer of diabetes in the NOD-scid mouse by CD4 T-cell clones: Differential requirement for CD8 T-cells. Diabetes 45:328–336.

276. Wucherpfennig KW, Eisenbarth GS. 2001. Type 1 diabetes. Nature 2:767–768.

277. Himmelreich U, Hoehn M. 2008. Stem cell labeling for magnetic resonance imaging. Minim Invasive Ther Allied Technol 17.

278. Himmelreich U, Dresselaers T. 2009. Cell labeling and tracking for experimental models using Magnetic Resonance Imaging. Methods 48:112–124.

279. Harms C, Datwyler AL, Wiekhorst F, Trahms L, Lindquist R, Schellenberger E, Mueller S, Schütz G, Roohi F, Ide A, Füchtemeier M, Gertz K, Kronenberg G, Harms U, Endres M, Dirnagl U, Farr TD. 2013. Certain types of iron oxide nanoparticles are not suited to passively target inflammatory cells that infiltrate the brain in response to stroke. J Cereb Blood Flow Metab 33.

280. Shin SH, Kadayakkara DK, Bulte JWM. 2017. In Vivo ^{19} F MR Imaging Cell Tracking of Inflammatory Macrophages and Site-specific Development of Colitis-associated Dysplasia. Radiology 282:194–201.

281. Tirotta I, Dichiarante V, Pigliacelli C, Cavallo G, Terraneo G, Bombelli FB, Metrangolo P, Resnati G. 2015. 19F magnetic resonance imaging (MRI): From design of materials to clinical applications. Chem Rev.

282. Westermann J, Söllner S, Ehlers E-M, Nohroudi K, Blessenohl M, Kalies K. 2003. Analyzing the Migration of Labeled T Cells In Vivo: An Essential Approach with Challenging Features. Lab Investig 83:459–469.

283. Gonzales C, Yoshihara HAI, Dilek N, Leignadier J, Irving M, Mieville P, Helm L, Michielin O, Schwitter J. 2016. In-Vivo Detection and Tracking of T Cells in Various Organs in a MelanomaTumor Model by 19F-Fluorine MRS/MRI. PLoS One 11:1–18.

284. Przybylski S, Gasch M, Marschner A, Ebert M, Ewe A, Helmig G, Hilger N, Fricke S, Rudzok S, Aigner A, Burkhardt J. 2017. Influence of nanoparticle-mediated transfection on proliferation of primary immune cells in vitro and in vivo. PLoS One 12:1–16.

285. Wayteck L, Dewitte H, De Backer L, Breckpot K, Demeester J, De Smedt SC, Raemdonck K. 2016. Hitchhiking nanoparticles: Reversible coupling of lipid-based nanoparticles to cytotoxic T lymphocytes. Biomaterials 77:243–254.

286. Ferreira GB, Gysemans CA, Demengeot J, da Cunha JPMCM, Vanherwegen A-S, Overbergh L, Van Belle TL, Pauwels F, Verstuyf A, Korf H, Mathieu C. 2014. 1,25-Dihydroxyvitamin D3 Promotes Tolerogenic Dendritic Cells with Functional Migratory Properties in NOD Mice. J Immunol 192:4210–4220.

287. Poulin M, Haskins K. 2000. Induction of diabetes in nonobese diabetic mice by Th2 T cell clones from a TCR transgenic mouse. J Immunol 164:3072–8.

288. Eizirik DL, Colli ML, Ortis F. 2009. The role of inflammation in insulitis and beta-cell loss in

type 1 diabetes. Nat Rev Endocrinol 5:219–226.

289. Gaglia JL, Guimaraes AR, Harisinghani M, Turvey SE, Jackson R, Benoist C, Mathis D, Weissleder R. 2011. Noninvasive imaging of pancreatic islet inflammation in type 1A diabetes patients. J Clin Invest 121:442–445.

290. Chapelin F, Gao S, Okada H, Weber TG, Messer K, Ahrens ET. 2017. Fluorine-19 nuclear magnetic resonance of chimeric antigen receptor T cell biodistribution in murine cancer model. Sci Rep 7.

291. O'Hanlon CF, Fedczyna T, Eaker S, Shingleton WD, Helfer BM. 2017. Integrating a 19F MRI Tracer Agent into the Clinical Scale Manufacturing of a T-Cell Immunotherapy. Contrast Media Mol Imaging Volume 201:1–7.

292. Boehm-Sturm P, Mengler L, Wecker S, Hoehn M, Kallur T. 2011. In Vivo tracking of human neural stem cells with 19F magnetic resonance imaging. PLoS One.

293. Waiczies S, Millward JM, Starke L, Delgado PR, Huelnhagen T, Prinz C, Marek D, Wecker Di, Wissmann R, Koch SP, Boehm-Sturm P, Waiczies H, Niendorf T, Pohlmann A. 2017. Enhanced Fluorine-19 MRI Sensitivity using a Cryogenic Radiofrequency Probe: Technical Developments and Ex Vivo Demonstration in a Mouse Model of Neuroinflammation. Sci Rep 7:1–10.

294. Liang S, Dresselaers T, Louchami K, Zhu C, Liu Y, Himmelreich U. 2017. Comparison of different compressed sensing algorithms for low SNR19F MRI applications—Imaging of transplanted pancreatic islets and cells labeled with perfluorocarbons. NMR Biomed 30.

295. Saberzadeh-Ardestani B, Karamzadeh R, Basiri M, Hajizadeh-Saffar E, Farhadi A, Shapiro AMJ, Tahamtani Y, Baharvand H. 2018. Type 1 diabetes mellitus: Cellular and molecular pathophysiology at a glance. Cell J.

296. Maahs DM, West NA, Lawrence JM, Mayer-Davis EJ. 2010. Epidemiology of type 1 diabetes. Endocrinol Metab Clin North Am.

297. Rewers M, Ludvigsson J. 2016. Environmental risk factors for type 1 diabetes. Lancet.

298. Morran MP, Vonberg A, Khadra A, Pietropaolo M. 2015. Immunogenetics of type 1 diabetes mellitus. Mol Aspects Med.

299. Furman BL. 2015. Streptozotocin-Induced Diabetic Models in Mice and Rats. Curr Protoc Pharmacol.

300. Wu J, Yan LJ. 2015. Streptozotocin-induced type 1 diabetes in rodents as a model for studying mitochondrial mechanisms of diabetic β cell glucotoxicity. Diabetes, Metab Syndr Obes Targets Ther.

301. Morel PA. 2013. Dendritic cell subsets in type 1 diabetes: Friend or foe? Front Immunol.

302. Mellman I, Steinman RM. 2001. Dendritic cells: Specialized and regulated antigen processing machines. Cell.

303. Kaliński P, Hilkens CMU, Wierenga EA, Kapsenberg ML. 1999. T-cell priming by type-1 and type-2 polarized dendritic cells: The concept of a third signal. Immunol Today.

304. Pletinckx K, Döhler A, Pavlovic V, Lutz MB. 2011. Role of dendritic cell maturity/costimulation for generation, homeostasis, and suppressive activity of

regulatory T cells. Front Immunol.

305. Gillespie KM. 2006. Type 1 diabetes: Pathogenesis and prevention. CMAJ.

306. Yoon JW, Jun HS. 2005. Autoimmune destruction of pancreatic β cellsAmerican Journal of Therapeutics.

307. Vanherwegen A-S, Gysemans C, Overbergh L. 2015. Dendritic cell metabolism: immunity and tolerance. Oncotarget.

308. Ganguly D, Haak S, Sisirak V, Reizis B. 2013. The role of dendritic cells in autoimmunity. Nat Rev Immunol.

309. O'Neill E, Hammond N, Miller FH. 2014. MR imaging of the pancreas. Radiol Clin North Am.

310. Gaglia JL, Harisinghani M, Aganj I, Wojtkiewicz GR, Hedgire S, Benoist C, Mathis D, Weissleder R. 2015. Noninvasive mapping of pancreatic inflammation in recent-onset type-1 diabetes patients. Proc Natl Acad Sci.

311. Thoeni RF. 2015. Imaging of Acute Pancreatitis. Radiol Clin North Am.

312. Mallak N, Hope TA, Guimaraes AR. 2018. PET/MR Imaging of the Pancreas. Magn Reson Imaging Clin N Am.

313. Vandeputte C, Thomas D, Dresselaers T, Crabbe A, Verfaillie C, Baekelandt V, Van Laere K, Himmelreich U. 2011. Characterization of the inflammatory response in a photothrombotic stroke model by MRI: Implications for stem cell transplantation. Mol Imaging Biol.

314. Weber R, Wegener S, Ramos-Cabrer P, Wiedermann D, Hoehn M. 2005. MRI detection of macrophage activity after experimental stroke in rats: New indicators for late appearance of vascular degradation? Magn Reson Med.

315. Weise G, Basse-Luesebrink TC, Wessig C, Jakob PM, Stoll G. 2011. In vivo imaging of inflammation in the peripheral nervous system by 19F MRI. Exp Neurol.

316. Balducci A, Helfer BM, Ahrens ET, Ohanlon CF, Wesa AK. 2012. Visualizing arthritic inflammation and therapeutic response by fluorine-19 magnetic resonance imaging (19F MRI). J Inflamm (United Kingdom).

317. Srinivas M, Tel J, Schreibelt G, Bonetto F, Cruz L-J, Amiri H, Heerschap A, Figdor CG, de Vries IJM. 2015. PLGA-encapsulated perfluorocarbon nanoparticles for simultaneous visualization of distinct cell populations by ^{19} F MRI. Nanomedicine 10.

318. Trekker J, Leten C, Struys T, Lazenka V V., Argibay B, Micholt L, Lambrichts I, Van Roy W, Lagae L, Himmelreich U. 2014. Sensitive invivo cell detection using size-optimized superparamagnetic nanoparticles. Biomaterials.

319. Staelens D, Liang S, Appeltans B, Van de Wouwer M, Van den Mooter G, Van Assche G, Himmelreich U, Vande Velde G. 2016. Visualization of delayed release of compounds from pH-sensitive capsules in vitro and in vivo in a hamster model. Contrast Media Mol Imaging.

320. Lyman M, Lloyd DG, Ji X, Vizcaychipi MP, Ma D. 2014. Neuroinflammation: The role and consequences. Neurosci Res.

321. Willerson JT. 2004. Inflammation as a Cardiovascular Risk Factor. Circulation.

322. Eizirik DL, Colli ML, Ortis F. 2009. The role of inflammation in insulitis and β-cell loss in type 1 diabetes. Nat Rev Endocrinol 5:219–226.

323. Takenaka MC, Quintana FJ. 2017. Tolerogenic dendritic cells. Semin Immunopathol.

324. Nikolic T, Roep BO. 2013. Regulatory multitasking of tolerogenic dendritic cells - lessons taken from vitamin D3-treated tolerogenic dendritic cells. Front Immunol.

325. Manicassamy S, Pulendran B. 2011. Dendritic cell control of tolerogenic responses. Immunol Rev.

326. Palucka K, Banchereau J. 2014. Cancer immunotherapy via dendritic cellsInteraction of Immune and Cancer Cells.

327. Tacken PJ, De Vries IJM, Torensma R, Figdor CG. 2007. Dendritic-cell immunotherapy: From ex vivo loading to in vivo targeting. Nat Rev Immunol.

328. Figdor CG, De Vries IJM, Lesterhuis WJ, Melief CJM. 2004. Dendritic cell immunotherapy: Mapping the way. Nat Med.

329. Sugawara E, Nikaido H. 2000. Immunobiology of dendritic cells. Annu Rev Immunol.

330. Hori Y, Winans AM, Huang CC, Horrigan EM, Irvine DJ. 2008. Injectable dendritic cell-carrying alginate gels for immunization and immunotherapy. Biomaterials.

331. Serreze D V, Gaskins HR, Leiter EH. 1993. Defects in the differentiation and function of antigen presenting cells in NOD/Lt mice. J Immunol.

332. Calderon B, Unanue ER. 2012. Antigen presentation events in autoimmune diabetes. Curr Opin Immunol.

333. Baumjohann D, Hess A, Budinsky L, Brune K, Schuler G, Lutz MB. 2006. In vivo magnetic resonance imaging of dendritic cell migration into the draining lymph nodes of mice. Eur J Immunol.

334. De Vries IJM, Lesterhuis WJ, Barentsz JO, Verdijk P, Van Krieken JH, Boerman OC, Oyen WJG, Bonenkamp JJ, Boezeman JB, Adema GJ, Bulte JWM, Scheenen TWJ, Punt CJA, Heerschap A, Figdor CG. 2005. Magnetic resonance tracking of dendritic cells in melanoma patients for monitoring of cellular therapy. Nat Biotechnol.

335. Chen J, Lanza GM, Wickline SA. 2010. Quantitative magnetic resonance fluorine imaging: Today and tomorrow. Wiley Interdiscip Rev Nanomedicine Nanobiotechnology.

336. Hitchens TK, Ye Q, Eytan DF, Janjic JM, Ahrens ET, Ho C. 2011. 19F MRI detection of acute allograft rejection with in vivo perfluorocarbon labeling of immune cells. Magn Reson Med.

337. Lentacker I, Raemdonck K, Manshian B, Himmelreich U, Gysemans C, De Smedt SC, Saini S, Verbeke R, Korf H, Liang S. 2019. Challenges for labeling and longitudinal tracking of adoptively transferred autoreactive T lymphocytes in an experimental type-1 diabetes model. Magn Reson Mater Physics, Biol Med.

338. Kok MB, De Vries A, Abdurrachim D, Prompers JJ, Grüll H, Nicolay K, Strijkers GJ. 2011. Quantitative 1H MRI, 19F MRI, and 19F MRS of cell-internalized perfluorocarbon paramagnetic nanoparticles. Contrast Media Mol Imaging.

339. Chung BH, Lim YT. 2009. Cell labeling and imaging using multifunctional perfluorocarbon nanoemulsion. PCT Int Appl.

340. Oliva J, Bardag-Gorce F, Wood A, Sota H, Niihara Y. 2015. Direct labeling of 19F-perfluorocarbon onto multilayered cell sheet for MRI-based non-invasive cell tracking. Tissue Eng Regen Med.

341. Maldonado RA, von Andrian UH. 2010. How Tolerogenic Dendritic Cells Induce Regulatory T Cells. Adv Immunol.

342. Suwandi JS, Toes REM, Nikolic T, Roep BO. 2015. Inducing tissue specific tolerance in autoimmune disease with tolerogenic dendritic cells. Clin Exp Rheumatol.

343. Noh Y-W, Lim YT, Chung BH. 2008. Noninvasive imaging of dendritic cell migration into lymph nodes using near-infrared fluorescent semiconductor nanocrystals. FASEB J.

344. Ren PG, Lee SW, Biswal S, Goodman SB. 2008. Systemic trafficking of macrophages induced by bone cement particles in nude mice. Biomaterials.

345. Meir R, Shamalov K, Betzer O, Motiei M, Horovitz-Fried M, Yehuda R, Popovtzer A, Popovtzer R, Cohen CJ. 2015. Nanomedicine for Cancer Immunotherapy: Tracking Cancer-Specific T-Cells in Vivo with Gold Nanoparticles and CT Imaging. ACS Nano.

346. Love C, Tomas MB, Tronco GG, Palestro CJ. 2005. FDG PET of Infection and Inflammation. RadioGraphics.

347. Hertlein T, Sturm V, Kircher S, Basse-Lüsebrink T, Haddad D, Ohlsen K, Jakob P. 2011. Visualization of abscess formation in a murine thigh infection model of Staphylococcus aureus by 19F-magnetic resonance imaging (MRI). PLoS One.

348. Fu PP, Xia Q, Hwang HM, Ray PC, Yu H. 2014. Mechanisms of nanotoxicity: Generation of reactive oxygen species. J Food Drug Anal.

349. Khanna P, Ong C, Bay B, Baeg G. 2015. Nanotoxicity: An Interplay of Oxidative Stress, Inflammation and Cell Death. Nanomaterials.

350. Ahrens ET, Bulte JWM. 2013. Tracking immune cells in vivo using magnetic resonance imaging. Nat Rev Immunol 13.

351. Bönner F, Merx MW, Klingel K, Begovatz P, Flögel U, Sager M, Temme S, Jacoby C, Salehi Ravesh M, Grapentin C, Schubert R, Bunke J, Roden M, Kelm M, Schrader J. 2015. Monocyte imaging aftermyocardial infarction with ^{19}FMRI at 3 T: A pilot study in explanted porcine hearts. Eur Heart J Cardiovasc Imaging 16.

352. Liu Z, Li Z. 2014. Molecular imaging in tracking tumor-specific Cytotoxic T Lymphocytes (CTLs). Theranostics.

353. Boissonnas A, Fetler L, Zeelenberg IS, Hugues S, Amigorena S. 2007. In vivo imaging of cytotoxic T cell infiltration and elimination of a solid tumor. J Exp Med.

354. Forouhi NG, Wareham NJ. 2019. Epidemiology of diabetes. Med (United Kingdom).

355. DiMeglio LA, Evans-Molina C, Oram RA. 2018. Type 1 diabetes. Lancet.

356. Ahrens ET, Srinivas M, Morel PA, Ernst LA, Laidlaw DH. 2007. Fluorine-19 MRI for visualization and quantification of cell migration in a diabetes model. Magn Reson Med.

357. Boudewijns S, Bloemendal M, Gerritsen WR, de Vries IJM, Schreibelt G. 2016. Dendritic cell vaccination in melanoma patients: From promising results to future perspectives. Hum Vaccines Immunother.

358. Chapelin F, Capitini CM, Ahrens ET. 2018. Fluorine-19 MRI for detection and quantification of immune cell therapy for cancer. J Immunother Cancer.

359. Lee SB, Lee HW, Lee H, Jeon YH, Lee SW, Ahn BC, Lee J, Jeong SY. 2017. Tracking dendritic cell migration into lymph nodes by using a novel PET probe 18F-tetrafluoroborate for sodium/iodide symporter. EJNMMI Res.

360. Pham W, Xie J, Gore JC. 2007. Tracking the Migration of Dendritic Cells By In Vivo Optical Imaging. Neoplasia.

Curriculum Vitae

Shweta Saini

Address	Diamantlaan 210, Leiden, The Netherlands
Place and Date of birth	India, 14 May 1986
Nationality	Indian

University education

2014 – 2018	Marie Curie Biomedical Doctoral student KU Leuven, Belgium
2010 – 2012	Master of Science in Molecular Imaging University of Paris Sud, France
2004 – 2009	Bachelor of Technology in Biotechnology Uttar Pradesh Technical University, India

Fellowships

- Marie Curie EC-FP7- Beta Train, Initial Training Network (ITN) PhD grant, Leuven , Belgium
- Travel grant from WMIS society for World Molecular Imaging Congress, Philadelphia, USA
- Erasmus fellowship for master thesis from University of Paris Sud, Paris, France

First-author abstracts at (inter)national conferences

Shweta Saini, Jennifer Poelmans, Sayuan Liang, Rein Verbeke, Greetje Vande Velde, Hannelie Korf, Ine Lentacker, Stefaan Desmedt, Katrien Lagrou, Uwe Himmelreich. Dynamic study of host-pathogen interaction in murine models of aspergillosis using fluorine-19 MRI. European Molecular Imaging Meeting (EMIM), San Sebastian, Spain, March 2018.

Shweta Saini, Jennifer Poelmans, Sayuan Liang, Rein Verbeke, Greetje Vande Velde, Hannelie Korf, Ine Lentacker, Stefaan Desmedt, Katrien Lagrou, Uwe Himmelreich. ^{19}F MRI allows longitudinal follow-up of immune cells in pulmonary infectious disease mouse model. Young Belgian Molecular Resonance Scientists (YBMRS) conference. Blankenberge, Belgium, December 2017.

Shweta Saini, Jennifer Poelmans, Sayuan Liang, Rein Verbeke, Greetje Vande Velde, Hannelie Korf, Ine Lentacker, Stefaan Desmedt, Katrien Lagrou, Uwe Himmelreich. ^{19}F MRI to study Immune cell infiltration in pulmonary Aspergillus. World Molecular Imaging Congress (WMIC), Philadelphia, USA, September 2017.

Shweta Saini, Hannelie Korf, Sayuan Liang, Rein Verbeke, Ine Lentacker, Stefaan Desmedt, Chantal Mathieu, Uwe Himmelreich. Follow-up and detection of biomarkers for study of disease progression in LPS induced lung inflammation model fluorine-19 imaging. European Molecular Imaging Meeting (EMIM), Cologne, Germany, April 2017.

Shweta Saini, Hannelie Korf, Sayuan Liang, Rein Verbeke, Ine Lentacker, Stefaan Desmedt, Chantal Mathieu, Uwe Himmelreich. T cell labeling and tracking in a type 1 diabetes model using ^{19}F MRI. Belgian Molecular Imaging Community (BMIC) meeting. Brussels, Belgium, May 2016.

Shweta Saini, Hannelie Korf, Sayuan Liang, Rein Verbeke, Ine Lentacker, Stefaan Desmedt, Chantal Mathieu, Uwe Himmelreich. Immune cell labeling and biodistribution profile study: a step towards insight of T1D pathogenesis. DiabImage Symposium, Stockholm, Sweden, September 2015.

Scientific Publications

S Saini, H Korf, Sayuan Liang, R Verbeke, B Manshian, K Raemdonck, I Lentacker, C Gysemans, SC. De Smedt, U Himmelreich. Challenges for labeling and longitudinal tracking of adoptively transferred autoreactive T lymphocytes in an experimental type 1 diabetes model. Magn Reson Mater Phy (2019).

B Manshian, J Poelmans, S Saini, S Pokhrel, J J Grez, U Himmelreich, L Mädler, S J Soenen. Nanoparticle-induced inflammation can increase tumor malignancy. Acta Biomater. (2018).

S Saini, J Poelmans, H Korf, J L Dooley, S Liang, B Manshian, R Verbeke, S J Soenen, G Vande Velde, I Lentacker, K Lagrou, A Liston, C Gysemans, SC. De Smedt, U Himmelreich. ^{19}F MRI allows non-invasive longitudinal monitoring of host-microbe interactions in murine pulmonary aspergillosis. Under review in iScience Journal, Cell press, Elsevier.

S Saini, A Vanherwegen, S Liang, R Verbeke, H Korf, I Lentacker, C Gysemans, SC. De Smedt, U Himmelreich. Fluorine MR imaging probes dynamic migratory profiles of perfluorocarbonloaded dendritic cells in type 1 diabetes model. In preparation for publication in Journal of Molecular Imaging and Biology, Springer.

Personal Contribution

All experiments reported in chapter 3, 4 and 5 have been designed, performed, analyzed and reported by Shweta Saini under the supervision of Prof. Uwe Himmelreich. In chapter 3, Dr. Jennifer Poelmans helped in fungal model development, BLI data acquisition, data analyses and histology. For chapter 3 and 4, Dr. Hannelie Korf provided help in designing the experiment and data analyses. Shweta Saini acquired and analyzed overall *in vitro* and *in vivo* experimental data. Shweta Saini and Dr. Conny Gysemans designed chapter 5 and Dr. An-Sofie Vanherwegen provided help in data acquisition and data analyses.

Scientific Acknowledgement

Chapter 3

The authors acknowledge Dr. Bala Attili (Laboratory of Radiopharmaceutical Research, KU Leuven, Belgium) for providing help with the formulation of HCA treatment and Dr. Matthias Brock (University of Nottingham, UK) for providing the $Fluc^{+}$ *A. fumigatus* strain 2/7/1. Its use was granted by the Leibniz Institute for Natural Product Research and Infection Biology (Hans Knöll Institute, Jena, Germany). We are grateful for the financial support by the following funding agencies: the European Commission Marie Curie (ITN) BetaTrain (289932), the Research Foundation Flanders (FWO, G.0A75.14, G.0B28.14 and G.069115N), the Agentschap voor Innovatie door Wetenschap en Technologie for the SBO NanoCoMIT (IWT SBO 140061), the European ERA-NET project 'CryptoView' (3rd call of the FP7 programme Infect-ERA) and KU Leuven for PF 10/017 (IMIR).

Chapter 4

The authors acknowledge the funding agencies, the European Commission Marie Curie (ITN) BetaTrain (289932), the Research Foundation Flanders (FWO, G.0A75.14 and G.0B28.14) and the

Agentschap voor Innovatie door Wetenschap en Technologie (IWT 140061, SBO NanoCoMIT) for supporting this work.

Chapter 5

The authors acknowledge Jos Laureys and Dries Swinnen (Clinical and Experimental Endocrinology, KU Leuven, Belgium) for their technical assistance. We would like to thank the staff of the VIB-KU Leuven FACS Core Facility for the assistance with flow cytometry. We are grateful for the financial support by the following funding agencies: the European Commission Marie Curie (ITN) BetaTrain (289932), the Research Foundation Flanders (FWO, G.0A75.14, G.0B28.14, 11Y5915N and G.069115N), the Agentschap voor Innovatie door Wetenschap en Technologie for the SBO NanoCoMIT (IWT SBO 140061).

Conflict of interest

The candidate declares that there are no other conflicts of interest.